Report No.
UCB/SEMM-2015/05

Structural Engineering
Mechanics and Materials

Simulations of Innovative Solutions for Energy Efficient Building Façades

By

Aashish Ahuja
Khalid M. Mosalam
Tarek I. Zohdi

December 2015

Department of Civil and Environmental Engineering
University of California, Berkeley

Abstract

Simulations of Innovative Solutions for Energy Efficient Building Façades

by

Aashish Ahuja

Khalid M. Mosalam

Tarek I. Zohdi

The last decade has witnessed a heightened interest in making buildings more sustainable, which has been fueled largely by the relative increase in energy costs and advancements in manufacturing technology. Lighting consumes a substantial amount of the building energy consumption, making it necessary to look for alternative technology that depends more on natural lighting. A structural element for façades called the Translucent Concrete (TC) panel has been developed for capturing and delivering daylight into buildings that could reduce our dependence on artificial lighting and save energy. It consists of optical fibers embedded in concrete that can channel diffused sunlight into the office building workspace. The transmission of light is analyzed using a newly developed ray tracing software that is coupled with an open source software $RADIANCE$ to compute the spatial illumination in a room. The information on distribution of illumination is applied to occupancy profiles generated from Markov chain models and is finally combined with light switching models to estimate the energy saved from using daylighting as an alternative to artificial lighting. It is observed from calculations on a studied windowless room example that using TC panels with a practical optical fiber volumetric ratio from constructibility view point can save at least 44% of lighting energy, spent between 8 am - 6 pm annually. These results have been presented for a place like Berkeley that due to its proximity to the Pacific Ocean experiences a Mediterranean type of climate.

The utility of a south-facing wall consisting of TC panels would be enhanced if it can also reduce the heating and cooling requirements of a room. Using the solar radiation channeled by optical fibers can offset some of the heating requirements of the room. On the other hand, if the optical fiber density in the TC panels is high, solar radiation leads to overheating and in this case cooling loads consume large portion of the building energy. Moreover, the use of natural daylight in illuminating the office work space reduces heat dissipation from lighting installations and positively impacts cooling loads. Moreover,

conduction through the walls allows heat to be removed from the room during the morning but transmits heat from the ambient environment into the room later in the afternoon and evening. A thermal analysis algorithm is developed to calculate the heat transfer due to solar radiation, conduction through walls and heat dissipation from lighting installations. The thermal analysis is coupled with lighting analysis to search for an optimal optical fiber volumetric ratio for the TC panels that would reduce the energy expenditure on lighting, heating and cooling with respect to energy spent in a daylight-deprived room with opaque walls. The TC panels are able to cut down energy expenditure by as much as 18% for a fiber volumetric ratio of 5.6% which is also consistent with the objective of maintaining structural integrity and making the fabrication process practical for the construction case of the TC panels by having fewer embedded optical fibers.

Contents

List of Figures

List of Tables

Acknowledgments

The research funding was made possible by the Republic of Singapore's National Research Foundation through a grant to the Berkeley Education Alliance for Research in Singapore (BEARS) for Singapore-Berkeley Building Efficiency and Sustainability in the Tropics (SinBerBEST) Program. BEARS has been established by the University of California, Berkeley as a center for intellectual excellence in research and education in Singapore.

Chapter 1

Introduction

The translucent concrete (TC) is envisioned as a novel building material which is capable of transmitting sunlight from the exterior environment to the inside space of the building. It consists of plastic optical fibers that are embedded in the concrete mix at the time of construction. The optical fibers acts as light channels that are able to guide light through them. An innovation such as TC can be used as a part of a building envelope ($i.e$ wall and roof), since it satisfies requirements which are usually set apart [44]: (a) Envelope behaving as a structural sub-system, (b) Construction procedure is simple and scalable, and (c) Movable and mechanized parts are avoided. In this chapter, the objective of pursuing the development of this new construction material is presented. This would be followed by an elaborate discussion on the tools that have been developed as part of this report, which can be used by engineers and architects to model and evaluate the different designs of TC panels during the pre-construction and planning stages.

1.1 Building façade and building envelope

The building envelope is one of the most visible and technically complex aspects of architecture. It is the enclosing membrane in vertical, sloped, horizontal or other geometric configuration that protects the indoor environment from external environmental impacts. It is also an interface between the external environment and the indoor environment. Moreover, building envelope regulates the energy consumption, consumption of resources like materials ($e.g.$ sand, cement, wood, steel) and water and environmental degradation [24]. Apart from its protective and regulatory functions, the building envelope controls solar and thermal flow, as well as the moisture flow in and out of the building. It also controls the effects of fire, wind and rain on buildings. The indoor environmental quality (IEQ) measures the productivity of the people working inside the building and their exposure

to building-health related problems. In fact to achieve a high value of IEQ, critical components like indoor air quality, thermal comfort, lighting and acoustic effects should be regulated properly. A well-built building envelope can control the inflow of pollutants, introduce daylight and views and provide controls to the occupants for thermal and lighting comfort, thus, improving the overall IEQ for the residents.

Within a building envelope, the building façade acts as the most important component in modulating the energy and environmental performance. With the increase in energy costs and demand by countries worldwide to control building resource consumption and pollution, there is a heightened interest in making buildings more sustainable and energy efficient. Buildings (commercial and residential) consumed almost 41% of the total energy and 74% of generated electricity that was available for use in the United States in 2011 [11]. A large part of this energy consumption, in the form of electricity, was solely utilized in artificially lighting the indoors of buildings. The electric energy was derived primarily from thermal power plants which are not clean sources and contribute to green house gas emissions. This makes it necessary to search for alternative technology that depends more on natural lighting. Figure 1.1a details the sources of energy consumption in the USA. Figure 1.1b gives the distribution of energy in a commercial building [11].

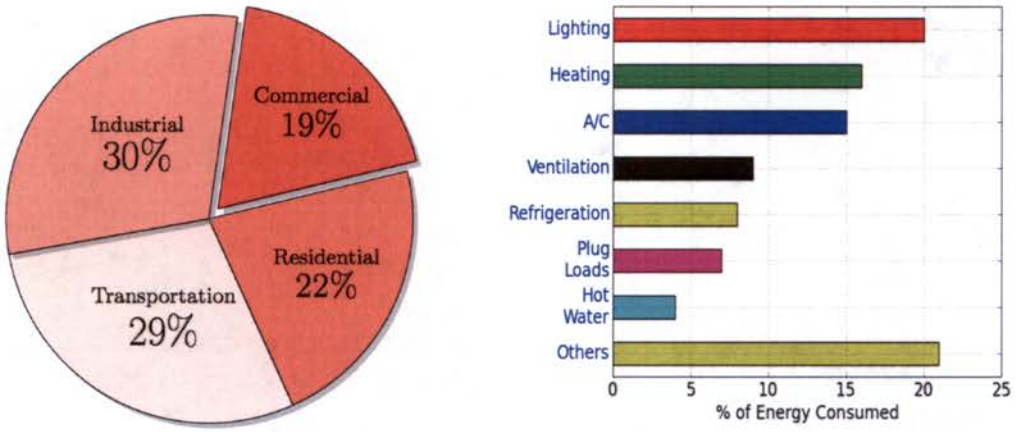

(a) Sources of energy use

(b) Energy consumption in commercial buildings

Figure 1.1: Energy consumed by USA in 2011 [11].

1.2 Daylighting using TC

The utilization of sunlight to illuminate the interior spaces of buildings is beneficial as it provides the human occupants with a healthy environment and contributes to energy savings by decreasing the electricity used for artificial lighting. Today, exterior glazing is the only solution to allow natural daylight to pass through the building's envelope. Also, we see that the amount of external glazing used in a building, measured by window-to-wall ratio (WWR), is increasing in new and retrofitted buildings. A number of industry codes in the United States like ASHRAE 90.1-2010 and ASHRAE 189.1-2013 were proposed to limit the amount of glazing citing low insulation value, high solar heat gains, and the potential for glare within the space. Other reasons to limit glazing but not discussed in this report could include issues related to building safety and falling hazard of glass curtain walls under extreme loads by earthquakes [41]. These proposals to reduce the WWR were voted down and subsequently dropped (twice in ASHRAE 90.1 and once in ASHRAE 189.1) as they limited the occupant's view to nature and daylight and constrained the architect's design intent.

Since the demand for natural daylighting inside the buildings is well established, building designers are also beginning to seek means other than windows to capture, transport, and deliver natural light into the interior spaces of buildings. For example, designers have recently started using flexible solar light pipes for transmitting light into inner rooms of the building. The interests in using alternative sources of lighting, have led to the development of a concept called 'Translucent Concrete' (TC). This counterintuitive notion is the idea that light conduits, for example optical fibers, can be embedded in the concrete to allow light to pass through them. The TC panels are envisioned to coexist with windows in a building which will neither restrict the occupant's view to the outside environment nor hamper an architect's ability to design buildings which are aesthetically appealing. Moreover, as we will see in Chapter 8, diffused light emitted by the optical fibers in the panel has the ability to reduce glare and save up to 50% lighting energy with a reasonable fiber volumetric ratio of $\sim$ 6%. This innovation has the potential to redefine the way people think of concrete walls, from that of opaque and bland element of the envelope, to one that is transporting and providing natural daylight into the interior space of an otherwise artificially lit room. Thus, together with existing building components, the TC panels might be able to save energy and also offer a comfortable indoor environment to its occupants.

1.3 Previous work on TC

In 2001, the Hungarian architect Aron Losonczi invented LiTraCon^{TM}, the first commercially available form of TC [39]. It was a combination of optical fibers and fine concrete, combined in such a way that the material was both internally and externally homogeneous. It was manufactured in blocks and used primarily for decoration. The current price of a LiTraCon^{TM} 100 mm thick block is approximately €$2140/m^2$ (ex-works), which makes it prohibitively expensive and difficult to commercialize. During the Shanghai 2010 EXPO, Italy modeled its pavilion out of TC using about 4,000 blocks. The blocks were rather heavy to be used as a façade sub-system in buildings. Another product featured plastic fibers arranged in a grid, namely Pixel Panels, developed by Bill Price of the University of Houston. These panels transmitted light in a pattern resembling thousands of tiny stars in the night sky. University of Detroit-Mercy also developed a process to produce translucent panels made of Portland cement and sand and reinforced the panel with a small amount of chopped fiberglass. These panels, which were only 2.5 mm thick at their centers, were thin enough to be translucent under direct light. A number of companies are also producing translucent concrete with different production systems. Some manufacturers are:

- Florak Bauunternehmung GmbH, Heinsberg/Germany
- LBM EFO, Berching/Germany
- LUCEM GmbH, Stolberg/Germany
- Luccon Lichtbeton GmbH, Klaus/Austria

The primary focus of the TC technology has previously been on its aesthetic appeal and its application in artistic design. Recently, He et al. [16] published a study on smart TC which experimentally explored the light emission properties of TC in the laboratory. Interestingly, there has also been some active research in the development of other light transmitting façades. As an example, a recent study on a novel translucent façade made of organic materials like sucrose was published in [14].

1.4 Organization of chapters

The flowchart in Figure 1.2 gives a layout of the organization of chapters in this report. The first part is devoted to modeling the interaction of sunlight with TC panels and quantifying the distribution of light as it exits from these panels. In the second part, using the concepts from statistics, the energy saved as a result of reduction in the dependence on artificial lighting is estimated. In the last part, a finite difference model is proposed to calculate heat

conduction through the different layers of the TC panel. Two case studies are implemented that use the concepts presented in the three different parts of developed theory of analyzing TC panels and links them together. The last part includes conclusions from the study and alludes the readers to future research that is being conducted to further improve the overall capabilities of TC panels.

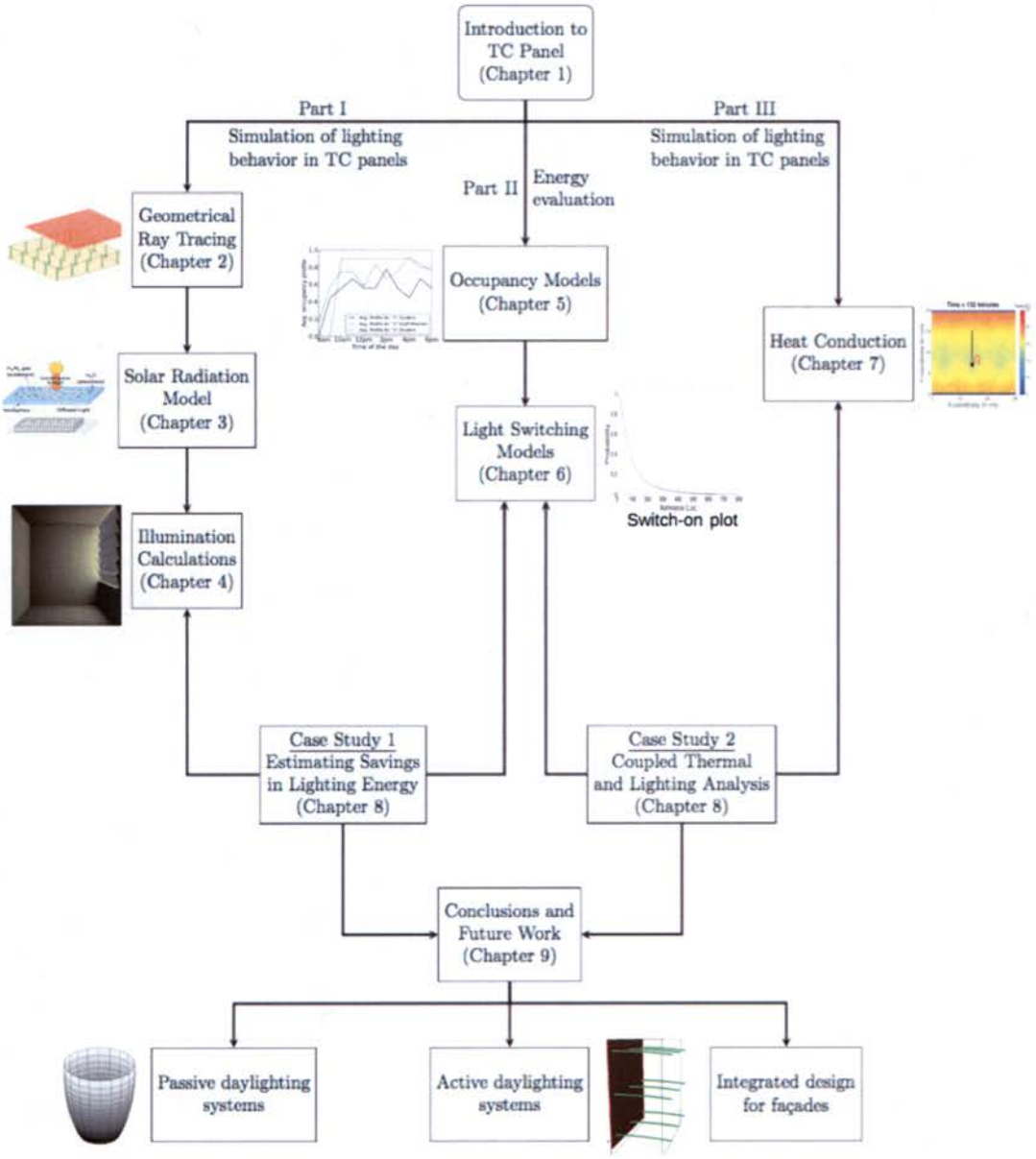

Figure 1.2: Organization of chapters.

1.5 Summary

In this chapter, the following concluding remarks can be inferred:

1. Buildings contribute to 41% of the total energy that is consumed in the United States.
2. Harvesting sunlight for illumination of indoor spaces provides a passive strategy for reducing artificial lighting.
3. A new building façade material is proposed called Translucent Concrete (TC) that can channel light using optical fibers embedded in the concrete matrix.
4. The following chapters will discuss the numerical methods to evaluate the TC panels as an innovative solution for energy efficient building envelope.

Chapter 2

Geometrical Ray Tracing

Ray tracing methods begin by representing wavefronts as an array of discrete rays. Geometrically, one proceeds by tracking each ray as it changes trajectories. On encountering a surface, the intersection point is either determined analytically (in case the surface geometry is simple such as a sphere or a polygon) or using some numerical method, like Newton's method. Next, Fresnel's law is applied at the intersection point and the outgoing ray (reflected or refracted) is calculated. Ray-tracing methods, in general, are suited for the computation of scattering in systems that are difficult to mesh/discretize. It is assumed for the applicability of the method that the length scale of the surface features are large enough relative to the optical wavelength of sunlight (280 $nm \leq \lambda \leq 4000\ nm$) [68].

2.1 Eikonal equation for light waves

The theoretical derivation of the "Ray Theory" and the formulation of Eikonal equation for any wavefront is presented in Appendix A. In this chapter, a numerical method to march rays in space by discretizing the ray tracing equation is presented. The formulation of a ray of light wave is given as

$$\frac{d(n\hat{\mathbf{s}})}{ds} = \nabla n \tag{2.1}$$

where $n(x, y, z)$ is the refractive index of the medium at a space coordinate (x, y, z) and the direction of light ray is given by the unit vector, $\hat{\mathbf{s}}$. Let $\hat{\mathbf{s}}$ be described in terms of its direction cosines, $[\cos\alpha, \cos\beta, \cos\gamma]$, with $[\alpha, \beta, \gamma]$ being the angles between the direction of ray path and $[x, y, z]$ axes, respectively. Differentiating left hand expression in Equation (2.1) gives:

$$n\frac{d\hat{\mathbf{s}}}{ds} = \nabla n - \hat{\mathbf{s}}\frac{dn}{ds} \tag{2.2}$$

The directional derivative of dn/ds in direction $\hat{s}$ is written as

$$\frac{dn}{ds} = \hat{\mathbf{s}}.\nabla n \tag{2.3}$$

Combining Equations (2.2) and (2.3) and rearranging the terms give

$$\frac{d\hat{\mathbf{s}}}{ds} = \frac{1}{n}(\nabla n - (\hat{\mathbf{s}}.\nabla n)\hat{\mathbf{s}}) \tag{2.4}$$

where

$$\nabla n = \left[\frac{\partial n}{\partial x}, \frac{\partial n}{\partial y}, \frac{\partial n}{\partial z}\right] = [n_x, n_y, n_z] \tag{2.5}$$

Equation (2.4) is separated into components which are written as:

$$\frac{d(\cos\alpha)}{ds} = \frac{1}{n}\left\{n_x - \left(\nabla n.\hat{\mathbf{s}}\right)\cos\alpha\right\} \tag{2.6}$$

$$\frac{d(\cos\beta)}{ds} = \frac{1}{n}\left\{n_y - \left(\nabla n.\hat{\mathbf{s}}\right)\cos\beta\right\} \tag{2.7}$$

$$\frac{d(\cos\gamma)}{ds} = \frac{1}{n}\left\{n_y - \left(\nabla n.\hat{\mathbf{s}}\right)\cos\gamma\right\} \tag{2.8}$$

To integrate Equations (2.6), (2.7) and (2.8), the forward Euler scheme is used. The equations are discretized along the path length, ds, to give:

$$d(\cos\alpha) \rightarrow (\cos\alpha)_{k+1} - (\cos\alpha)_k \tag{2.9}$$

$$d(\cos\beta) \rightarrow (\cos\beta)_{k+1} - (\cos\beta)_k \tag{2.10}$$

$$d(\cos\gamma) \rightarrow (\cos\gamma)_{k+1} - (\cos\gamma)_k \tag{2.11}$$

$$ds \rightarrow \Delta s \tag{2.12}$$

where k denotes the integration step, and Δs is a finite integration step. The discretized form is expressed as

$$(\cos\alpha)_{k+1} = \frac{1}{n}\left\{n_x - \left(\nabla n.\hat{\mathbf{s}}\right)\cos\alpha\right\}_k \Delta s + (\cos\alpha)_k \tag{2.13}$$

$$(\cos\beta)_{k+1} = \frac{1}{n}\left\{n_y - \left(\nabla n.\hat{\mathbf{s}}\right)\cos\beta\right\}_k \Delta s + (\cos\beta)_k \tag{2.14}$$

and to determine $(\cos\gamma)_{k+1}$, the property of directional cosines can be used:

$$(\cos\gamma)_{k+1} = \sqrt{1 - (\cos\alpha)_{k+1}^2 - (\cos\beta)_{k+1}^2} \tag{2.15}$$

Finally, the ray position at any instant can be expressed in the following form:

$$x_{k+1} = x_k + \Delta s(\cos\alpha)_{k+1} \tag{2.16}$$

$$y_{k+1} = y_k + \Delta s(\cos\beta)_{k+1} \tag{2.17}$$

$$z_{k+1} = z_k + \Delta s(\cos\gamma)_{k+1} \tag{2.18}$$

Thus, the time spent by light ray in the optical system is evaluated as:

$$T_{k+1} = T_k + \frac{\Delta s}{u} = T_k + \frac{\Delta s}{c/n} \tag{2.19}$$

where u is the wave speed in the medium of propagation and c is the absolute speed of light in vacuum. Note that $n = \frac{u}{c}$.
Remark: The travel times of different light rays calculated using the discretization presented above can also be used to assess the dispersion properties of the optical medium.

The value of ∇n can be estimated using finite differences as follows:

$$\begin{aligned}\nabla n &= [n_x, n_y, n_z] \\ &= \Big[\frac{n(x+\delta x, y, z) - n(x, y, z)}{\delta x}, \frac{n(x, y+\delta y, z) - n(x, y, z)}{\delta y}, \\ &\qquad \frac{n(x, y, z+\delta z) - n(x, y, z)}{\delta z}\Big]\end{aligned} \tag{2.20}$$

The values of $[\delta x, \delta y, \delta z]$ are chosen to be very small, usually an order of magnitude smaller than the value chosen for Δs.

2.2 Reflection

As the ray of light travels in space, it interacts with different objects and travels from one medium to another. In the process of interacting with surrounding objects/media, a part of light is reflected and the remaining part is refracted. In this section, the geometrical representation of reflection is introduced followed by the details on refraction of light in

the next section.

The law of reflection states that an incident ray makes the same angle with the normal to the surface as the reflected ray. To model this on a computer, we define the reflection vector, $\mathbf{R_e}$ of a normalized incident vector $\mathbf{I}$. The two rays subtend the same angle with a given surface normal $\mathbf{N}$. The vectors $\mathbf{R}$, $\mathbf{I}$ and $\mathbf{N}$ all lie in the same plane so $\mathbf{R_e}$ can be expressed as a linear combination of $\mathbf{I}$ and $\mathbf{N}$.

$$\mathbf{R_e} = \alpha\mathbf{I} + \beta\mathbf{N} \tag{2.21}$$

From Figure 2.1, it is observed that the relation between the cosines of angles formed between $\mathbf{I}, \mathbf{N}$ and $\mathbf{R_e}, \mathbf{N}$, expressed as dot products of each pair of vectors, can be written as

$$-\mathbf{I}.\mathbf{N} = \mathbf{R_e}.\mathbf{N} \tag{2.22}$$

Substituting the value of $\mathbf{R_e}$ from Equation (2.21) in Equation (2.22) gives

$$\begin{aligned} -\mathbf{I}.\mathbf{N} &= \mathbf{N}.(\alpha\mathbf{I} + \beta\mathbf{N}) \\ &= \alpha\mathbf{N}.\mathbf{I} + \beta\mathbf{N}.\mathbf{N} \\ &= \alpha\mathbf{N}.\mathbf{I} + \beta \end{aligned} \tag{2.23}$$

where $\mathbf{N}.\mathbf{N} = 1$. If $\alpha = 1$, we obtain $\beta = -2(\mathbf{N}.\mathbf{I})$. The final reflection vector is given as

$$\mathbf{R_e} = \mathbf{I} - 2(\mathbf{N}.\mathbf{I})\mathbf{N} \tag{2.24}$$

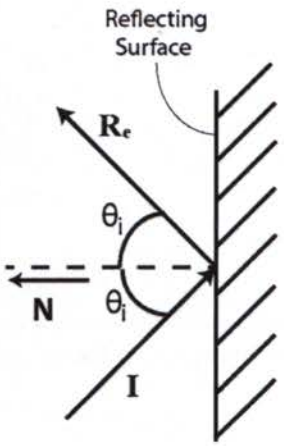

Figure 2.1: Reflection of light from a totally reflective surface. $\mathbf{I}, \mathbf{N}$ and $\mathbf{R_e}$ all lie in the same plane.

2.3 Refraction

The modeling of light transmission, like reflection, involves generating a new ray and tracing it through the optical medium. The light entering from one medium to another bends and travels in a new direction. The speed of light in a medium is dictated by the material's refractive index. Light travels the fastest in vacuum and slows down in denser mediums.

For some incident ray traveling along vector $\mathbf{I}$ in a surface with a refractive index, η_i, and normal, $\mathbf{N}$, the relationship of the angle of incidence, θ_i, to the angle of refraction, θ_t, is given by:

$$\eta_i \sin\theta_i = \eta_t \sin\theta_t \tag{2.25}$$

Since there are infinite number of refraction vectors that can make an angle of θ_t with the normal, $-\mathbf{N}$ we also add the constraint that the refracted vector, $\mathbf{R_f}$ is coplanar to both the surface normal and the incident vector and thus, is written as their linear combination.

$$\mathbf{R_f} = \alpha\mathbf{I} + \beta\mathbf{N} \tag{2.26}$$

From the Snell's law, it is derived (as shown in Figure 2.2)

$$\begin{aligned} \eta_i^2(1-\cos^2\theta_i) &= \eta_t^2(1-\cos^2\theta_t) \\ \eta_i^2(1-[\mathbf{N}.\mathbf{I}]^2) &= \eta_t^2(1-[-\mathbf{N}.\mathbf{R_f}]^2) \end{aligned} \tag{2.27}$$

Substituting for $\mathbf{R_f}$ from Equation 2.26 in Equation (2.27) gives:

$$\eta_i^2(1-[\mathbf{N}.\mathbf{I}]^2) = \eta_t^2(1-[\alpha(\mathbf{N}.\mathbf{I})+\beta]^2) \tag{2.28}$$

Since $\mathbf{R_f}.\mathbf{R_f} = 1$, it can also be deduced:

$$2\alpha\beta(\mathbf{N}.\mathbf{I}) + \beta^2 = 1 - \alpha^2 \tag{2.29}$$

Solving Equations (2.28) and (2.29) to find the values for α and β returns

$$\begin{aligned} \alpha &= \frac{\eta_i}{\eta_t} \\ \beta &= -\left(\frac{\eta_i}{\eta_t}\right)(\mathbf{I}.\mathbf{N}) - \sqrt{1+\left(\frac{\eta_i}{\eta_t}\right)^2[(\mathbf{I}.\mathbf{N})^2-1]} \end{aligned} \tag{2.30}$$

Finally, substituting the values of α and β from Equation (2.30) in Equation 2.26, one gets the refracted vector as:

$$\mathbf{R_f} = \frac{\eta_i}{\eta_t}\mathbf{I} - \left[\left(\frac{\eta_i}{\eta_t}\right)(\mathbf{I}.\mathbf{N}) + \sqrt{1+\left(\frac{\eta_i}{\eta_t}\right)^2[(\mathbf{I}.\mathbf{N})^2-1]}\right]\mathbf{N} \tag{2.31}$$

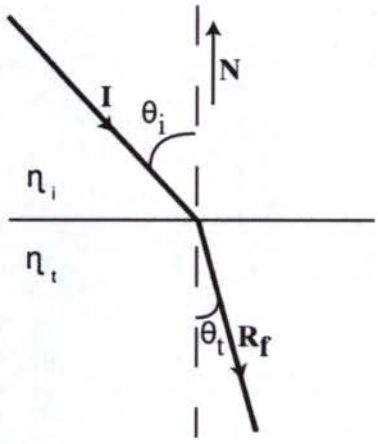

Figure 2.2: Light follows Snell's law as it travels from one medium (η_i) to another medium (η_t). Here, $\eta_i < \eta_t$.

2.4 Fresnel relations

A light ray incident on a boundary separating two media produces a reflected wave and a transmitted (refracted) wave. The vectors for calculating the reflected and refracted rays have been given in Equations (2.24) and (2.31), respectively. Fresnel relations uses Maxwell's equations to define the ratios of light energies that are reflected and transmitted.

The light wave is an electromagnetic wave that has an electric field component, $\mathbf{E}$, which is perpendicular to the magnetic field, $\mathbf{H}$. A light wave is either p-polarized or s-polarized. A p-polarized light has an electric field polarized parallel to the plane of incidence (given by $\mathbf{E}_{||}$), while in a s-polarized light, the electric field is perpendicular to this plane (given by $\mathbf{E}_{\perp}$). Light waves, like sunlight, are unpolarized due to the presence of equal ratios of p-polarized light and s-polarized light. The amount of incident sunlight reflected from the interface of two media is calculated by considering both cases of polarization [68]. The electric, $\mathbf{E}_{||}$ and magnetic field, $\mathbf{H}_{||}$ of a p-polarized light are expressed as

$$\begin{aligned} \mathbf{E}_{||} &= E_{||} \cos(\boldsymbol{k}.\boldsymbol{r} - \omega t)\boldsymbol{e}_1 \\ \mathbf{H}_{||} &= H_{||} \cos(\boldsymbol{k}.\boldsymbol{r} - \omega t)\boldsymbol{e}_2 \end{aligned} \tag{2.32}$$

where $\boldsymbol{e}_1$ and $\boldsymbol{e}_2$ are orthogonal to the propagation direction, $\boldsymbol{k}$. The spatial position of the wave is given by $\boldsymbol{r}$, the angular velocity by ω and time by t. Using Snell's Law from Equation (2.25), the transmitted electric field is related to the incident and reflected field

as shown in
Equation 2.33 and Figure 2.3.

$$\begin{aligned} E_{||i}\cos\theta_i - E_{||r}\cos\theta_r &= E_{||t}\cos\theta_t \\ H_{\perp i} + H_{\perp r} &= H_{\perp t} \end{aligned} \tag{2.33}$$

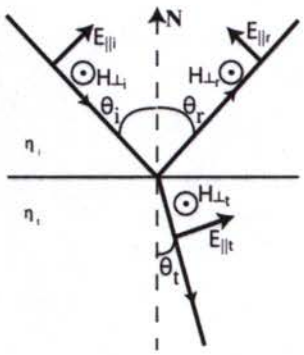

Figure 2.3: The electric and magnetic field components of a p-polarized light.

The magnetic and electric field amplitudes are related by $H_\perp = \frac{E_{||}}{v\mu}$ which gives

$$E_{||i} + E_{||r} = \frac{\mu_i}{\mu_t}\frac{v_i}{v_t}E_{||t} = \frac{\mu_i}{\mu_t}\frac{\eta_t}{\eta_i}E_{||t} = \frac{\hat{\eta}}{\hat{\mu}}E_{||t} \tag{2.34}$$

where $\hat{\mu} = \frac{\mu_t}{\mu_i}$ is the ratio of magnetic permeabilities for transmission and incident media and $\hat{\eta} = \frac{\eta_t}{\eta_i}$ is the ratio of refractive indices for transmission and incident media and v_i and v_t are the magnitudes of velocities of light in the incident and transmitted media. Equations (2.33) and (2.34) are solved simultaneously to give the following relations for Fresnel's reflection and transmission coefficients

$$\begin{aligned} r_{||} &= \frac{E_{||r}}{E_{||i}} = \frac{\frac{\hat{\eta}}{\hat{\mu}}\cos\theta_i - \cos\theta_t}{\frac{\hat{\eta}}{\hat{\mu}}\cos\theta_i + \cos\theta_t} \\ t_{||} &= \frac{E_{||t}}{E_{||i}} = \frac{2\cos\theta_i}{\cos\theta_t + \frac{\hat{\eta}}{\hat{\mu}}\cos\theta_i} \end{aligned} \tag{2.35}$$

For the case of s-polarized light, the electric field is perpendicular to the plane of incidence. The electric and magnetic field system of equations is given as

$$\begin{aligned} E_{\perp i} + E_{\perp r} &= E_{\perp t} \\ H_{||i}\cos\theta_i - H_{||r}\cos\theta_r &= H_{||t}\cos\theta_t \end{aligned} \tag{2.36}$$

The second equation in Equation (2.36) is related to $E_\perp$ as

$$E_{\perp i}\cos\theta_i - E_{\perp r}\cos\theta_r = \frac{\mu_i}{\mu_t}\frac{v_i}{v_t}E_{\perp t}\cos\theta_t = \frac{\mu_i}{\mu_t}\frac{\eta_t}{\eta_i}E_{\perp t}\cos\theta_t = \frac{\hat{\eta}}{\hat{\mu}}E_{\perp t}\cos\theta_t \tag{2.37}$$

Solving for the Fresnel's reflection and transmission coefficients from Equations (2.36) and (2.37) gives

$$\begin{aligned} r_\perp &= \frac{E_{\perp r}}{E_{\perp i}} = \frac{\cos\theta_i - \frac{\hat{\eta}}{\hat{\mu}}\cos\theta_t}{\cos\theta_i + \frac{\hat{\eta}}{\hat{\mu}}\cos\theta_t} \\ t_\perp &= \frac{E_{\perp t}}{E_{\perp i}} = \frac{2\cos\theta_i}{\cos\theta_i + \frac{\hat{\eta}}{\hat{\mu}}\cos\theta_t} \end{aligned} \tag{2.38}$$

Using Snell's law, the reflection coefficients, $r_{||}$ and $r_\perp$, in Equations (2.35) and (2.38) are expressed as

$$\begin{aligned} r_{||} &= \frac{\frac{\hat{\eta}}{\hat{\mu}}\cos\theta_i - \left[1 - \frac{1}{\hat{\eta}^2}\sin^2\theta_i\right]^{1/2}}{\frac{\hat{\eta}}{\hat{\mu}}\cos\theta_i + \left[1 - \frac{1}{\hat{\eta}^2}\sin^2\theta_i\right]^{1/2}} \\ r_\perp &= \frac{\cos\theta_i - \frac{\hat{\eta}}{\hat{\mu}}\left[1 - \frac{1}{\hat{\eta}^2}\sin^2\theta_i\right]^{1/2}}{\cos\theta_i + \frac{\hat{\eta}}{\hat{\mu}}\left[1 - \frac{1}{\hat{\eta}^2}\sin^2\theta_i\right]^{1/2}} \end{aligned} \tag{2.39}$$

The total reflectance, $\mathfrak{R}$, of unpolarized light from the interface of two media is

$$\mathfrak{R} = \frac{1}{2}(r_{||}^2 + r_\perp^2) \tag{2.40}$$

Finally, the fraction of unpolarized light transmitted is simply $(1 - \mathfrak{R})$.

2.5 Plastic Optical Fibers (POF)

Optical fibers have been extensively used for short distance and long distance communications. The flexibility and ease of handling plastic optical fibers compared to glass optical fibers makes them suitable for this research. An optical fiber generally consists of either two layers (core and cladding) or three layers (core, cladding and jacket). The jacket acts as a protective layer for the entire fiber. The light travels in the core of the fiber while

the cladding works in unison with the core to keep the light contained within the fiber. The optical fibers, for the TC panels constructed in a lab in UC-Berkeley, only had the core and the cladding layers since the jacket layer does not transmit light. Also the price of a batch of jacketless optical fibers was lower which helped in reducing the material costs. The composition of these optical fibers contained a PolyMethylene MethAcrylate (PMMA) core protected by a perfluorinated (PF) cladding of small thickness (Figure 2.4). In general the refractive index of the cladding is less than that of the core; a requirement necessary to initiate Total Internal Reflection which is discussed in the next section. Also, in the case of plastic optical fibers, refractive indices vary slightly over a range of wavelengths [25]. A refractive index of 1.49 for the core and 1.40 for the cladding were provided by the manufacturer of the considered type of fiber with a numerical aperture, $N.A. = \sqrt{\eta_{core}^2 - \eta_{cladding}^2}$ of 0.51. A complete discussion on the modeling of refractive indices for the different kinds of fibers is given in Appendix B.

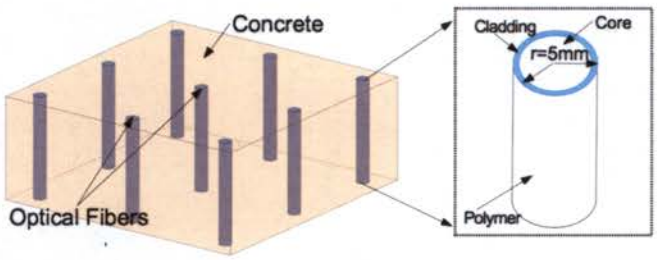

Figure 2.4: A computational model of the TC panel with embedded optical fibers (optical fiber illustration not to scale). The optical fiber has two layers: inner core and outer cladding.

Total Internal Reflection

Total Internal Reflection (TIR) is a phenomenon which occurs when a propagating wave strikes a medium boundary at an angle larger than the computed critical angle measured with respect to the normal to the surface. Necessary conditions for TIR are that the two involved media should be in contact with each other and the refractive index of the medium from which the light wave tends to exit should be greater than the index of the refracting medium. The critical angle for the POF described above will depend on the refractive indices of the core ($\eta_{core} = 1.49$) and the cladding ($\eta_{cladding} = 1.40$). The critical angle is calculated as:

$$\theta_c = \sin^{-1}\left(\frac{1.40}{1.49}\right) \approx 70^\circ \tag{2.41}$$

A POF allows two types of light rays: meridonial rays and skew rays. Meridonial rays are rays that are confined to the plane containing the axis of the POF and the point from where the ray originated. Meridonial rays always pass through the optical axis. Skew rays, on the other hand, travel in a non-planar spiral path and never cross the axis of the POF. Figure 2.5 shows the trajectories followed by both types of rays. It is also observed from Figure 2.6 that the transmission of meridonial rays is dependent on the $N.A.$ of the optical fiber. For the type of fiber considered here, the value of $N.A. = 0.51$. This implies that any meridonial ray will only be transmitted through the fiber if the angle of incidence it makes with the fiber axis at its entrance is less than or equal to $\sin^{-1}(N.A) = 30.66°$. This constraint does not apply to skew rays and is also observed in Figure 2.6 where the skew rays were also transmitted beyond the transmission angle set by $N.A.$.

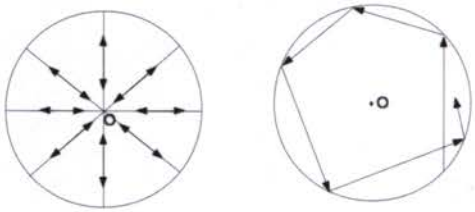

Figure 2.5: a) Meridonial rays cross the axis of fiber after reflection from the fiber wall. b) Skew rays travel in a spiral path and do not cross the axis of the fiber.

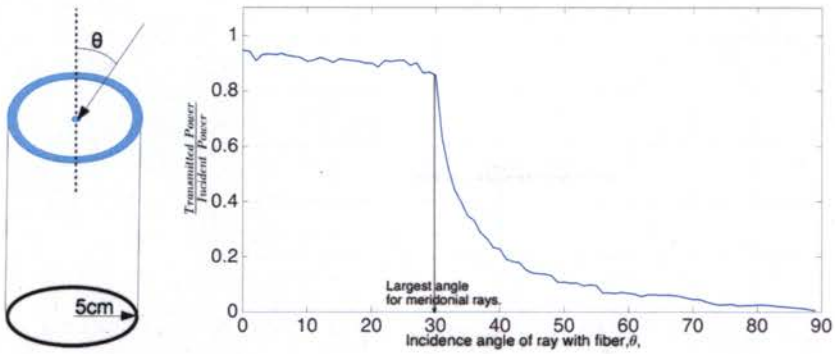

(a) (b)

Figure 2.6: (a) Light ray incident at an angle θ with the face of an optical fiber (b) Percentage of light that is transmitted for different incidence angles subtended with the entrance face of the fiber.

The transmitted power in Figure 2.6b is the light intensity that exits the optical fiber normalized to the incident power.

2.6 Loss of light in optical fibers

As light travels through the core, it suffers two types of intrinsic losses [69]:

1. Rayleigh scattering in the fiber from the random density fluctuations caused by irregular microscopic structure of the fiber. This loss is inversely proportional to the fourth power of the wavelength. For a PMMA core, the relation for loss factor is mentioned in [31] as $\alpha_R = 13 \times \left(\frac{633}{\lambda}\right)^4 dB/km$.

2. Light absorption from electronic transitions between the excited and the ground state (Urbach's rule). Loss factor, in this case is expressed as $\alpha_e = 1.58 \times 10^{-12} \exp(\frac{1.15 \times 10^4}{\lambda})$ dB/km from [32].

Light absorption leads to heating up of the optical fiber, whereas the radiation dissipated via the scattering process is rejected from the optical fiber. The significant terrestrial radiation (280 nm-4000 nm) is broken into 3 spectra: Ultraviolet (UV) range (280 nm-380 nm), visible light (380 nm-780 nm) and infrared (IR) range (780 nm-4000 nm) of solar radiation. The intrinsic transmittance of a PMMA optical fiber with rays having an average optical path length of L (in km) is calculated by applying Equation (2.42) as given in

[34] to each spectrum of terrestrial radiation.

$$T(L) = \frac{\int_{\lambda_1}^{\lambda_2} E_o(\lambda) \exp(-(\alpha_R + \alpha_e)L) d\lambda}{\int_{\lambda_1}^{\lambda_2} E_o(\lambda) d\lambda} \tag{2.42}$$

where the solar spectral distribution as a function of the wavelength (λ) is defined as $E_o(\lambda) = \frac{C_1}{\lambda^5[\exp(C_2/\lambda)-1]}$ with $C_1 = 8.097 \times 10^{-21}\ Wm^2$ and $C_2 = 2.497 \times 10^{-6}\ m$. The outcome of applying 2.42 is to calculate the attenuation in the intensity of each ray as a function of the length travelled by the ray in an attenuating medium like an optical fiber.

Modeling roughness in optical fibers

The roughness is quantified by the deviations in the direction of the normal vector of a real surface from its ideal form. Roughness plays an important role in determining how light will interact with the fiber. During the construction process of the TC panels, the fibers are cut and sanded. This causes the top and bottom surfaces of the fibers to be produced unevenly. The surface roughness at the two ends of the fiber can change the incidence angle of a light ray. The interaction of light ray with surface asperities is modeled as a random variable with two states, say 0 and 1, and upon having say '1', a new normal is randomly and uniformly generated which is considered to be orthogonal to the irregularity. This simulates the condition that the light ray encounters an asperity on the fiber surface half of the time and the normal to the asperity can be directed in any direction.

2.7 Summary of Algorithm

The entire algorithm of geometrical ray tracing is summarized in Figure 2.7

Steps to perform Ray Tracing

1. Define the position and velocity of N light rays in the medium at time $t = 0$.
2. Advance the light rays in the medium by using Equations (2.16), (2.17) and (2.18)
3. Update time using Equation (2.19)
4. If a ray encounters a new medium
   i) Solve for the point of intersection of the ray with the interface of the two media. Let the intersection point be (x_1, x_2, x_3)
   ii) Compute the normal to the interface surface. For a surface, Φ, describing the interface, the normal is given as $\mathbf{N} = \frac{\nabla\Phi(x_1,x_2,x_3)}{\|\nabla\Phi(x_1,x_2,x_3)\|_{L2}}$
   iii) Compute the reflected ray ($\mathbf{R_e}$) and refracted ray ($\mathbf{R_f}$) with respect to the normal using Equations (2.24) and (2.31). (The incident ray ($\mathbf{I}$), reflected ray ($\mathbf{R_e}$), refracted ray ($\mathbf{R_f}$) and normal ($\mathbf{N}$) should all lie in the same plane)
   iv) Determine if there is a possibility of TIR by comparing incidence angle with critical angle from Equation (2.41):
      - If there is TIR: Light is totally internally reflected. Calculate $\mathbf{R_e}$ using Equation (2.24).
      - If TIR is not achieved: A fraction of light is refracted while the remaining fraction is reflected. Calculate $\mathbf{R_e}$ using Equation (2.24) and $\mathbf{R_f}$ using Equation (2.31).
   v) Calculate the losses incurred by the light rays inside the medium due to scattering (α_R), absorption (α_e) and interface roughness.
5. Update all ray front positions using Equations (2.16), (2.17) and (2.18).
6. Repeat steps (4) and (5) until all the rays have reached their destination.

Figure 2.7: Algorithm for ray tracing method.

Example

The method presented in Figure 2.7 was applied to the case of a Translucent Concrete (TC) panel which consists of two materials, concrete and optical fibers. The sequence of light propagation in the TC panel is shown in Figure 2.8. The optical fiber is a transparent medium while concrete is opaque. As can be observed from the figure, a fraction of light rays (represented by arrows) interacting with concrete is reflected from the surface. The remaining fraction is absorbed by concrete. On the other hand, optical fibers allow light rays to enter into the tube and travel through the tube by TIR.

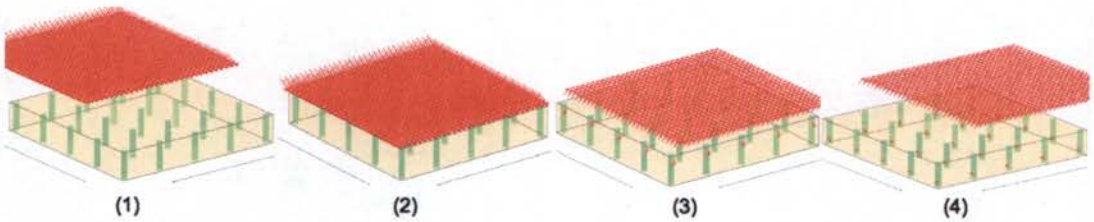

Figure 2.8: Ray tracing in a TC panel (1) The rays are travelling towards the TC panel (2) The rays intersect with the top of the panel (3) A fraction of the rays enter into the optical fibers while the rest are reflected away from the TC panel (4) The rays that enter into the optical fibers are channeled through it while the remaining rays travel further away from the panel.

2.8 Summary

In this chapter, the following remarks can be made:

1. Geometrical ray tracing is derived from the Eikonal equation for light.
2. A forward Euler method is developed to march rays in space as they travel in different media.
3. When a ray strikes the face of an optical fiber, it reflects some of its light and refracts the remaining fraction of light energy. This phenomenon can be quantified using Fresnel Relations.
4. Rays propagate inside an optical fiber using Total Internal Reflection (TIR).
5. The TIR condition is dependent on the critical angle of the selected optical fiber.

6. Loss of light occurs inside fiber due to scattering, absorption and roughness of the fiber.

7. A ray tracing algorithm considering all above points is developed and applied to an example of a Translucent Concrete (TC) panel with embedded optical fibers.

Chapter 3

Solar Radiation Models

The ray tracing algorithm for a TC panel is coupled with a solar radiation model to estimate the amount of sunlight that is transmitted by the panel. This requires precise measurements or calculations of the components (direct and diffused) of sunlight that are incident on the surface of the TC panel. A number of empirical, analytical and measurement-based methods have been developed in the past that tries to compute these components. The empirical relations are only specific to a certain region in the world and the analytical methods are useful in situations where one does not have data for sunlight that is incident on the surface of Earth. Since empirical methods are easy to implement, they are still widely used. Some of them include the H-model [18], S-model [61], B-model [6] which are applied to calculate clear-sky global solar irradiance. The analytical methods are sophisticated formulations that require a number of parameters to calculate the global solar irradiance incident on a surface. The two popular analytical methods are Leckners spectral model [35] and Gueymards Simple Model for the Atmospheric Radiative Transfer of Sunshine-SMARTS2 [12]. For locations with weather stations, the weather file (also called Typical Meteorological Year file) can provide statistically representative information for the sunlight incident during the entire year. The measurement-based methods extract the hourly data for sunlight irradiances/illuminances from the weather file and differentiate the values into its components (direct and diffused radiation). The following sections detail a measurement-based method called the 'Perez Model' which is interfaced with the ray tracing algorithm for calculating the light transmission of a TC panel. The Perez Model has been frequently found to be the most robust model among all the different types of measurement-based methods.

3.1 Radiation from the Sun

At the top of the Earth's atmosphere, the light from the Sun is incident as a nearly parallel beam of rays referred to as the extraterrestrial solar irradiation (G_{etr}). The G_{etr} fluctuates over the year due to Earth's varying distance from the Sun. The best mean estimate of G_{etr} is 1366.1 W/m^2 which has been derived from 25 years of collected data [13]. The variation in the G_{etr} over the year depends on the position of the Earth in its elliptical orbit around the Sun. It is given as

$$G_{etr} = 1366.1\left(1 + 0.034\cos\frac{2\pi(N-2)}{365}\right)\ W/m^2 \tag{3.1}$$

where N is a Julian day between $[1, 365]$. Equation (3.1) can also be applied to calculate the extraterrestrial solar illuminance by replacing the mean value of 1366.1 W/m^2 for G_{etr} with a mean illuminance value of 133100 lx. The illuminance (units: lx) is the amount of visible light flux incident on a unit surface area and the irradiance (units: W/m^2) is defined as the total light power striking on a unit surface area. From this point onwards, the terms, illuminance and irradiance will be used interchangeably and the reader is requested to differentiate between the two quantities based on the context or the units used.

Outside the Earth's atmosphere, the distribution of the solar flux with respect to the wavelength is termed AM0 meaning no atmosphere is present. The solar radiation is affected by absorption and scattering processes that occur as it travels through the Earth's atmosphere. This mass of atmosphere is referred to as AM1.5. The complex effect of AM1.5 separates the beam of sunlight into different components that are discussed in Section 3.2. The spectral distribution for sunlight after transiting the atmosphere is presented in Figure 3.1, which is used later in radiation calculations for the TC panel.

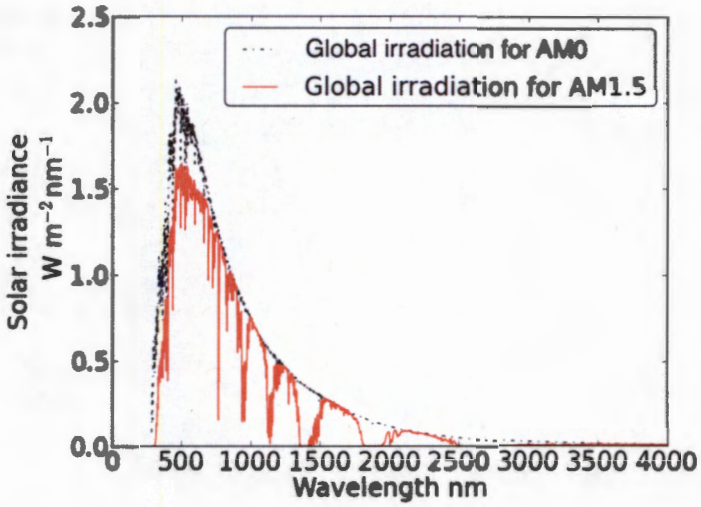

Figure 3.1: Spectral distribution for solar radiation in AM0 and AM1.5 [13].

Remark: The AM1.5 calculations are standard curves that have been adopted by the American Society for Testing Materials (ASTM) for testing terrestrial solar cells.

3.2 Solar radiation incident on the Earth's surface

The solar radiation incident on the Earth's surface consists of direct and diffused components. The direct component is that part which directly reaches the Earth's surface from the Sun. The diffuse component is generated by scattering solar radiation from the small molecules of Hydrogen (H_2) and Nitrogen (N_2) in the atmosphere. The following quantities associated with solar radiation are measured:

1. Direct beam irradiance/illuminance (G_n) which is the energy flux (in W/m^2 or lx) of the solar radiation incoming from the Sun on a surface that is perpendicular to the rays.

2. Direct horizontal irradiance/illuminance (G_b) is the component of G_n that is projected on a flat horizontal plane. Since the incidence angle of the Sun's beam striking the horizontal ground is given by the zenith angle, θ_z, therefore

$$G_b = G_n \cos\theta_z \tag{3.2}$$

3. Diffuse irradiance/illuminance (G_d) represents the energy flux coming from the entire sky dome on a horizontal surface, which excludes the direct beam coming from Sun's beam.

4. Global irradiance/illuminance (G) is the sum of direct horizontal (G_b) and diffuse (G_d) components of the sunlight irradiance. For a panel that is tilted at an angle β with respect to the horizontal, G is expressed as follows

$$G = G_b \frac{\cos\theta}{\cos\theta_z} + G_d \tag{3.3}$$

where θ is the incidence angle between the sun direction and normal to the panel surface.

The incidence angle, θ, for an arbitrarily oriented surface with a surface azimuth angle, μ and solar azimuth angle, a_z is expressed as:

$$\cos\theta = \cos\theta_z \cos\beta + \sin\theta_z \sin\beta \cos(\mu - a_z) \tag{3.4}$$

For the case of a south facing panel, $\mu = 180°$ which reduces θ in Equation (3.4) to:

$$\theta = \cos^{-1}(\cos\theta_z \cos\beta - \sin\theta_z \sin\beta \cos a_z) \tag{3.5}$$

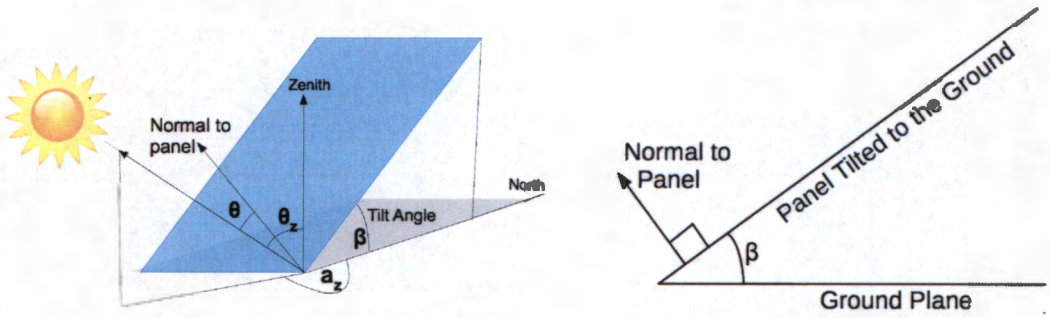

(a) θ is the angle between normal to the panel and the sun

(b) Side View

Figure 3.2: Setup for a tilted TC panel.

Weather stations in the United States record the direct beam irradiance/illuminance ($G_n = G_b/\cos\theta_z$) component of sunlight which is also the direct horizontal flux of the sun at

zenith. Accordingly, Equation (3.3) is modified to yield:

$$G = G_n \cos\theta + G_d \tag{3.6}$$

The total irradiance/illuminance (G) on a tilted surface also includes an additional component due to radiation reflected from the ground (G_r). This reflected radiation does not account for a significant part of the sunlight striking the surface and is hence, ignored in Equation (3.6).

3.3 Literature review

The measurement-based methods differ in nature by the way in which they calculate the diffuse component. The simplest model was proposed back in the 1960s by Liu et al. [37] which was referred as to the isotropic sky model. It assumed that all diffused radiation was uniformly distributed over the sky dome. The incident diffused irradiation, G_d, was only dependent on β which decided the part of panel that will be blocked from the view to sky. As can be seen from Equation (3.7), when $\beta = 90°$, the value of $G_d = 0.5G_d(0)$ meaning that the surface of the vertical panel is only exposed to half of the sky.

$$G_d = G_d(0)\frac{(1+\cos\beta)}{2} \tag{3.7}$$

where $G_d(0)$ represents the diffused solar irradiation incident on the horizontal plane and its value is specified in the weather file [8].

The Hay model [15] proposed some improvements by adding a circumsolar component to the isotropic sky model. This was the first model that introduced anisotropy in diffused radiation. The circumsolar component is assumed to come from the sun being a visible disk of light source rather than just a point source in the sky. The diffused irradiation, G_d, was calculated as the weighted average of the extreme states, clear sky and overcast sky. As shown in Equation (3.8), G_d depended on θ_z which varied due to the latitude of the location.

$$G_d = G_d(0)\left[\frac{1+\cos\beta}{2}(1-F_a) + \frac{\cos\theta}{\cos\theta_z}F_a\right] \tag{3.8}$$

where $F_a = G_b/G_{etr}$ is the factor to quantify the fraction of diffused radiation that is circumsolar. For a clear sky ($F_a > 0.5$), the model assumed that the majority of the solar energy came from the Sun's position while in overcast sky ($F_a \to 0$), the model assumed that the solar radiation was uniformly distributed in the sky. Thus, Hay's model reduced

to the Liu and Jordan model in the case of an overcast sky.

A further improvement in the solar radiation model considered horizon brightening and used the same factor F_a as described in Equation (3.8). This model proposed by Reindl et al. [57] is expressed in Equation (3.9). It provided slightly higher diffused irradiances than the Hay's model.

$$G_d = G_d(0)\left[\frac{1+\cos\beta}{2}(1-F_a)\left(1+\left(1-\frac{G_d(0)}{G(0)}\right)^{1/2}\sin^3\frac{\beta}{2}\right)+\frac{\cos\theta}{\cos\theta_z}F_a\right] \quad (3.9)$$

where $G(0)$ is the global solar irradiation on a horizontal plane. More recent models have been proposed by Muneer [45], Olmo et al. [49], Noorian et al. [48], Ibrahim et al. [22]. However, on the whole, in numerous locations of the world, the Perez Sky model (discussed in the next section) is frequently found to be the best performing model [52].

3.4 Perez Sky model and the modified form

Under the Perez Sky model assumption [53], the diffuse solar radiation (G_d) on a tilted surface is calculated as the sum of the following components (Figure 3.3):

1. Isotropic radiation which is uniformly distributed over the sky vault.
2. Radiations from circumsolar disk and horizon brightening which cause anisotropic distributions of diffused light.

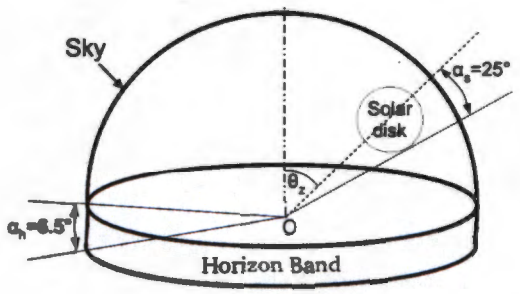

Figure 3.3: Description of Perez circumsolar radiation and horizon radiation band.

The circumsolar disk subtends a half angle of 25° around the sun produced from forward scattering by aerosols and multiple Rayleigh scattering. A bright band of 6.5° elevation

develops near the horizon because of sunlight retroscattering. The contribution of each component (isotropic, circumsolar or horizon brightening) in the final equation for diffused light depends on the sky brightness factor, Δ, atmospheric clearness, ϵ, and zenith angle, θ_z. Hence, G_d for a tilted surface is expressed as:

$$G_d = G_d(0)\left[(1 - F_1)\frac{1 + \cos\beta}{2} + F_1\frac{\cos\theta}{\cos\theta_z} + F_2\sin\beta\right] \tag{3.10}$$

where

$$F_1(\epsilon) = f_{11} + f_{12}\Delta + f_{13}\theta_z, \quad F_2(\epsilon) = f_{21} + f_{22}\Delta + f_{23}\theta_z \tag{3.11}$$

and

$$\Delta = \frac{mG_d(0)}{G_{etr}}, \epsilon = \frac{G_d(0) + G_n(0)}{G_d(0)} \tag{3.12}$$

The coefficients f_{ij} in Equations (3.11) are listed in Table 3.1.

Table 3.1: Coefficients for circumsolar irradiation (or illumination) and horizon brightening developed for the 25° circumsolar model [53].

ϵ bin	Upper limit of ϵ	f_{11}	f_{12}	f_{13}	f_{21}	f_{22}	f_{23}
1	1.056	-0.011	0.748	-0.080	-0.048	0.073	-0.024
2	1.253	-0.038	1.115	-0.109	-0.023	0.106	-0.037
3	1.586	0.166	0.909	-0.179	0.062	-0.021	-0.050
4	2.134	0.419	0.646	-0.262	0.140	-0.167	-0.042
5	3.230	0.710	0.025	-0.290	0.243	-0.511	-0.004
6	5.980	0.857	-0.370	-0.279	0.267	-0.792	0.076
7	10.080	0.734	-0.073	-0.228	0.231	-1.180	0.199
8	> 10.08	0.421	-0.661	0.097	0.119	-2.125	0.446

In the above relations, m is the atmospheric air mass coefficient which is the direct optical path length through the Earth's atmosphere, expressed as a ratio relative to the path length vertically upwards, *i.e.* at zenith. For clarity, in Figure 3.4 the light coming from the Sun's position S_1 will suffer lesser scattering and absorption due to optical mass as compared to light that emanates from a point S_2 which is farther from point P on Earth.

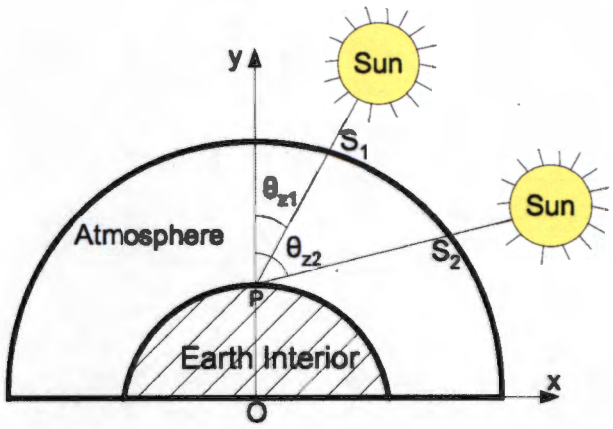

Figure 3.4: Optical mass, m, is dependent on the path length through the atmosphere. Since $PS_2 > PS_1$, light will suffer higher scattering and absorption along PS_2.

To estimate, m, the formulation proposed by Kasten and Young [33] was used leading to the following expression:

$$m = \frac{1}{\cos(\theta_z) + 0.50572(96.07995 - \theta_z \frac{180}{\pi})^{-1.6364}} \tag{3.13}$$

Modified Perez model for illuminance calculations

The TC panel contains cylindrical optical fibers that exhibit a limited acceptance cone ,*i.e* light is lost if rays fall outside the acceptance angle of this cone, for light transmission (Figures 2.4 and 2.6). This loss of light is in addition to the light reflection at the top and bottom surfaces and losses during transit within fiber. Thus, all components of incident global illuminance (G) cannot be transmitted through the fiber equally. The ratio of each component (direct, isotropic, etc.) that is transmitted through a TC panel is calculated using geometrical ray tracing (Chapter 2). These ratios are included in the modified form of Equations (3.6) and (3.10) to give Equations (3.14)

$$\begin{aligned} G' &= D_n G_n \cos\theta + G'_d \\ G'_d &= G_d(0)\left[D_i(1-F_1)\frac{1+\cos\beta}{2} + D_c F_1 \frac{\cos\theta}{\cos\theta_z} + D_h F_2 \sin\beta\right] \end{aligned} \tag{3.14}$$

where G' and G'_d represent the global and diffused illuminances, respectively, collected on a surface adjoining and parallel to the TC panel. D_n, D_i, D_c and D_h are the averaged TC panel transmittance ratios for their respective global illumination components. Finally, G'

and G'_d are multiplied by the area of the TC panel to give the total luminous flux (in lm) value. This is the light that is delivered into a room by a TC panel. A detailed algorithm given in Figure 3.5 combines the geometrical ray tracing discussed in Chapter 2 with the modified Perez Sky model to estimate the total luminous flux (or energy flux) transmitted by the TC panel.

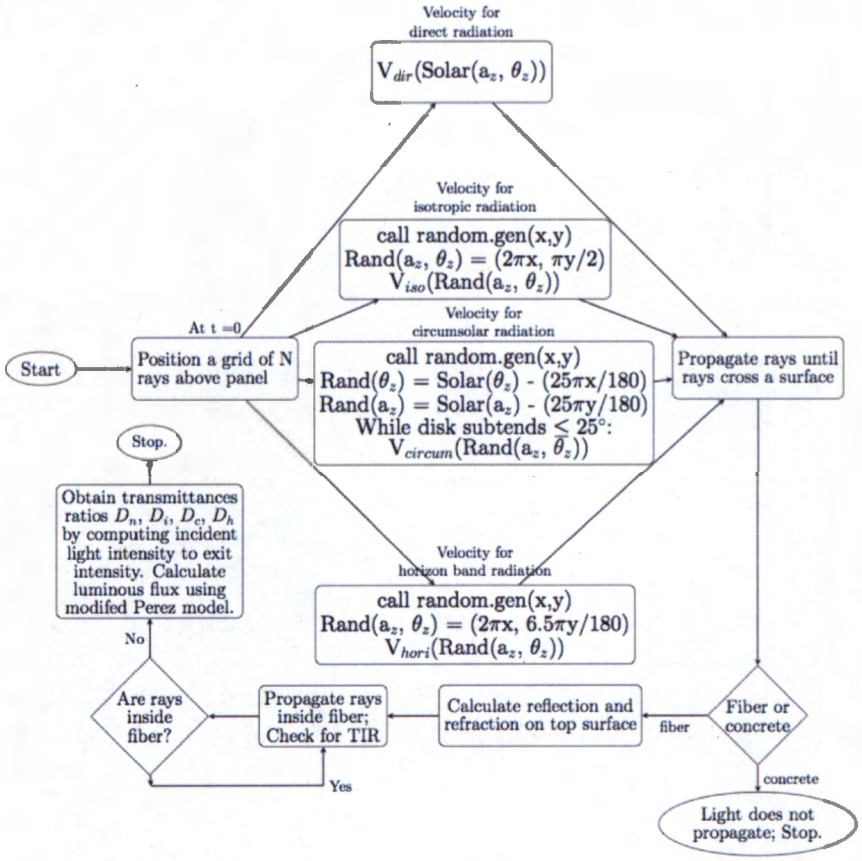

Figure 3.5: Algorithm for calculation of the total flux emitted from a TC panel. The velocities (V_{dir}, V_{iso}, V_{circum}, V_{hori}) refer to the speed and direction of N groups of light rays that are projected towards TC from their source of generation, *i.e.* direct, isotropic, circumsolar and horizon brightening, respectively.

Extension to Heat Radiation and Absorption

The same relations presented in Equations (3.14) and the algorithm in Figure 3.5 can be utilized with slight modifications to calculate the heat radiated and absorbed by the optical fibers inside the TC panel which leads to its gradual heating during the day. The heat absorbed is modeled as a source of heat distributed uniformly along the optical fiber length. This heat is conducted within the TC panel and convected into the room depending on the boundary conditons. The total amount of heat absorbed by the fibers is given as follows:

$$E_f = E_{direct} + E_{diffused} \tag{3.15}$$

where,

$$\begin{aligned} E_{direct} &= \chi_n G_n \cos\theta \\ E_{diffused} &= G_d(0)\left[\chi_i(1-F_1)\frac{1+\cos\beta}{2} + \chi_c F_c \frac{\cos\theta}{\cos\theta_z} + \chi_h F_2 \sin\beta\right] \end{aligned} \tag{3.16}$$

where the coefficients χ_r $(r = n, i, c, h)$ in the heat absorption Equation (3.16) are obtained slightly differently from the corresponding D coefficients used for illuminance (Equation (3.14)). Illuminance only pertains to the visible region of the light spectrum whereas in heat calculations, one has to consider the absorption of light rays for the enitre spectrum. The radiation transmitted by the TC panel can be written using Equation (3.17) with coefficients τ_r $(r = n, i, c, h)$ that modulate the transmission of solar energy by optical fibers.

$$q_{rad} = \tau_n G_n \cos\theta + G_d(0)\left[\tau_i\left(1-F_1\right)\frac{1+\cos\beta}{2} + \tau_c F_1 \frac{\cos\theta}{\cos\theta_z} + \tau_h F_2 \sin\beta\right] \tag{3.17}$$

The coefficients τ_r are related to D_r $(r = n, i, c, h)$ as

$$\tau_r G_{\bar{r}} = (T_{UV} G_{\bar{r},UV} + T_{vis} G_{\bar{r},vis} + T_{IR} G_{\bar{r},IR}) D_r \tag{3.18}$$

where $G_{\bar{r}}$ can be either G_n or $G_d(0)$ depending on the type of solar radiation (direct or diffused) being considered (*i.e.* $\bar{r} = n$ if $r = n$ and $\bar{r} = d$ if $r = i, c, h$). The values T_{UV}, T_{vis} and T_{IR} are the transmittance ratios for the UV, visible and infrared spectrum, respectively.The flowchart in Figure 3.6 gives the procedure to obtain the χ_r $(r = n, i, c, h)$ coefficients in order to calculate Equation (3.16).

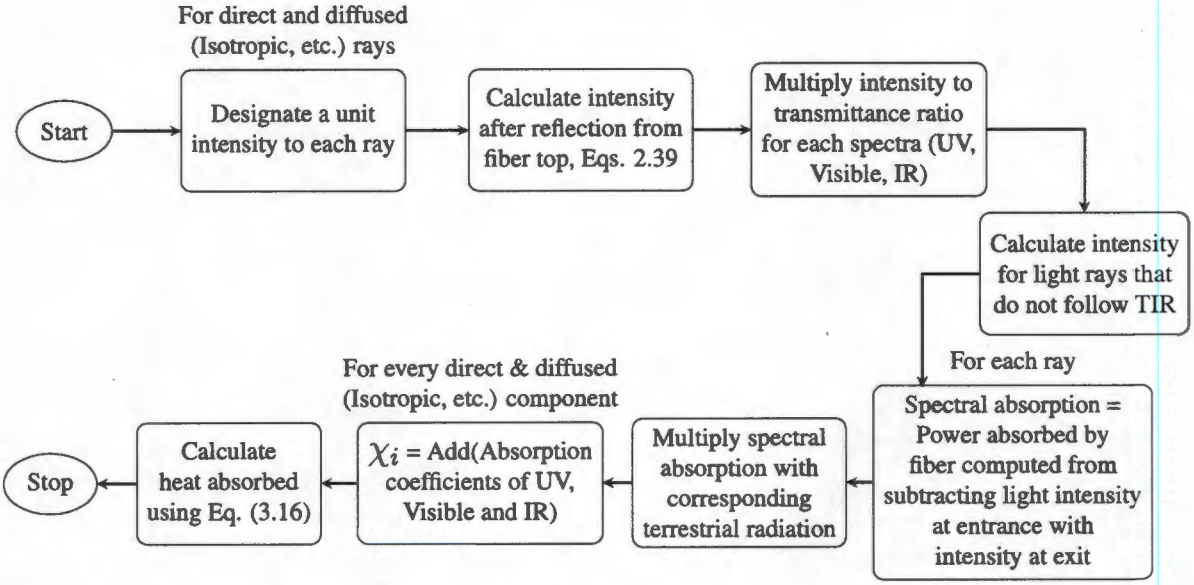

Figure 3.6: Algorithm to calculate the heat absorption by the TC panel.

3.5 Summary

The topics discussed in this chapter can be summarized as follows:

1. The solar radiation passes through the atmosphere and becomes attenuated due to the presence of gases in the air.
2. Solar radiation incident on earth consists of direct and diffused components.
3. The direct radiation originates from the Sun and is the dominant component during a clear sky. The diffused component is produced from scattering of light as it passes the atmosphere. Diffused light is more observable during cloudy skies.
4. The diffused radiation is further split into the isotropic and the anisotropic components (Circumsolar radiation and horizon brightening).
5. The ratio of the components of diffused light for a given location and sky condition can be computed using the Perez Sky model [53].
6. Two algorithms developed for computing the amounts of light transmitted and heat radiation absorbed by the TC panel based on the sky conditions are presented.

Chapter 4

Illumination Calculations using Radiance

RADIANCE is a widely used open source software developed by Lawrence Berkeley National Laboratory (LBNL) for visualizing lighting in a defined space. It has highly-accurate ray tracer engine that can predict illumination, visual quality and appearance in innovative design spaces. In this chapter, *RADIANCE* is used to evaluate the illumination distribution of light that is emitted from a wall composed of TC material. To model the optical fibers in TC, *RADIANCE* requires its luminaire properties which are unfortunately not available in the software. The properties are evaluated using the ray tracing software developed as part of this report (Chapter 2) which is coupled with the directionality of light that is transmitted from the optical fibers. These values are then entered into *RADIANCE* for calculating illumination of the modeled space due to the TC panels.

4.1 Luminaire in lighting

A luminaire is defined as a lighting unit consisting of a lamp or lamps combined together with the parts designed to distribute the light. For a luminaire with a given shape and material properties, we can calculate its lighting parameters, which include:

i). Luminous intensity distribution (I_c) (Units: *candela* or *cd*): It is the distribution curve representing the variation of luminous intensity of a lamp or luminaire in a plane through the light center. The distribution curve is usually measured by a photometer with moving cell along the various C-planes (Figure 4.1). A C-plane is defined as a surface along which light measurements are taken. The C-plane is divided into a number of γ angles. Figure 4.2 shows an example of a flat luminaire with its C-planes and γ angles.

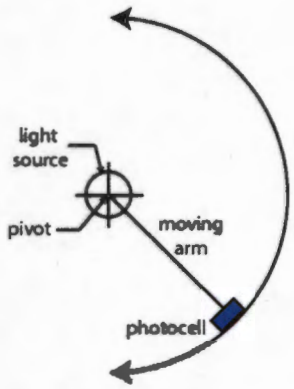

Figure 4.1: A moving photometer for calculating luminous intensity distribution.

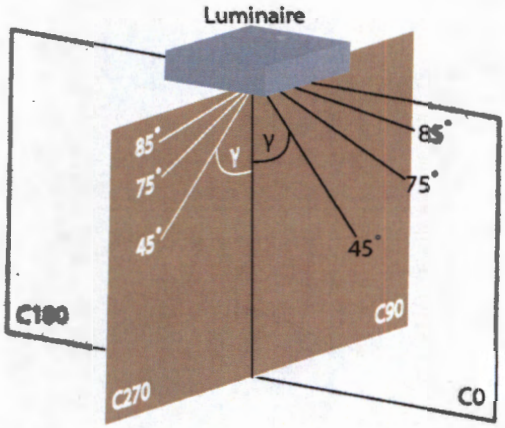

Figure 4.2: The measurements of a luminaire are taken along its C-planes and γ angles. In the figure, we consider the (C0-C180 plane) and (C90-C270 plane).

ii). Luminous flux (Φ) [Units: *lumen* or *lm*]: This quantity is either calculated directly using Integrating Spheres or calculated from the lighting intensity distribution of the luminaire (I_c). The total luminous flux (Φ) means that the part of the flux, $\Delta\Phi$, is distributed among several solid angles, $\Delta\omega$, spread across multiple C-planes. Thus, in general, we can represent Φ over n $\Delta\omega$'s which are added for m C-planes to give the following:

$$\Phi = \sum_{C_0}^{C_{m-1}} \sum_{i=1}^{n} \Delta\Phi_{\Delta\omega_i} \tag{4.1}$$

The luminous intensity for a solid angle is given as $I_{c(\Delta\omega_i)}$ which is defined as the luminous flux, $\Delta\Phi$, emitted into a solid angle, $\Delta\omega_i$ as expressed below:

$$\Delta\Phi_{\Delta\omega_i} = I_{c(\Delta\omega_i)}.\Delta\omega_i \tag{4.2}$$

where $I_{c(\Delta\omega_i)}$ is the average luminous intensity.

Solid angle, $\Delta\omega_i$, can be expressed by the angle subtended in the C-plane and is calculated as follows:

$$\Delta\omega_i = \frac{2\pi}{360}[\cos\gamma_i - \cos(\gamma_i + \delta\gamma_i)]\Delta C \tag{4.3}$$

where ΔC is the distance measured in rad between the C-planes ($i.e.$ distance between C0 and C90 is 90°) and $\delta\gamma$ is the increment in elevation angle within a C-plane.

iii). Light output ratio (luminaire efficiency) (η): It is the ratio of luminous flux, Φ, emitted by the luminaire to that emitted by the filament (Φ_0) of the luminaire. It is expressed as follows:

$$\eta = \frac{\Phi}{\Phi_0} \tag{4.4}$$

4.2 Evaluation of an optical fiber as a luminaire

Ray tracing is utilized to track the displacement of rays after they exit the fiber. It is assumed that the calculations for the intersection of rays with the sphere are being executed in the far field of the optical fiber, where the interference of rays is negligible and the illumination distribution has the form of the intensity distribution. Hence, a sphere in the far field [38] with a radius bigger than at least five times the diameter of the fiber is constructed around the fiber. The $RADIANCE$ software can model customized luminaires and define the luminous intensity distribution for calculating illuminance at different points inside the room. The optical fiber is a point source that emits diffused light according to the transmission curve illustrated in Figure 4.3, calculated using ray tracing (Chapter 2). It is noted that the normalization in Figure 4.3 is with respect to the maximum light transmitted for any polar angle, Ψ.

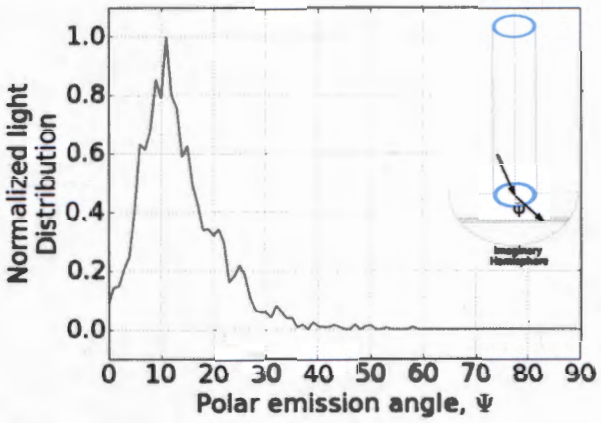

Figure 4.3: Normalized light distribution exiting from the fiber into the room.

Definition of a light source

Let us construct a large sphere (with *sphere radius* $>$ 5$\times$ *fiber dia.*) around a single optical fiber in the TC panel such that the exit end of the fiber is located at the center of the sphere. Further, let the total luminous flux output from the fiber be Φ *lm*. The sphere which encapsulates the optical fiber is divided into 180 $\delta\gamma$ angles of the (C0-C180) plane such that each section subtends an elevation angle, $\delta\gamma$, of 1° and an azimuth angle of 2π. The light output, Φ, of the fiber crosses the surface of sphere at several locations. Thus, each section is only exposed to a fraction of this light output which is conveniently expressed according to Wandachowicz [63] as:

$$\Phi = \sum_{i=0}^{179} \Delta\Phi_i = \sum_{i=0}^{179} I_{c(\Delta\omega_i)} \Delta\omega_i \tag{4.5}$$

where $I_{c(\Delta\omega_i)}$ is the average luminous intensity emitted into a solid angle, $\Delta\omega_i$ expressed in Equation (4.3) can be simplified as follows:

$$\Delta\omega_i = 2\pi(\cos i - \cos(i+1)) \tag{4.6}$$

From the specific transmission curve in Figure 4.3, a dependence between the different $\Delta\Phi_i$ can be established. The largest fraction of light rays exiting an optical fiber passes the section formed by angles $\{11°, 12°\}$. Let the corresponding light flux passing through this section be $\Delta\Phi_{11} = v_{11}\Phi$ where $v_{11} = 1$. Then, proportionally, $\Delta\Phi_0 = v_0\bar{\Phi}$, $\Delta\Phi_1 = v_1\bar{\Phi}$, and $\Delta\Phi_{i=90,91,...,179} = 0$, *i.e* the sphere mentioned above is actually a hemi-sphere for the

case of an optical fiber, since light is only radiated by the fiber tip to all γ-planes between 0° and 90°. Equation (4.5) is thus reduced to

$$\Phi = \bar{\Phi}(v_0 + v_1 + ... + 1 + ... + v_{89}) \tag{4.7}$$

$$\bar{\Phi} = \frac{\Phi}{\sum_{i=0}^{89} v_i} \tag{4.8}$$

$$\Delta\Phi_i = \frac{v_i \Phi}{\sum_{i=0}^{89} v_i} \tag{4.9}$$

and using Equation (4.6), assuming luminous intensity, $I_{c(\Delta\omega_i)}$, is uniform in each C-plane, we get

$$I_{c(\Delta\omega_i)} = \frac{\Delta\Phi_i}{\Delta\omega_i} = \frac{v_i \Phi}{\Delta\omega_i \sum_{i=0}^{89} v_i} \tag{4.10}$$

The *RADIANCE* tool *ies2rad* converts luminaire data file to the equivalent scene description. This means by using the algorithm described earlier (Figure 3.5) to calculate the light output from optical fibers along with Equation 4.10, we can treat the fiber end as a luminaire and prepare its luminous intensity distribution table. The *RADIANCE* software uses two files to define the geometry and material, and the luminous intensity distribution of the optical fibers. The code for both files is given in Appendix C, which is used for defining optical fibers as a luminaire.

4.3 Algorithm for illumination calculations

The illumination on a workplane is calculated in *RADIANCE* using the algorithm shown in Figure 4.4. The first two steps of the algorithm were described in the previous chapter. The luminous flux values collected over the year are stored in a tabulated form using the *.csv* format and loaded into *RADIANCE*. A room is prepared in the software environment with one or more walls designed using TC panels. Each optical fiber in the panel is modeled as a separate luminaire which emits light into the room following the trend given in Figure 4.3. After assigning material properties to the surfaces of the room, the illumination is estimated at different points on the workplane located at the typical 0.8 m above the floor level (*ASHRAE* 90.1-2007).

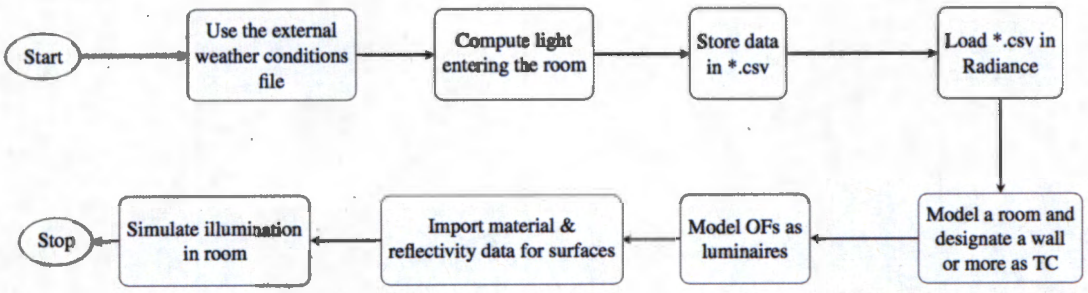

Figure 4.4: Algorithm for calculating illumination due to TC panels using *RADIANCE*.

4.4 Summary

The topics discussed in this chapter can be summarized as follows:

1. The directional distribution of a light source is measured using an equipment called the photometer.
2. For optical fibers, directional distribution is modeled to vary along the γ angles within the $C - plane$ but assumed to remain constant along the C-planes.
3. A normalized light distribution curve for a fiber is presented in Figure 4.3.
4. Illumination can be calculated in a space by modeling optical fibers as point sources and using the luminaire properties specified in Appendix C.

Chapter 5

Occupancy Models

5.1 Introduction

An occupant in a building interacts with the building controls to heat, cool or ventilate the environment to enhance thermal comfort or indoor air quality. Similarly, but to a lesser extent, the occupants adjust lighting systems to improve their visual comfort. They may also use electrical appliances causing internal heat gains and consumption of electricity. In other words, a model capable of reproducing patterns for the presence of occupants in a building and their associated behavior (Chapter 6) is of utmost importance in simulating the behavior of occupants within a building and their effects on the buildings' demands for different types of resources such as energy (*e.g.* electricity or natural gas) or water. In this chapter, a randomized model for occupancy is suggested using the Markov chain method applied to real occupancy data which is used in predicting the lighting requirements of the room.

5.2 Literature review

An occupancy model consists of daily profiles of occupants for a 24 hour period. The profiles vary between different types of buildings (residential or commercial). The simplest occupancy models, like the one in [1], use an average weekday and weekend daily profile for all the occupants in the building. This assumption fails to capture the temporal variations, such as differences in behavior between weekdays and unpredicted presence on the weekends.

Since the use of lighting is linked with the presence of users, Reinhart [59] introduced a simple improvement to the occupant presence model included in the algorithm proposed

by Newsham [47]. [59] called his model as the Lightswitch-2002. It is stochastic meaning that whenever a user is confronted with a control decision, a stochastic process is initiated to determine the outcome of the decision. The model simulated occupancy profiles corresponding to a user with working hours from Monday to Friday 8 am to 6 pm with a one hour lunch break at noon and two 15-min breaks in the morning at 10 am and the afternoon at 3 pm. All arrivals, departures and breaks are randomly scheduled in a time interval of $\pm$ 15 min around their official starting times to add realism to the model. Since the model did not consider any holidays, vacation days, sick leaves or business trips, the number of occupancy hours reported are higher than the measured occupancy hours. The mean occupancy profile derived from a total of 10 stochastic profiles for a weekday is represented in Figure 5.1

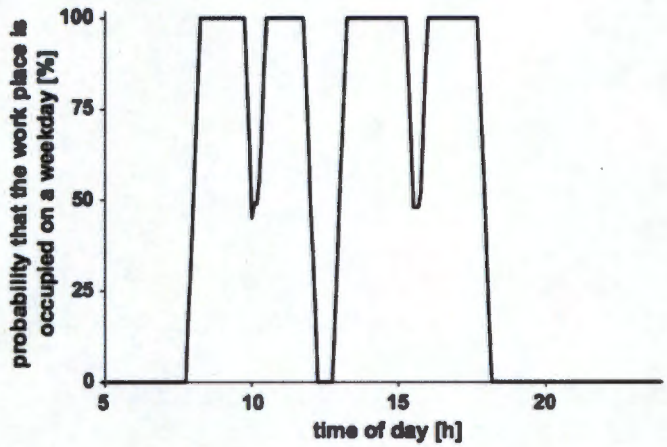

Figure 5.1: Weekday profile of the annual mean occupancy probability.

The above model by Reinhart [59] did not recognize some of the phenomena common to the real world such as the appearance of occupants on weekends, their arrival before 7:45 am, the departure after 6:15 pm and the possibility of having lunch in office space. Moreover, in a university lab, the occupants are mainly students who leave the space regularly for classes or meetings. Reinhart's model [59] failed to simulate the absence of occupants outside the breaks which made it unsuitable for the case study considered in a later chapter.

Wang et al. [64] tried to propose occupancy models that could capture the intermediate absence and presence of occupants during a random day in the office using the occupancy logs from 35 single person offices published in [28] and [60]. In this work, the researchers used a non-homogeneous Poisson process model (the rate parameter varied with time) with

different exponential distributions to simulate the occupancy-to-vacancy and vacancy-to-occupancy sequence for a single person office. From these models, it was possible to conclude that the intervals of vacancy (*i.e.* the time lengths during which the occupant is absent) were exponentially distributed. The parameter, β, in the exponential distribution ($= \frac{1}{\beta}e^{-\frac{y}{\beta}}$) varied from office to office which also changed the corresponding mean vacant interval for each office; y was the random variable representing length of vacancy interval. The research by Wang et al. [64], unfortunately, could not validate the exponential model for intervals of occupancy. In addition, the model also tried to simulate the first arrival to the office, the last departure from the office and the lunchtime break based on the assumptions that these events are distributed normally (also assumed by Reinhart [59] in his model), which were found not to be true [51]. Another drawback of this model was that like all its predecessors, it supposed that all weekdays were alike and that offices were always unoccupied during weekends.

In comparison to all its predecessors, the newly proposed Markov chain model uses a profile of probability of presence, rather than an adjusted fixed profile, as an input to a Markov chain. In this way, it is able to produce intermediate periods of presence and absence distributed exponentially with a time-dependent coefficient as well as the fluctuations of arrivals, departures and typical breaks. A complete explanation of this model is given in the next section.

5.3 Markov chain occupancy model

The occupancy model proposed by Page et al. [51] is one of the most popular models based on utilization of Markov chain Monte Carlo methods. Their model was validated and calibrated against two years of data acquired from twenty zones of an office building. The authors of the model claim that though the algorithm was tested with data from an office building, it can be applied to any type of building and any pattern of occupant presence.

Theory

The Markov chain model for occupancy uses the idea that the probability of presence at a time step only depends on the the state of presence at the previous time step. In other words the probability that an occupant is present now only depends on whether he/she was present one time step ago and not on whether he/she has been present over the past long period of time. This statement can be expressed mathematically by the following

conditional probability:

$$\begin{aligned}\mathbb{P}(X(t_n) = j_n | X(t_{n-1}) = j_{n-1}, ..., X(t_1) = j_1) &= \mathbb{P}(X(t_n) = j_n | X(t_{n-1}) = j_{n-1}) \\ &= T_{ij}(t)\end{aligned} \tag{5.1}$$

where the random variable, $X(t)$, during all finite sequences of times $t_1 < ... < t_n \in I$ has states $j_1, ..., j_n \in \{0, 1\}$. This situation corresponds to considering the state of occupancy as a Markov chain with probabilities of transition T_{ij}. The probability that an occupant should arrive at the office at 9:00 am or at 5:00 pm are not the same. Therefore, the values of T_{ij} need to be time dependent which can be captured by inhomogeneous Markov chain (with discrete states and discrete time steps). In order to determine the time dependence of these probabilities of transition, the following inputs to the model are required: the profile of probability of presence over a typical week and a parameter of mobility that gives an idea of how frequently people move in and out of their office zone. The reader is directed to Appendix D for details on Markov chain.

Formulation

The model generated a time series of zeros (absence) and ones (presence) that can render the arrival, departure from offices and also short instances of intermediate absence and presence in between. The profile that is produced is stochastically generated and does not simply reproduce the input pattern.

The Markov chain occupancy model only needs two states since the occupant can be expected to be either present or absent. Thus, the value of occupancy at the next time step should only depend on the state we are in now and the probability of transition from the present state to either the same state (0 to 0; 1 to 1) or its other state (0 to 1; 1 to 0). The transition state matrix in this case is expressed as follows:

$$\mathbb{T} = \begin{bmatrix} T_{00} & T_{01} \\ T_{10} & T_{11} \end{bmatrix} \tag{5.2}$$

where $\mathbb{T}$ is the transition matrix and $T_{00}, T_{01}, T_{10}, T_{11}$ are transition states given as random variables that take discrete values. The relations between the transition states are stated as follows:

$$T_{00} + T_{01} = 1;\ T_{10} + T_{11} = 1 \tag{5.3}$$

A better understanding of the states of a Markov chain model for occupancy is given in Figure 5.2.

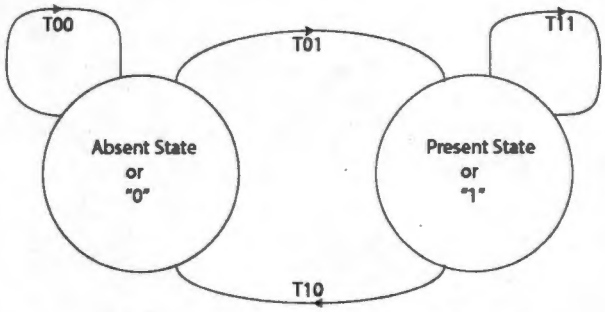

Figure 5.2: Time-inhomogeneous Markov chain model for occupancy.

From the average presence profile that is provided as an input[1], one can find the probability, $\mathbb{P}(t_n)$, of an occupant being present at a time, t_n, in a particular space.

$$\mathbb{P}(t_n) = \mathbb{P}(t_{n-1})T_{11}(t_{n-1}) + (1 - \mathbb{P}(t_{n-1}))T_{01}(t_{n-1}) \tag{5.4}$$

The terms in Equation (5.4) can be rearranged to give Equation (5.5):

$$T_{01}(t_{n-1}) = \frac{\mathbb{P}(t_n)}{(1 - \mathbb{P}(t_{n-1}))} - T_{11}(t_{n-1})\frac{\mathbb{P}(t_{n-1})}{(1 - \mathbb{P}(t_{n-1}))} \tag{5.5}$$

Another condition is needed to calculate the transition states in Equation (5.5). This is given by the mobility factor, μ, of the occupant. The mobility describes how often the user oscillate between states of presence and absence. It is defined as the ratio between the probability of change of state over that of no change.

$$\mu(t_{n-1}) = \frac{T_{01}(t_{n-1}) + T_{10}(t_{n-1})}{T_{00}(t_{n-1}) + T_{11}(t_{n-1})} \tag{5.6}$$

The parameter $\mu(t = 0)$ is the average mobility that is used at the beginning of the day and is calculated from the data. The value of μ is updated as the simulation proceeds.

From Equations (5.5) and (5.6) and the inputs $\mathbb{P}(t_n)$ and μ, a complete profile for $T_{01}(t_{n-1})$ and $T_{11}(t_{n-1})$ can be derived.

$$T_{01}(t_{n-1}) = \frac{\mu - 1}{\mu + 1}\mathbb{P}(t_{n-1}) + \mathbb{P}(t_n) \tag{5.7}$$

[1]The input presence profile can be either derived from collected data of occupants or by using standard occupancy profiles available from National Renewable Energy Laboratory (NREL [10]) or DOE-2 [17].

$$T_{11}(t_{n-1}) = \frac{\mathbb{P}(t_{n-1}) - 1}{\mathbb{P}(t_{n-1})}\left[\frac{\mu - 1}{\mu + 1}\mathbb{P}(t_{n-1}) + \mathbb{P}(t_n)\right] + \frac{\mathbb{P}(t_n)}{\mathbb{P}(t_{n-1})} \tag{5.8}$$

Equations (5.7) and (5.8) should return values in the range $\{0, 1\}$. For cases which include regular events like arrival and departure at specific times, taking lunch break in an allotted interval, etc., the value of $\mathbb{P}(t_{n-1})$ might be much smaller or greater than $\mathbb{P}(t_n)$. This could cause transition state, T_{ij}, to have values which are not admissible. In such a situation, where we have deterministic changes instead of random movements into and out of the office zone at hand, the following conditions are fixed as specified in Algorithm 1 below.

Algorithm 1 Pseudo-code for deterministic T_{ij}

```
1: procedure FOR THE CASE OF T_11
2:     if (P(t_n) == 0.0 ) then return T_11 = 0.0
3:     else if ( P(t_n) == 1.0 ) then return T_11 = 1.0
4:     else
5:         if ( P(t_{n-1}) == 1.0 ) then return T_11 = P(t_n)
6:         else if ( P(t_{n-1}) == 0.0 ) then return T_11 = 0.0

1: procedure FOR THE CASE OF T_01
2:     if (P(t_n) == 0.0 ) then return T_01 = 0.0
3:     else if ( P(t_n) == 1.0 ) then return T_01 = 1.0
4:     else
5:         if ( P(t_{n-1}) == 1.0 ) then return T_01 = 0.0
6:         else if ( P(t_{n-1}) == 0.0 ) then return T_01 = P(t_n)
```

5.4 Procedure

Figure 5.3 shows how the Markov chain works in generating an occupancy profile. We start with a '0' probability for an occupant at time $t = 0$ for a new day. At the next time step, which could be an interval of few minutes to hours depending on the sparsity of the data, a number is randomly drawn between '0' and '1' for each state (presence or absence) and compared with values of transition (*i.e.* T00, T01, T11, or T10), to select the event that occurs in the next step. For cases leading to T_{11} or T_{01}, we consider the occupant to be present (marked as '1') in the new time step. For the remaining cases, T_{00} or T_{10}, the occupant is marked as '0' or being absent. The state of presence of each occupant of one zone and the states of occupancy of different zones being considered are independent so

this algorithm can be repeated as many times as the number of total occupants, respecting, of course, the inputs particular to each occupant simulated.

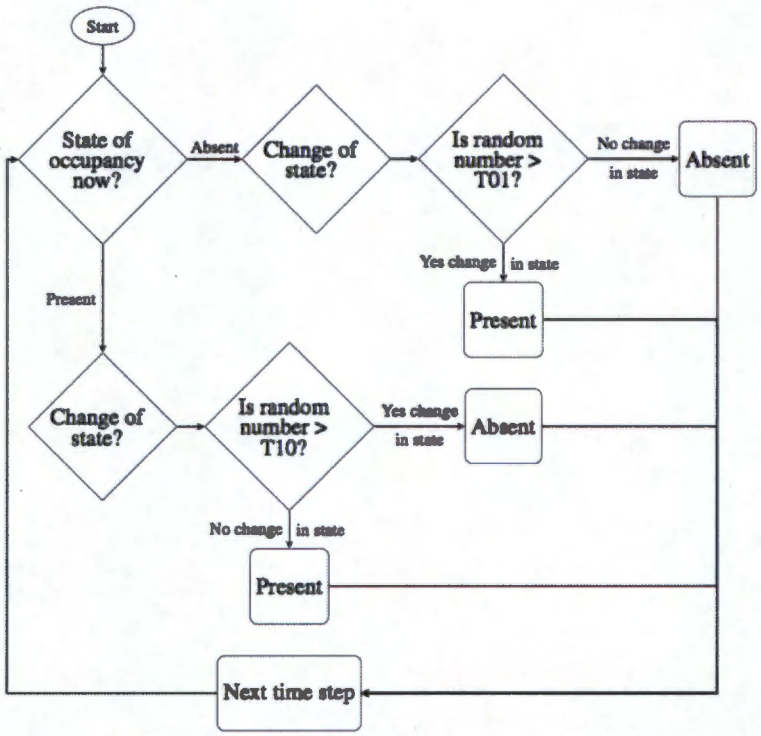

Figure 5.3: Occupancy model algorithm based on Markov chain.

5.5 Summary

Chapter-5 is summarized as follows:

1. Reproducing occupancy patterns in an energy model is highly important since many other models *e.g.* use of HVAC systems, lighting, water usage, are dependent on such occupancy models.

2. Earlier research either used simple models for occupancy or introduced very simple randomizations.

3. For this research, a more accurate method called the Markov chain occupancy model is used to estimate occupancy.

4. The Markov chain model for occupancy uses the idea that the probability of presence at a time step only depends on the state of presence at the previous time step.
5. The data for occupancy are utilized to generate two parameters: a) profile of probability of presence over a typical week and b) the mobility of the occupant.
6. The two parameters are fed into the Markov chain model to stochastically generate occupancy profiles for a non-leap year starting from any day of the week and for all occupants in an office space.

Chapter 6

Light switching models

Studies have been made in the past to analyze how people, in their natural working environments, interact with lighting controls. From these studies, a number of light switching profiles have been developed that capture the average behavior of the occupants. The estimation of artificial lighting use with reasonable accuracy is important to determine the energy balance of a prospective building early in its design, or in assessing the cost effectiveness of automatic lighting controls for an existing building. Till a few decades ago, the model for lighting use was based on one or more of a number of crude assumptions, *i.e.* lights are 'on' continuously throughout the building, there will be no lighting use during summer months, or occupants behave like photoelectric switches ensuring that light will be 'on' only when the daylight illuminance on their desks or in the ceiling is below the design level set by the building codes and standards. With the adoption of behavioral methods for tracking lighting use and several long term field studies being conducted [5], [58], [36], [21], [20] to validate the occupant's interaction with lighting controls, a number of reliable light switching models have been developed to follow the observed patterns of occupant's behavior.

In this chapter, some of the popular light switching models for manual controls are introduced. These models are used in estimating the amount of energy that can be saved from daylighting harvesting.

6.1 Lighting actions

In general, a light switching algorithm is used to measure the probability of the occurrence of any event which is related to interaction of an occupant with lighting controls. The principal reason for any modulation is that people are concerned with the visual com-

fort at their work area which might hamper their work productivity. Moreover, from a practitioner's point of view, algorithm can be combined with simulated annual daylight and occupancy profiles to predict a building's annual lighting demand at early stage of construction and also justify the use of automated controls over manual ones. There are four types of lighting events that are undertaken by an occupant in a room. These actions include:

1. Switch-on at arrival
2. Intermediate switch-on
3. Intermediate switch-off
4. Switch-off at departure

In the following sections, the first three lighting events will be discussed in detail. It is noted that switch-off at departure is considered in a simplified practical manner as discussed at the end of this section. A summary of observations based on previous field studies on manual lighting is presented in Table 6.1.

Table 6.1: Lighting behavior observed from previous field studies.

Manual control of artificial lighting	Reference
1) People usually pertain to either of the following two behavioral classes • people who switch on the lights for the duration of the working day and keep it on even in times of temporary absence • people who use electric lighting only when indoor illuminance levels due to daylight are low.	[40]
2) All lights in a room are switched on or off simultaneously.	[21]
3) Switching mainly takes place when entering or vacating a space.	[21], [40], [54], [58]
4) The switch-on probability on arrival for artificial lighting exhibits a strong correlation with minimum daylight illuminances in the work area.	[21], [40]
5) The presence of an occupancy sensor influences the behavioural patterns of some people. On the average, people in private offices with occupancy control are only half as likely to turn off their lights upon temporarily departure than people in working area without sensors	[54]

The light switching algorithms proposed here will be used to quantify the savings in energy that is aggregated over the entire year by considering daylighting transmitted by a wall constructed from TC panels. In this case, only manual lighting controls, instead of automatic/dimming controls, are used to give an absolute assessment of the electrical lighting that can be saved from using the TC panels. Further, from prior studies it was inferred that people switched-off lights when the work place was vacated in the evening but did not switch off light during short breaks, *e.g.* lunch or tea breaks. It is also suggested to turn-off lights or use natural sunlight in case the lighting intensity on the workspace from lamps is higher than that which is appropriate for a specific activity [46]. Some reasons for this behavior could be reluctance from the occupants to take action when the controls are located away from the workstations or disinclination to disturb or distract others in multi-person offices. In this model, it was assumed that the lights had occupancy sensors which switched off the lights every time the occupant left his work desk. This was again done to calculate the energy savings due to the installation of the TC panels in the room from the perspective of an *active* user (*active* user is one who takes conscious decisions to switch-on/switch-off electrical lights while considering daylighting).

6.2 Switch-on at arrival

The switch-on at arrival event corresponds to the probability that the occupant will turn on the lights when he/she enters the room. This event is considered to be the most important criterion for energy savings due to lighting and a number of studies have validated this importance. Boyce et al. [5] reported that around 79% of all switching decisions made by the users during the day were executed during the beginning of the day when people came to office. They conducted this field work in an office building situated in Albany, New York. Another study by Reinhart and Voss [58] deduced that switch-on events upon arrival accounted for 86% of all switch-on events. They monitored the activities of the users in a building in Weilheim near Stuttgart, Germany. Interestingly, both of the aforementioned studies and other studies by Love [40], Bourgeois et al. [4], concluded that the switch-on at arrival event was highly correlated with the observed minimum workplane illuminance. Hunt [21] suggested a probability function to relate the amount of desk illuminance to the likelihood of an occupant switching 'on' the light. The function has been widely used since and has also been cited in some of the studies mentioned previously in this section.

The study by Hunt [21] used time-lapse photography to collect data on lighting actions from several schools and offices for six months. From the data it was possible to fit the experimental data very closely to a mathematical expression. The fitted curve equation

proposed by Hunt [20] is as follows

$$y = a + c/(1 + \exp\{-b(x - m)\}) \tag{6.1}$$

where y = switching probability, a = -0.0175, b = -4.0835, c = 1.0361, m = 1.8223 and $x = \log_{10}$(minimum daylight illuminance in lx) subject to restrictions on y such as

$$\begin{aligned} y &= 1.0 \text{ for } x \leq 0.843 \\ y &= 0.0 \text{ for } x \geq 2.818 \end{aligned} \tag{6.2}$$

Equation (6.1) is plotted for a range of illumination received on a working plane and presented in Figure 6.1.

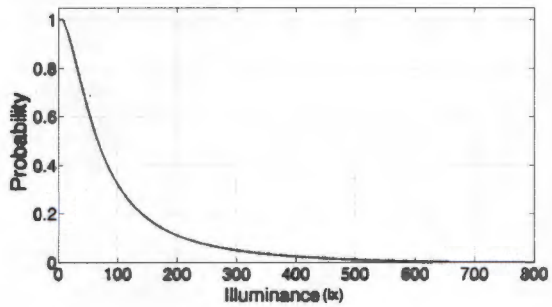

Figure 6.1: Probabilistic curve for switch-on at arrival.

6.3 Intermediate switching-on and switching-off

Intermediate light switching means the act of interacting with artificial lighting at occasions other than upon arrival to or before departure from the office. The determination of a probability function for intermediate switching events has been cumbersome for researchers in the past since the frequency of interaction of occupants with lighting controls over the day is usually low. The most recent and extensive research on this topic was undertaken by Lindel of and Morel [36] who analyzed almost two years of data (mid-November 2002 to mid-January 2005) from the LESO (Solar Energy and Building Physics Laboratory) building in EPFL, Lausanne, Switzerland.

The intermediate switching-on event was shown to be dependent on the illuminance threshold of the users. As soon as the illuminance reduced below the threshold, the switch-on probability sharply rose to a level between 1% and 4%. From field studies, this threshold

was found to be between 100 lx and 200 lx. The data for intermediate switch-on probability is presented in Figure 6.2. Since the users did not let illuminance drop to zero, none of the studies were able to conclude whether the probability should rise to unity for vanishing illuminance. Therefore, $p = 1.0$ for zero illuminance will be taken as an assumption for energy calculations.

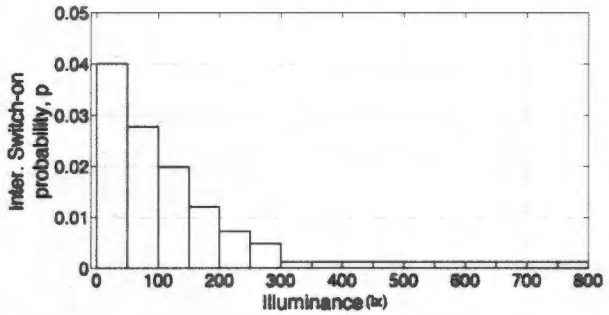

Figure 6.2: Intermediate switch-on (for illuminance=0, p=1.0 is assumed) [36].

The probability of an intermediate switching-off event is observed to be much lower than an intermediate switching-on event (Figure 6.2). This indicates that the users switched off their lights mostly on their way out of the office while keeping the lights switched on for the rest of the day. From Figure 6.3, it can be shown that the intermediate switch-off probability is rather flat at around 0.1% and is independent of the illuminance value.

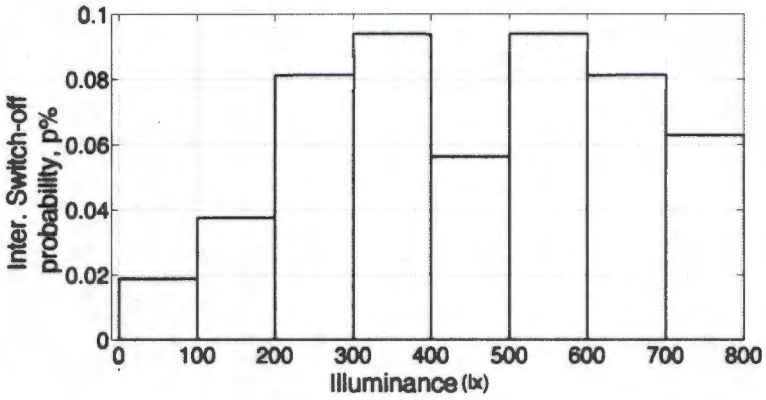

Figure 6.3: Intermediate switch-off (for illuminance=0, p=1.0 is assumed) [36].

From the studies above it became apparent that users usually interacted with the controls available to them while they were moving inside their office. Users did not leave their

seats to adjust their settings unless the situation is clearly uncomfortable.

Remark: The reluctance of users to change the light settings while they are sitting means that the controls should be placed in a location that is close and convenient to the user, who will otherwise not use them.

6.4 Summary

The topics discussed in this chapter can be summarized in the following points:

1. There are four primary light switching events: Switch-on at arrival, Intermediate Switch-on, Intermediate Switch-off and Switch-off at Departure. The first three are relevant to this research since it is assumed in the model that the lights have sensors that switch the lights off at departure.
2. The switch-on at arrival event corresponds to the probability that the occupant will turn on the lights when he/she enters the room.
3. Switch-on at arrival is considered to be the most important and commonly used criterion for energy savings due to lighting.
4. Intermediate light switching on and off means the act of interacting with artificial lighting at occasions other than upon arrival to or before departure from the office.
5. The results proposed by Lindel of and Morel [36] were used in this study to evaluate the intermediate switching on and off actions of the occupants.

Chapter 7

Heat conduction in the TC panels

The TC panel consists of concrete and plastic optical fibers that are both known to conduct heat when exposed to a temperature difference. The optical fibers, moreover, channel heat and radiate it into the room. They use the same principles for heat radiation as were used to transmit light. The total heat that enters/leaves the room increases the heating/cooling loads for the HVAC system. Hence, it is important to estimate these loads which will be required in sizing the heating and cooling equipments inside the room. In this chapter, a numerical method for conduction is described to calculate the total heat flux exchange that occurs through the TC panel subject to boundary conditions existing inside the room and in the outside environment.

7.1 Finite difference method for conduction

The heat transfer in a TC panel due to conduction of heat is given as follows:

$$\rho c_p \frac{\partial T}{\partial t} = \nabla.(\boldsymbol{\lambda} \nabla T) \tag{7.1}$$

where $\rho = \rho(\vec{r})$ is the mass density of the TC panel, $c_p = c_p(\vec{r})$ is the specific heat at constant pressure, $\boldsymbol{\lambda} = \boldsymbol{\lambda}(\vec{r}, T)$ is the heat conductivity of the TC which can be temperature, T, dependent, $\vec{r} = (x, y, z)$ gives the coordinates of any point in the TC panel, time is expressed as t.

For a 1-D system in the x-direction, Equation (7.1) is written as

$$\rho c_p \frac{\partial T}{\partial t} = \frac{\partial}{\partial x}\left[\lambda(x)\frac{\partial T}{\partial x}\right] \tag{7.2}$$

To solve Equation (7.2) numerically, an explicit finite difference for heterogeneous materials as given in [55] was proposed. The properties of heterogeneous materials (*i.e.* concrete and optical fibers) used in the construction of the TC panel can be easily accounted for in this scheme. A special mesh is generated to cover the volume of the domain. First, grid nodes are placed at the center of grid elements as shown in Figure 7.1. Then, to fulfil the transient condition for equality of temperature at the interfaces between grid elements, new intermediate grid points for $T_{i+1/2}$, $T_{i-1/2}$, ... are introduced that lies on the interface between grid elements as represented in Figure 7.1.

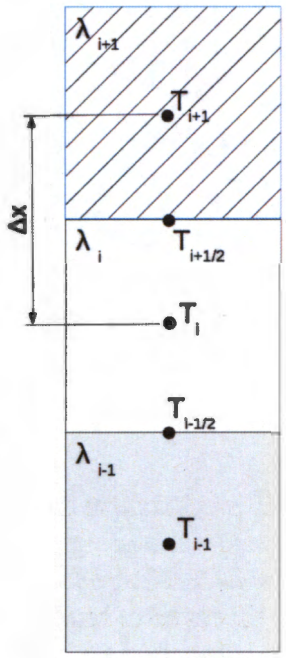

Figure 7.1: Grid elements with different material properties denoted by different patterns in the grid elements.

Within each grid element the properties are homogeneous such that the second derivative of the temperature at the center of grid element is expressed as follows:

$$\begin{aligned}\frac{\partial^2 T_i}{\partial x^2} &= \frac{\frac{T_{i+1/2}-T_i}{\frac{\Delta x}{2}} - \frac{T_i - T_{i-1/2}}{\frac{\Delta x}{2}}}{\Delta x} \\ &= \frac{2(T_{i+1/2} - 2T_i + T_{i-1/2})}{\Delta x^2}\end{aligned} \tag{7.3}$$

At the interface of two grid elements with different material properties, the following condition holds:

$$\lambda_i \frac{\partial T_i}{\partial x}\bigg|_{\Omega} = \lambda_{i+1} \frac{\partial T_{i+1}}{\partial x}\bigg|_{\Omega} \tag{7.4}$$

where Ω denotes the interface and index i gives the grid point where there is a jump in the thermal conductivity.

$$\begin{aligned} \lambda_i \frac{T_{i+1/2} - T_i}{\frac{\Delta x}{2}} &= \lambda_{i+1} \frac{T_{i+1} - T_{i+1/2}}{\frac{\Delta x}{2}} \\ T_{i+1/2} &= \frac{\lambda_i T_i + \lambda_{i+1} T_{i+1}}{\lambda_i + \lambda_{i+1}} \end{aligned} \tag{7.5}$$

Similarly $T_{i-1/2}$ can be written as:

$$T_{i-1/2} = \frac{\lambda_i T_i + \lambda_{i-1} T_{i-1}}{\lambda_i + \lambda_{i-1}} \tag{7.6}$$

For grid elements far away from the interfaces of different materials, the standard central difference scheme is applied to grid points inside the elements.

$$\frac{\partial^2 T_i}{\partial x^2} = \frac{T_{i+1} - 2T_i + T_{i-1}}{\Delta x^2} \tag{7.7}$$

The iterative solution procedure starts with calculating $T_{i+1/2}$ and $T_{i-1/2}$ from the temperatures calculated in the previous time step by Equations (7.5) and (7.6). Since $T_{i+1/2}$ of a grid element is equal to $T_{i-1/2}$ of the next element, they do not need to be calculated separately.

Thus, the new explicit finite difference scheme applied to a single grid element at time step, t_{i+1} for the solution of a 1D problem is defined as follows:

$$\rho_i c_{p_i} \frac{T_i^{n+1} - T_i^n}{\Delta t} = \lambda_i \frac{2(T_{i+1/2}^n - 2T_i^n + T_{i-1/2}^n)}{\Delta x^2} \tag{7.8}$$

where at the n^{th} time step, $T_{i+1/2}^n$ and $T_{i-1/2}^n$ are calculated using Equations (7.5) and (7.6) and $\Delta t = t_{i+1} - t_i$.

To model a TC panel, a 3D discretization of the heat equation (Equation (7.1)) is formulated. For a grid element with homogeneous thermal conductivity, $\boldsymbol{\lambda} = \lambda \mathbf{I}$, the heat equation is given as

$$\rho c_p \frac{\partial T}{\partial t} = \lambda \Big(\frac{\partial^2 T}{\partial x^2} + \frac{\partial^2 T}{\partial y^2} + \frac{\partial^2 T}{\partial z^2} \Big) + \frac{\partial \lambda}{\partial x} \cdot \frac{\partial T}{\partial x} + \frac{\partial \lambda}{\partial y} \cdot \frac{\partial T}{\partial y} + \frac{\partial \lambda}{\partial z} \cdot \frac{\partial T}{\partial z} \tag{7.9}$$

The terms in Equation (7.9) can be rearranged to give the following:

$$\rho c_p \frac{\partial T}{\partial t} = \left(\lambda \frac{\partial^2 T}{\partial x^2} + \frac{\partial \lambda}{\partial x}.\frac{\partial T}{\partial x}\right) + \left(\lambda \frac{\partial^2 T}{\partial y^2} + \frac{\partial \lambda}{\partial y}.\frac{\partial T}{\partial y}\right) + \left(\lambda \frac{\partial^2 T}{\partial z^2} + \frac{\partial \lambda}{\partial z}.\frac{\partial T}{\partial z}\right) \tag{7.10}$$

The discretized form of Equation (7.10) is analogous to Equation (7.8), where λ is constant within a grid element, *i.e.* $\frac{\partial \lambda}{\partial x} = \frac{\partial \lambda}{\partial y} = \frac{\partial \lambda}{\partial z} = 0$, which can be expressed as

$$\rho_{i,j,k} c_{p_{i,j,k}} \frac{T^{n+1}_{i,j,k} - T^{n}_{i,j,k}}{\Delta t} = 2\lambda_{i,j,k} \left(\frac{T^{n}_{i+1/2,j,k} - 2T^{n}_{i,j,k} + T^{n}_{i-1/2,j,k}}{\Delta x^2} \right.$$
$$\left. \frac{T^{n}_{i,j+1/2,k} - 2T^{n}_{i,j,k} + T^{n}_{i,j-1/2,k}}{\Delta y^2} + \frac{T^{n}_{i,j,k+1/2} - 2T^{n}_{i,j,k} + T^{n}_{i,j,k-1/2}}{\Delta z^2} \right) \tag{7.11}$$

Indices $\{i, j, k\}$ denote the spatial discretization in the $\{x, y, z\}$ directions, respectively, and $\Delta x, \Delta y, \Delta z$ are the corresponding spatial step sizes. Interface conditions between grid elements are now defined as follows:

$$T_{i\pm 1/2,j,k} = \frac{\lambda_{i,j,k} T_{i,j,k} + \lambda_{i\pm 1,j,k} T_{i\pm 1,j,k}}{\lambda_{i,j,k} + \lambda_{i\pm 1,j,k}} \tag{7.12}$$

$T_{i,j\pm 1/2,k}$ and $T_{i,j,k\pm 1/2}$ are defined similarly to Equation (7.12).

7.2 Heat conduction in a TC panel

The TC panel will be exposed to heat due to: a) temperature differences existing between the ambient environment and the indoor conditions and b) the solar radiation incident on the wall. This will lead to rise in the temperature of the TC panel during the day and also transfer some of that heat due to conduction and radiation. The scenario of thermal exchange between the TC panel, the ambient environment and indoors can be represented in Figure 7.2.

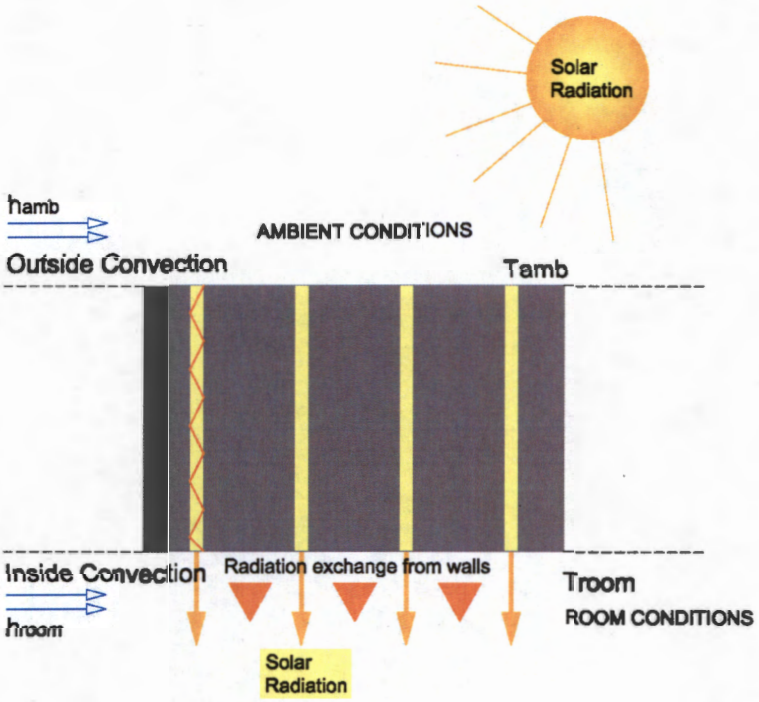

Figure 7.2: Heat exchange between TC panel, outside ambient and indoor room conditions. Illustrative image of a section of the TC panel and modes of heat transfer.

The TC panel can be divided into a number of smaller 'Representative Volume Elements (RVEs)' such that each element preserves the volumetric ratio of fibers as was modeled in the original TC panel composite. An example of a RVE in a TC panel containing 16 fibers (arranged in a 4×4 pattern) is shown in Figure 7.3.

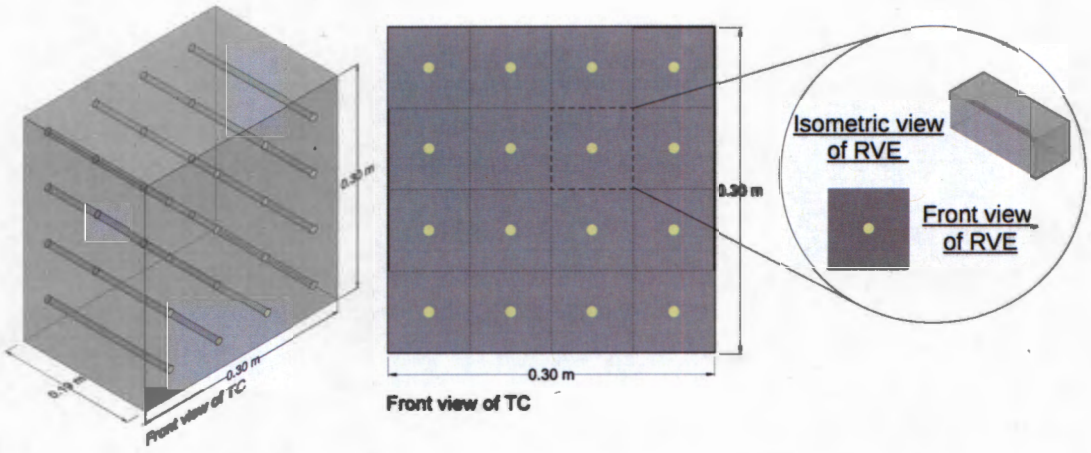

Figure 7.3: RVE of a TC panel with 4×4 fibers arranged in a regular pattern.

Boundary conditions

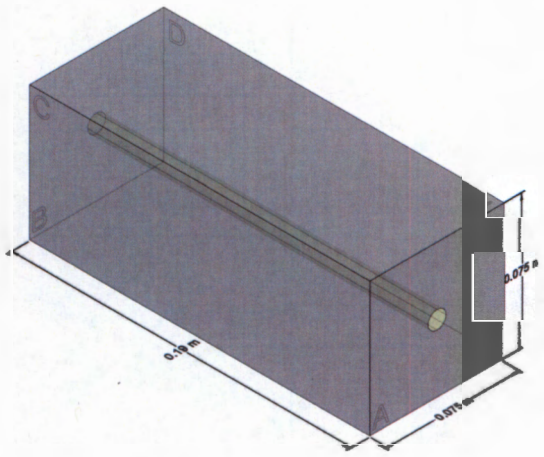

Figure 7.4: Isometric view of the RVE.

An isometric view of a RVE derived from Figure 7.3 is given in Figure 7.4. The faces are marked as A, B, C, D, E, F. The following boundary conditions are applied:

1. Faces C through F experience periodic boundary conditions which signify that the RVE is part of a larger TC panel and wall. Thus, the RVE is replicated throughout the space and is a periodic image of all the other RVEs that make up the TC panel.

2. Face A overlooks the interior of the room. It is exposed to the room air and also has radiation exchange with the rest of the surfaces inside the room. It is assumed that the RVE is surrounded by surfaces (other walls, ceiling, floor) that act like a hemispherical cap around the RVE and subtends a half angle of 90° which results in a view factor of $F_{12} = \sin^2 90° = 1$. (The view factor, F_{12} is the fraction of energy exiting an isothermal surface 1 by emission , that directly impinges and is absorbed on surface 2. View factors depend only on geometry.) The RVE exchanges radiation with room at mean radiant temperature, T_{mean}, which is calculated from the weighted average of the surface temperatures for the three walls *i.e.* those without TC panels, ceiling and roof adjacent and opposite to the considered south-facing TC wall. The heat balance across face A can be represented as follows:

$$-\lambda \left.\frac{\partial T}{\partial z}\right|_{FaceA} + h_{room}(T_{room} - T_A) + \epsilon\sigma(T_{mean}^4 - T_A^4) = 0 \qquad (7.13)$$

where $T_A = T_A(x, y)$ is the temperature of face A of the RVE, h_{room} is the convection coefficient inside the room with set-point temperature for cooling and heating given as T_{room}, $\epsilon = 0.95$ is the emissivity of all the surfaces inside the room and $\sigma = 5.6703 \times 10^{-8}\ W/(K^4 m^2)$ is the Stefan-Boltzmann constant. The discretized form of Equation (7.13) is expressed as follows:

$$\frac{-2\lambda_{i,j,k}}{\Delta z}(T_{i,j,k+1/2} - T_{i,j,k}) + h_{room}(T_{room} - T_{i,j,k+1/2}) + \epsilon\sigma(T_{mean}^4 - T_{i,j,k+1/2}^4) = 0 \qquad (7.14)$$

The terms are rearranged to give Equation (7.15) which is solved for $T_{i,j,k}$ making use of Equation (7.12) written for $T_{i,j,k+1/2}$ instead of $T_{i\pm1/2,j,k}$ using Newton's iterations.

$$\epsilon\sigma T_{i,j,k+1/2}^4 + \left(h_{room} + \frac{2\lambda_{i,j,k}}{\Delta z}\right) T_{i,j,k+1/2} + \left(-\frac{2\lambda_{i,j,k}}{\Delta z} T_{i,j,k} - h_{room} T_{room} - \epsilon\sigma T_{mean}^4\right) = 0 \qquad (7.15)$$

3. Face B interacts with the ambient environment. The concrete part of RVE absorbs solar radiation in the form of direct and diffused sunlight while the entire RVE exchanges heat with surroundings using convection. The heat exchange for face B is given as

$$\lambda \left.\frac{\partial T}{\partial z}\right|_{FaceB} + h_{amb}(T_{amb} - T_B) + q_{solar} = 0, \text{ for concrete} \qquad (7.16)$$

$$\lambda \left.\frac{\partial T}{\partial z}\right|_{FaceB} + h_{amb}(T_{amb} - T_B) = 0, \text{ for optical fibers} \qquad (7.17)$$

where $T_B = T_B(x, y)$ is the temperature of face B of the RVE, h_{amb} is the ambient convection coefficient and q_{solar} is the solar radiation incident on the concrete part of face B. Since the optical fiber guides solar radiation, the heat, q_{solar}, is not absorbed by the face of the fiber. In the discretized form, Equation(7.16) can be written as follows:

$$\frac{2\lambda_{i,j,k}}{\Delta z}(T_{i,j,k-1/2} - T_{i,j,k}) + h_{amb}(T_{i,j,k-1/2} - T_{amb}) - q_{solar} = 0 \qquad (7.18)$$

Equation (7.17) can be discretized similarly.

Rearranging the terms in the discretized forms for the concrete and fiber parts of face B gives:

$$T_{i,j,k-1/2} = \begin{cases} \frac{q_{solar} + h_{amb}T_{amb} + \frac{2\lambda_{i,j,k}}{\Delta z}T_{i,j,k}}{\frac{2\lambda_{i,j,k}}{\Delta z} + h_{amb}} & \text{for the concrete part} \\ \frac{\frac{2\lambda_{i,j,k}}{\Delta z}T_{i,j,k} + h_{amb}T_{amb}}{\frac{2\lambda_{i,j,k}}{\Delta z} + h_{amb}} & \text{for the fiber part} \end{cases} \qquad (7.19)$$

4. Some limitations exist in the current model with respect to calculating the radiative heat exchange with exterior surroundings (*e.g.* sky, ground, other buildings) and in calculating the heat absorbed by the ceiling, walls and floor of the room, which releases heat later in the day. Though the contribution of these quantities to the net heat transfer is small, their calculations would require complicated formulations which are better dealt with modeling in software like *EnergyPlus*.

7.3 Summary

The topics discussed in this chapter can be summarized as follows:

1. A new explicit finite difference method for solving the heat equation in heterogenous materials was proposed.

2. The new scheme reduced to standard finite difference method for nodes far from the interfaces between different materials.

3. A procedure to apply the finite difference scheme to Representative Volume Element (RVE) of a TC panel was detailed. Boundary conditions applied to different faces of the RVE due to heat exchange with the indoor and outdoor environment were also explained.

Chapter 8

Results and discussions

The preceding chapters detailed the techniques that were used as part of this report. This chapter applies those techniques to specific applications to estimate the lighting and heating properties of a TC panel and also estimates the energy that can be saved depending on the daylight transmitted from the TC panel and the location where the building is situated.

8.1 Case study A: Estimating the savings in lighting energy

In this example, the energy savings incurred over the day were calculated for time periods of 8 am to 6 pm local time (considering daylight savings). A lab room was modeled in $RADIANCE$ with a floor area of 3 m $\times$ 2.895 m with a ceiling height of 3.2 m. A workplane is constructed at 0.8 m above the floor level over which illumination is calculated. The South-facing wall of the lab above the workplane height is constructed with TC panels as shown in Figure 8.1. A total of 80 TC panels (panel size is 0.30 m $\times$ 0.30 m $\times$ 0.10 m) is used to span the required wall area. The surfaces in the room are white and on average reflect 60% of the total light incident on them as stated in the literature by Ouden and Steemers [50].

Remark : The room being modeled here is windowless, which is not a true representation of buildings in general. But we still see some windowless buildings like museums and superstores that are easy to design and also protect the indoor environment and artefacts from weather fluctuations and daylight.

Occupancy data

The Markov chain model was trained using the occupancy data collected for users working at a particular laboratory space, namely, CREST (Center for Research in Energy Systems Transformation) Lab, Cory Hall, Berkeley. Three occupants, including two graduate students and one staff member, were identified for whom at least three months of continuous occupancy data were available. The data were used to generate their averaged occupancy profile for each day of the week and estimate their mobility in the lab during the semester. It was observed that the students in the lab were very mobile often leaving the lab to attend classes, meetings or breaks while the staff member's work was more sedentary. As an example, the average occupancy profile (*i.e.* the probability of the presence of an individual at a certain time of the day) of a student for the entire week is shown in Table 8.1. From Table 8.1 we see the occupant arrives to the lab everyday after 9 *am*. The occupant is away from the lab between 11 *am* and 1 *pm* every Tuesday and Thursday while on Monday, Wednesday and Friday, the occupant spends most of the time in the lab. Another example in Figure 8.2 shows the occupancy profiles of all the three occupants on a Monday. Similar occupancy profiles were generated for other days of the week.

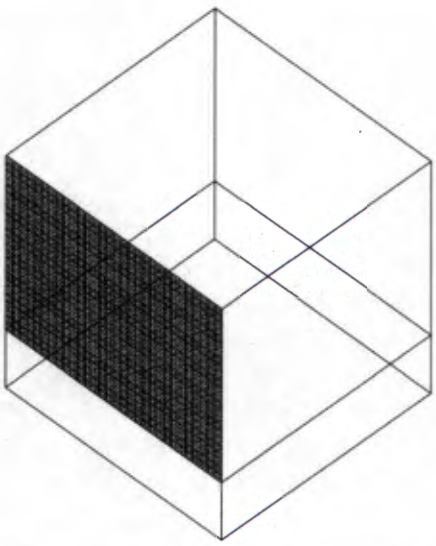

Figure 8.1: Wireframe model of lab with a South-facing vertical TC wall.

Table 8.1: Average occupancy profile for a graduate student during the week generated from more than three months of occupancy data. The average mobility, μ at $t = 0$, of the occupant is 0.215.

	8 *am*	9 *am*	10 *am*	11 *am*	12 *am*	1 *pm*	2 *pm*	3 *pm*	4 *pm*	5 *pm*	6 *pm*
Mon	0.00	0.44	0.56	0.67	0.56	0.56	0.78	0.56	0.44	0.67	0.56
Tue	0.00	0.33	0.33	0.00	0.00	0.00	0.11	0.22	0.00	0.00	0.11
Wed	0.00	0.22	0.56	0.44	0.22	0.11	0.44	0.56	0.56	0.67	0.44
Thu	0.00	0.11	0.22	0.00	0.00	0.00	0.22	0.44	0.11	0.67	0.89
Fri	0.00	0.11	0.44	0.56	0.56	0.44	0.78	1.0	1.0	0.78	0.44
Sat	0.00	0.00	0.38	0.5	0.38	0.38	0.5	0.38	0.38	0.38	0.63
Sun	0.00	0.13	0.25	0.63	0.50	0.50	0.63	0.38	0.38	0.5	0.63

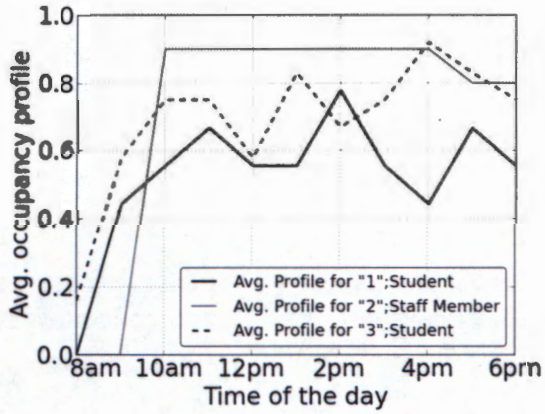

Figure 8.2: Average occupancy profiles for the three occupants on a Monday.

The occupancy data was collected using UC Berkeley's indigenous network of wireless sensors and actuators for monitoring AC energy usage. The entire architecture is called *ACme* [29]. The network detected changes in the power requirements when a user connected his or her electrical device (e.g. laptop, monitor, etc.) to the power source. This information was uploaded to a central database and could be retrieved from the server. The collected data was carefully analyzed to filter situations where the user left their device plugged in but unattended for long hours (e.g. a student running an application on their computer overnight). One way to detect this was by observing the fluctuations in hourly power demand over the interval, which in such cases, turned out to be small.

Calculation of optimal TC panel tilt angle

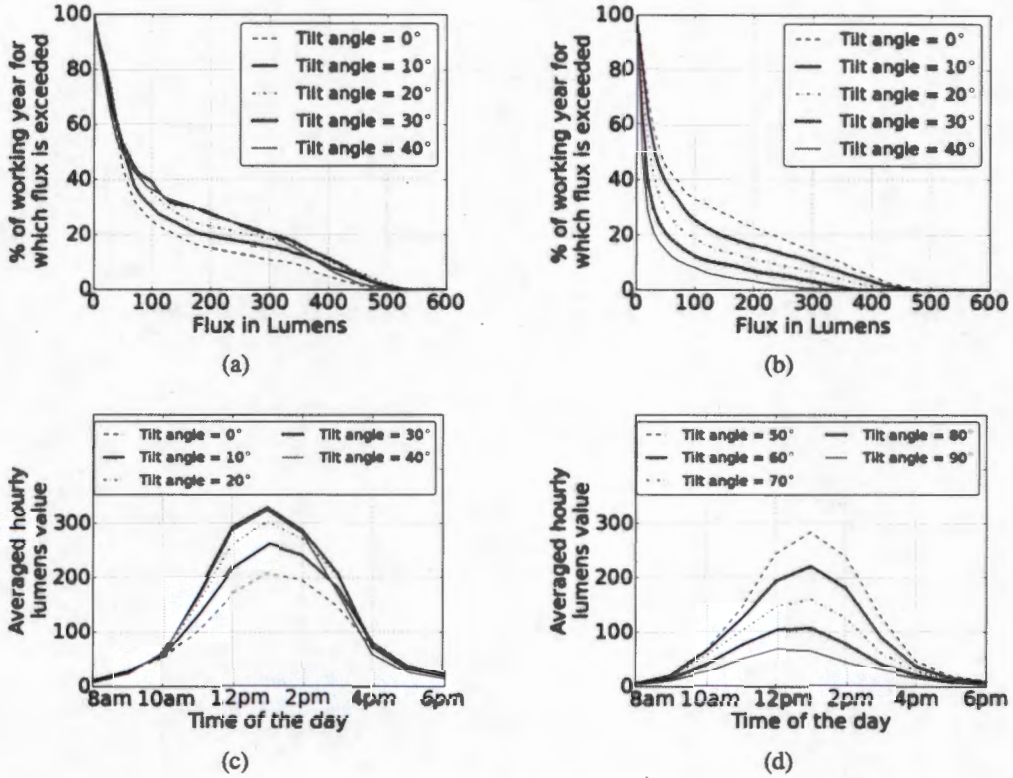

Figure 8.3: Calculations of luminous flux for a fiber vol. ratio of 10.56% based upon daytime (8 *am*-6 *pm*) (a) and (b) Luminous flux availabilities as a percentage of a non-leap year such that a flux value is exceeded. (c) and (d) Average luminous flux calculated for each hour of the whole year.

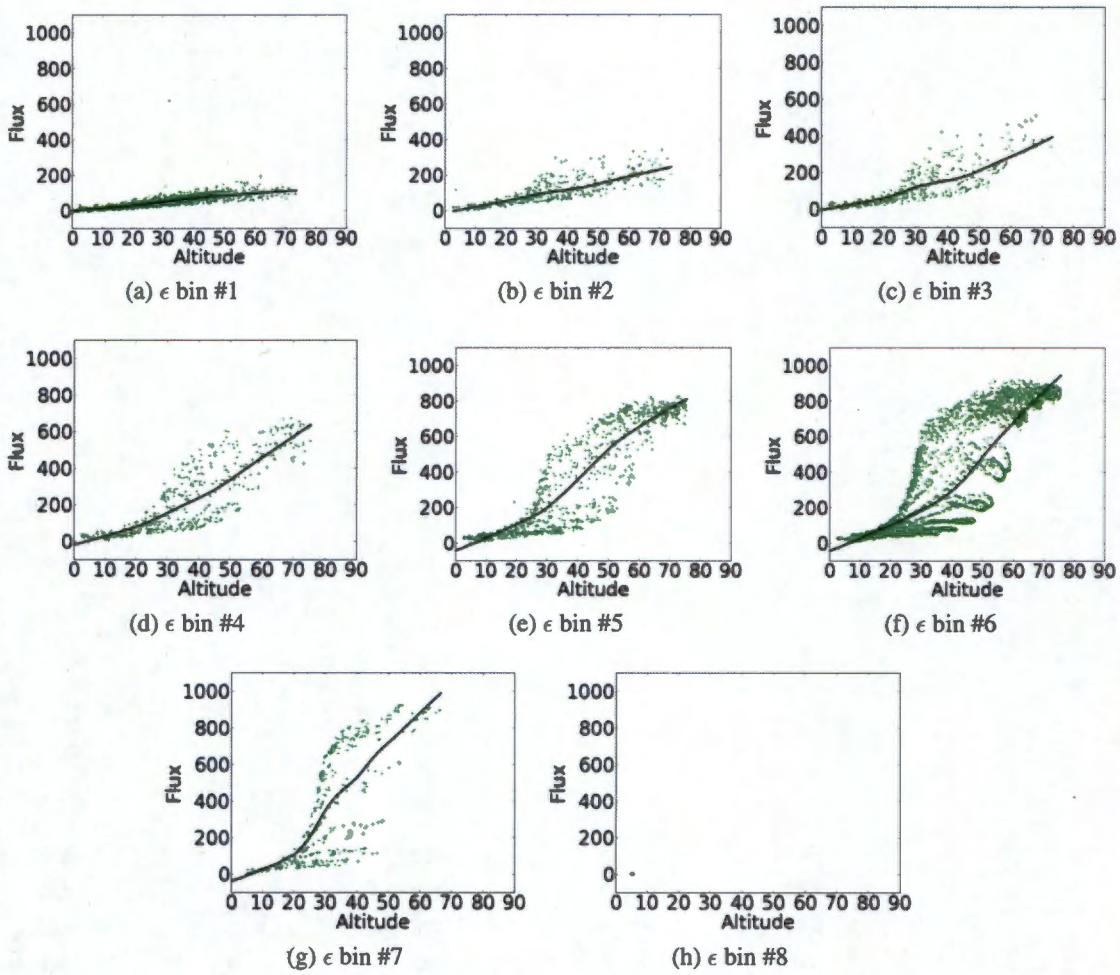

(a) ϵ bin #1 (b) ϵ bin #2 (c) ϵ bin #3

(d) ϵ bin #4 (e) ϵ bin #5 (f) ϵ bin #6

(g) ϵ bin #7 (h) ϵ bin #8

Figure 8.4: Variation of the luminous flux with solar altitude for atmospheric clearness, ϵ.

The optimal tilt angle for the TC panel is the angle which on average would transmit the maximum light for the given year. This angle would depend on the prevailing sky conditions of the location apart from the latitudinal and longitudinal values. In this research, the optimal tilt angle for a south-facing TC panel in Berkeley, CA was computed. The illuminance and irradiance values for Berkeley are adopted from the data values available in the TMY file for Oakland, CA which is located about 30 km from the site and experiences similar weather conditions as Berkeley. The TC panel has a regularly arranged grid of 121 optical fibers embedded in concrete that constitutes a fiber volumetric ratio of 10.56% in

the composite. The panel is simulated for multiple cases where it is tilted at several angles (0° to 90° in intervals of 10°) with respect to the horizontal plane. Figures (8.3a, 8.3b) and (8.3c, 8.3d) use different metrics to compare the effects of the tilt angles over the entire year . Figures 8.3a and 8.3b record the fraction of time when the flux transmitted by the TC panel exceeds a certain value. Figures 8.3c and 8.3d take the average value of the luminous flux at every half hour between 8 am and 6 pm. It was not possible to select the optimal tilt angle from visual inspection of the graphs. Instead, the areas under the curves in Figures 8.3c and 8.3d were calculated to conclude that a tilt angle, $\beta^* = 30°$, transmitted the maximum luminous flux for the year in Berkeley [3].

Remark: From the calculations, it was also observed that the areas under the curves for tilt angles between 20° and 40° were within 6% of the maximum luminous flux observed. The insensitivity for the range of tilt angles between 20° and 40° allows engineers and architects some leeway in installing the TC panels in different orientations with only minor compromise in performance related to light transmission.

The luminous flux values for the entire year for the optimal tilt angle (*i.e.* $\beta^* = 30°$ were arranged in 8 bins (Figure 8.4) according to the atmospheric clearness factor, ϵ, defined earlier (refer to Table 3.1), *i.e.* $\epsilon = 1$ to 8. It is observed that for days with overcast skies (ϵ bin 1) , luminous flux values were low and almost independent of the solar altitude. The dependence of flux on the solar altitude was stronger as the sky became clearer and less turbid (ϵ bins 3 to 7). To plot a nonlinear best fit curve through these data points, the robust LOWESS scheme was used with a spread fraction of 0.35. The details for setting up the LOWESS scheme are described in Appendix E. In general, Berkeley and the surrounding Bay Area experience very few days of highly clear skies (ϵ bin 8) which was also represented in Figure 8.4h. Hence, the splitting of the points into different bins provided us the contribution of isotropic radiation and anisotropic radiation to the diffused radiation (Equations (3.14)) while the fitting presented a trend of the solar flux through the TC panels to the altitude of the Sun in the sky (Figures 8.4a-h)

Pseudo-code and assumptions for energy savings estimator

The pseudo-code for energy savings estimator is presented in Algorithm 2. The algorithm begins with the precondition that illuminance on the workplane for each occupant is available. Using the Markov chain model, the algorithm generates a randomized annual occupancy profile. The switching models based on illuminance values and the occupancy status (i.e. Present or Absent) at the current moment decide whether the user prefers artificial lighting or sunlight. If they rely on daylight, then the event contributes to energy savings before decision is made in the next time step. The total number of such events

occurring over the year are recorded and the same process is repeated for 99 other random occupancy profiles for the same user. Total energy savings lump-sum is simply the energy offset (in kWh) during the year when the occupant did not use electric lighting. The resulting presence profile is only based on the schedule followed by the occupants during weekdays and weekends, which includes lunch breaks and flexible morning arrivals and evening departures. The switch-off probability at departure was excluded from the lighting performance model. It was assumed that the lights had occupancy sensors which switched off light automatically as soon as the occupant left the space. Moreover, each occupant was supposed to have access to a manual lighting switch (for 'on' and 'off') which controlled the illuminance on their desk.

Luminaire Rating is the power consumed by electrical lighting to illuminate the desk of an occupant. The expression for savings per occupant given in Algorithm 2 is averaged over 100 profiles (There is no rule of thumb to choose the number of profiles but after applying the algorithm to certain number of profiles, there is negligible change in the output) and converted to units of kWh by dividing it by 2 since are calculated for half-hourly intervals [2].

Algorithm 2 Energy Savings Estimator

Require: Ray Tracing using $\sim$ 100,000 rays: $Calculate\ \Phi$
Require: Workplane illuminance is calculated

```
save ← 0
for 1 to 100 do
    Generate: Annual Occupancy Profile
    for (1 to 365 days) do
        switch ← 0
        occ_{i-1} (at 8 am) ← 0
        T = 8 am
        while ( T < 6 pm) do
            illum ← WorkplaneIlluminance
            occ_i ← CurrentOccupancy
            if occ_{i-1} and occ_i is 0 then
                switch ← 0
            else if occ_i is 1 then
                if occ_{i-1} is 0 then
                    switch ← SwitchOnAtArrival
                    if switch is 0 then
                        save++
                else if occ_{i-1} is 1 and switch is 1 then
                    switch ← SwitchOnInter
                    if switch is 0 then
                        save++
                else
                    switch ← SwitchOffInter
                    if switch is 0 then
                        save++
            T += 1/2 hr (Energy savings are calculated every half-hour)
Savings per occupant is calculated as:
LuminaireRating × save/100(kW) × 1/2(hr)
```

Savings calculations

For saving calculations, two types of TC panels were considered. They either had a 121 (grid of 11 × 11) optical fibers (vol. ratio of 10.56%) or 49 (grid of 7 × 7) optical fibers (vol. ratio of 4.28%) that were arranged regularly in the concrete matrix. The ray tracing calculations returned the luminous flux (units in lm) exiting from the end of optical fibers

of a south-facing TC panel. This data, in addition to the directional distribution of light from the end of fiber (presented in Appendix C), was used to model several thousands of optical fibers as point sources of light in the room.

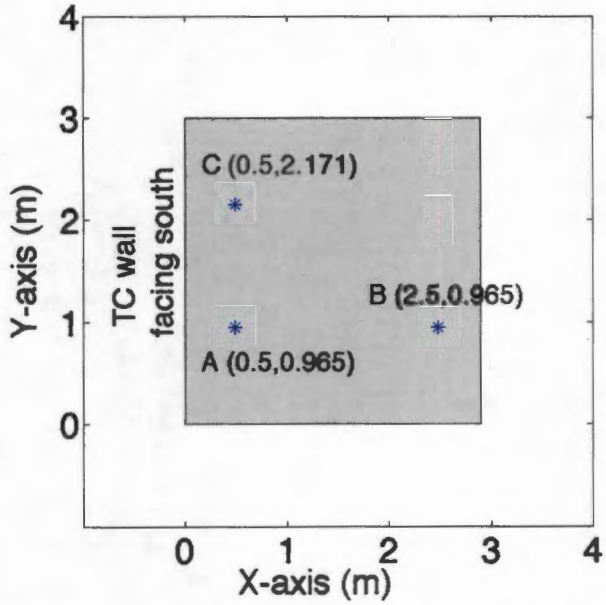

Figure 8.5: Workplane and positions A, B and C.

The illuminance was calculated at positions A, B and C referring to the desk positions of the three occupants shown in Figure 8.5. The computations were undertaken for one wall that was tilted at a 90° angle (conventional vertical wall) and another wall with a tilt of 30° (case of maximum light flux output) as given in Figure 8.6. Illuminance simulations were carried out daily for the entire year using an interval of 30 min between 8 am and 6 pm (local time).

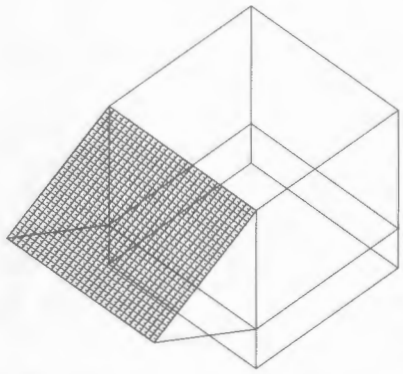

Figure 8.6: TC wall tilted at 30°.

Using the Markov chain model as described previously, several random profiles for the entire year were generated for each occupant and loaded into the code that executed Algorithm 2. The energy savings were calculated for each of the six combinations in positions that the three occupants could assume (Table 8.2). In an office, the minimum amount of light on the working plane enforced by the building code (Section 9, ASHRAE Standard 90.1.2007) is 400 lx. Three similar T8 Fluorescent tubes rated 32 W each and consuming a total of 96 W were used to produce the required illumination level. Thus, by constructing a TC wall, one could expect energy savings (kWh) for the several cases discussed in Table 8.2. Occupants are numbered from 1 to 3, where occupant 1 and 3 are graduate students and occupant 3 is a lab staff member (shown in Figure 8.2). From the results, it was observed that $Cases$ 3 and 4 were slightly better suited for the lab. This refers to the case when occupant 2 occupied position A, and occupant 1 or occupant 3 either filled up position B or C. A TC wall tilted at 30° (TC #3 and #4) performed better than a vertical TC wall (TC #1 and #2) by saving 26% more energy over the entire year. Though constructing a wall tilted at an angle of 30° for a building might be impractical, it is expected that other solutions such as optical fibers outfitted with concentrators and lenses would be able to capture sunlight at extended times of the sun path. Some of these solutions have been discussed under Future Work in Chapter 9.

The TC wall containing panels with 49 optical fibers per panel had a fiber volumetric ratio which was 60% lower than the panel containing 121 fibers. It was observed that the average savings with a vertical TC wall with 49 fibers per panel was only reduced by about 22% (corresponding to maximum savings of 43%). Also, the average savings increased nonlinearly with the number of fibers. From Figure 8.7, it could be inferred that the change in the maximum energy savings first increased and then shrunk as the number of fibers were increased in the TC panel. The error bars in the figure show the deviation

from the average that is observed due to the randomization introduced in the occupancy profiles.

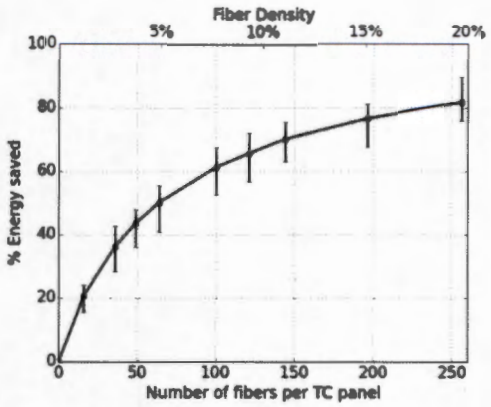

Figure 8.7: Plot showing the increase in expected energy savings with the number of fibers in the TC panel.

One of the major reasons for reduction in performance was due to the sufficient illumination provided by a TC wall with lower density of fibers. This allows the engineer to rule out construction of TC walls with higher density of fiber citing no extra savings in overall electricity consumption. The practitioner also needs to consider the effects of volumetric ratio of fibers on other properties like structural integrity of TC and resistance to water permeability before making a decision.

Table 8.2: Savings in energy for different cases. Columns 2 and 3 represent the performances of vertical TC walls containing panels with 49 and 121 fibers per panel, respectively; Columns 4 and 5 give performance results for TC walls tilted at 30° to the horizontal and containing panels with 49 and 121 fibers per panel, respectively. The last column shows the amount of lighting energy used if the room only had opaque walls.

Positional arrangement of occupants (1, 2 and 3)	TC #1 (kWh)	TC #2 (kWh)	TC #3 (kWh)	TC #4 (kWh)	Max. potential energy savings
Case 1 (A, B and C)	65	100	107	129	154
Case 2 (A, C and B)	64	97	106	129	154
Case 3 (B, A and C)	67	101	107	129	154
Case 4 (B, C and A)	67	101	107	129	154
Case 5 (C, A and B)	64	99	106	129	154
Case 6 (C, B and A)	65	100	107	129	154

The results for potential energy savings using the occupancy model derived from experimental data were compared against the savings accrued using the NREL model [10] for occupancy given in Figure 8.8. The differences are shown in Figure 8.9. It was observed that the NREL occupancy model produced energy savings which were slightly lower than the results presented in Table 8.2. This could be due to the assumption by NREL that there are very few people working during weekends, which is not entirely true for a university lab where students also work on weekends.

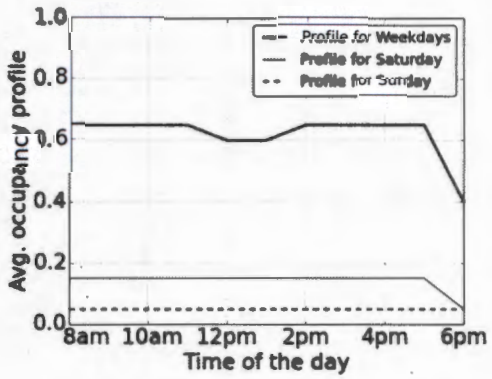

Figure 8.8: Weekly occupancy profile proposed by NREL. The y-axis gives the probabilities of presence for the occupant at a particular time of the day.

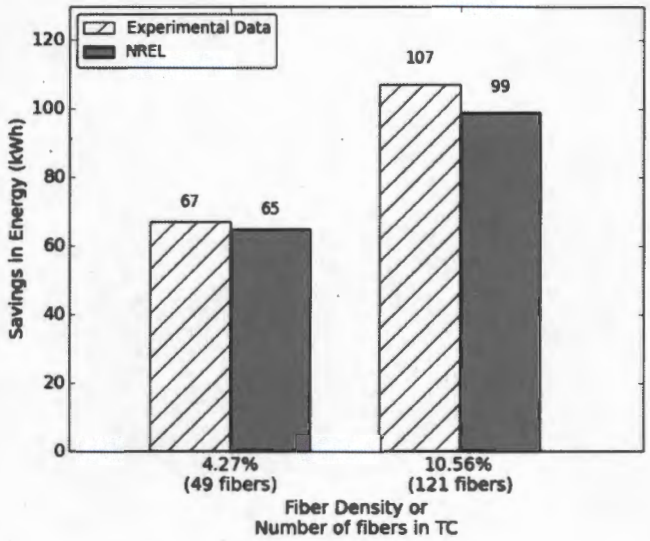

Figure 8.9: Energy savings from different occupancy profiles: Experimental data and NREL. Both the bar graphs are for a vertical wall and only the maximum values for savings have been compared.

8.2 Case study B: Coupled thermal and lighting analysis

The TC panel is exposed to heat due to the solar radiation incident on the wall and the temperature difference that exists between the outdoor environment and the indoor conditions. This leads to a rise in the temperature of the TC panel during the day and also transfers some of that heat into the room due to convection and radiation. The scenario of thermal exchange between the TC panel, the ambient environment and indoors has been represented in Figure 7.2.

The thermal analysis for the situation described in Figure 7.2 is solved using a 3D explicit finite difference method for heterogeneous materials described in Chapter 7. First, the new finite difference scheme is checked for second order accuracy in space and first order in time by comparing its solution with a known solution for a test problem. An assumed temperature distribution of $\theta(x, y, z, t) = x^2 + y^2 + z^2 + t^2$ is chosen as a boundary condition on the six faces of a simple cuboid with dimensions 7.5 cm × 7.5 cm × 20 cm. The initial condition for the nodes inside the cuboid is given by $\theta(x, y, z, 0) = x^2+y^2+z^2$. With enforced boundary and initial conditions, the heat equation is solved over the domain of the cuboid for a few seconds before the relative error between the theoretical solution

and numerical one is computed. As expected, the numerical scheme turned out to be second order accurate in space and first order accurate in time, *i.e.* $O(h^2 + t)$. This is also represented in Figure 8.10.

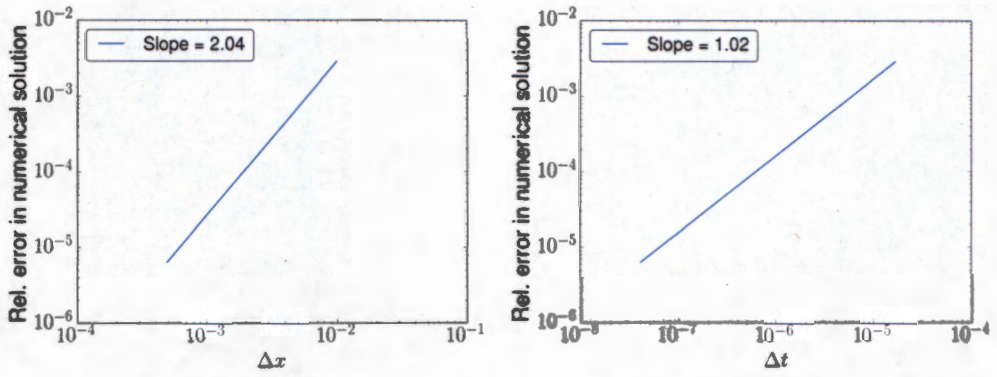

(a) Rel. Error vs Grid size

(b) Rel. Error vs Time step size

Figure 8.10: Order of accuracy for finite difference method with respect to the grid size, Δx and time step size, Δt.

After validation of the numerical scheme, the representative volume element (RVE) chosen in Figure 7.3 is used for conducting thermal and lighting analyses on a room with a south facing wall comprised of TC panels.

Heat sources in the room

A model room (shown in Figure 8.11) with a width and height of 3 m and a depth of 2.895 m is prepared for analyzing the impact of heat and light on the HVAC requirements for the room.

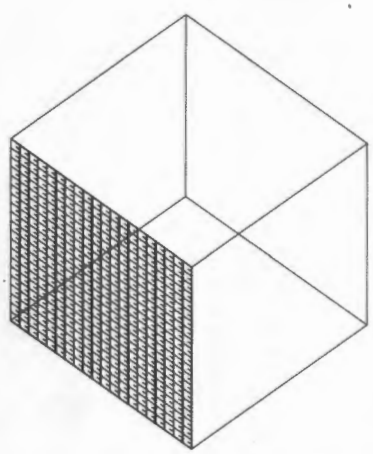

Figure 8.11: Room model for conducting coupled thermal and lighting analyses in Berkeley.

The room is maintained at $22°C$ which corresponds to the set-point temperature for heating and cooling. The south facing wall (shown with a checkered face in Figure 8.11) is composed fully of TC panels. The heat is radiated directly into the space of the room through optical fibers in the panel. Heat is also conducted into/out of the space through the walls of the room. The ceiling and floor of the room are insulated so there is no heat transfer through them. The room consists of three installations of T8 Fluorescent lamps consuming 32 W each. The lamps are designed to provide a constant illumination of 400 lux on workspaces of occupants. These lamps also dissipate 77% of their total input power as heat into the room during times of operation [56], which can further add to the cooling load of the HVAC system. Hence, it is important to control the daylight through optical fibers in TC to provide sufficient illumination inside the room while also cutting back on the heat gains.

Remark: The objective of this study is to compare the energy requirements imposed on a room that has TC panels to a completely windowless room. The set-point temperature of $22°C$ was used since it corresponded to the temperature at which the highest occupant productivity was observed by Seppanen et al. [62]. From discussion with Prof. Stefano Schiavon (Professor of Architeture, UC Berkeley), this study by Seppanen et al. [62] was limited in the scope as it did not consider well-known parameters as clothing levels and metabolic rate of occupants and the mean radiant temperature. Further, the set-points for heating and cooling are usually $4°C$-$6°C$ apart as the HVAC system is unable to continuously switch between modes of heat removal and heat addition. In future the same

algorithm will be tuned to consider different set-points for implementing whole building simulations.

Parameters for solving heat conduction through walls

Figure 8.12: The arrangement of different layers (concrete, extruded polystyrene (XPS) insulation, drywall) in the walls of the room.

The walls facing North, East and West are opaque while the wall facing South can be translucent or opaque. All the walls (including the wall with TC panels) are multi-layered and the layers are arranged as given in Figure 8.12. The heat from the walls is exchanged inside the room using convection and radiation. The interior space considered here is small but the algorithm is modular to incorporate floor areas of any sizes. The geometrical dimensions and material properties for the layers in the walls and the heat transfer coefficients used in the simulations are listed in Table 8.3.

Table 8.3: Material properties and heat transfer coefficients for conduction.

Parameter	Value/Expression
External Walls	Concrete (0.1 m), XPS insulation (0.075 m), Drywall (0.0156 m)
Concrete mix composition	Water, Cement (0.5 water-cement ratio), Fly-ash, Fine aggregate
R-value of layered-wall	2.81 m^2K/W (or 15.95 $hr - ft^2 - ^\circ F/Btu$)
R-value of fibers	1 m^2K/W (or 5.68 $hr - ft^2 - ^\circ F/Btu$)
$\lambda_{concrete}$	1.36 W/mK (From experiments at SERIS, Singapore [19])
λ_{XPS}	0.028 W/mK
$\lambda_{drywall}$	0.276 W/mK [42]
λ_{fiber}	0.2 W/mK
$\rho_{concrete}$	2180.79 kg/m^3 (From experiments at SERIS, Singapore [19])
ρ_{XPS}	25 kg/m^3
$\rho_{drywall}$	752 kg/m^3 [42]
ρ_{fiber}	1180 kg/m^3
$c_{p,concrete}$	750 J/kgK
$c_{p,XPS}$	1500 J/kgK (http://goo.gl/IDKahl)
$c_{p,drywall}$	1017 J/kgK [42]
$c_{p,fiber}$	1450 J/kgK
h_{amb}	5.7 + 3.8v_s W/m^2K (v_s is outside wind speed, [43])
h_{room}	8.29 W/m^2K (Recommended by ASHRAE)
Emissivity, ϵ	0.95
HVAC schedule	8 am to 6 pm daily

Total energy consumption from thermal and lighting analyses

Thermal and lighting simulations are conducted for the room shown in Figure 8.11. The finite difference scheme presented in Chapter 7 is used to solve for heat conduction under appropriate boundary conditions. The heat conduction in opaque walls is calculated using a 1D model since the material properties are considered to be homogeneous in the plane of the wall, while for a TC panel, a 3D model of its RVE is used (Figure 7.4). The occupancy models are used in conjunction with light switching models to estimate the heat dissipated inside the room during the year due to the use of artificial lighting. During the daytime, so-

lar radiation channeled by optical fibers will constantly heat up the space which is removed by the HVAC system to maintain the previously specified constant comfort temperature of $22°C$.

The simulation case shown here consists of a room with a south-facing TC wall made of panels with fiber volumetric ratio of 1.4%. The heat dissipated inside the room from the use of artificial lighting and transmission of solar radiation for each day of the entire year is shown in Figure 8.13. In the figure, it is observed that for days when solar radiation into the room is low (due to presence of cloudy skies), more artificial illumination is necessitated which becomes the major reason for heat dissipation. On the contrary, the ratio of heat dissipated on weekends would be primarily attributed to the solar radiation into the room due to lower occupancy levels which requires lesser use of artificial lighting.

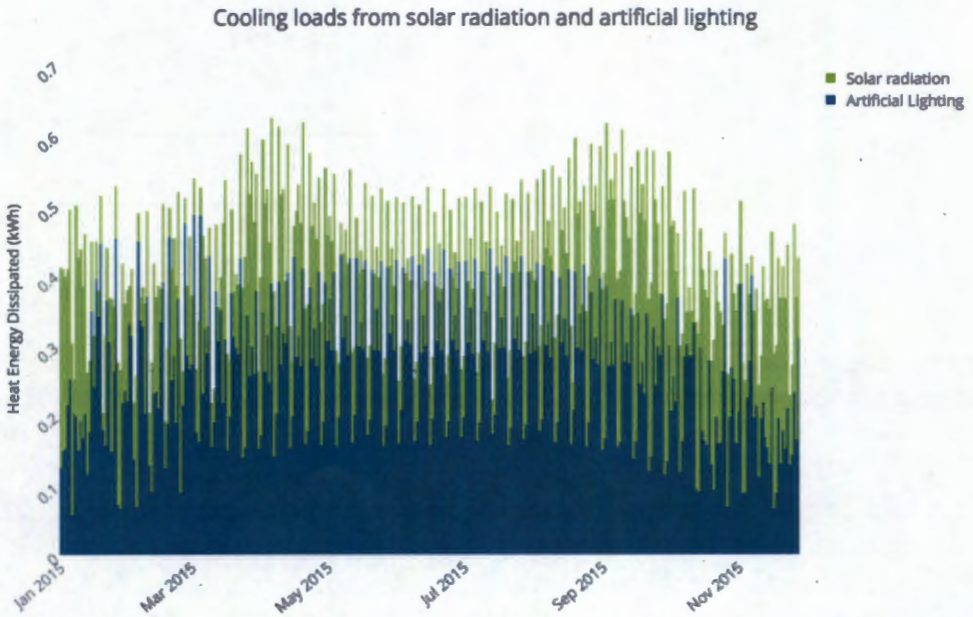

Figure 8.13: Daily cooling load for a room with fiber volumetric ratio of 1.4% in the TC panels. The heat input is due to solar radiation that is transmitted through the optical fibers and the heat dissipated by artificial lighting.

The cumulative heat dissipated due to electric lighting decreases as the volumetric ratio of optical fibers in the TC panels increases. This trend is observed in Figure 8.14 where the utilization of fluorescent lamps reduces due to sufficient illumination present during longer times of the day. The rate of reduction in heat dissipation becomes more gradual

as the number of fibers in the TC panels increases beyond 100 ($\sim$ 7.56% volumetric fiber density). This shows that the energy dissipated by lighting installations can never reach zero owing to random light-switching behavior of occupants.

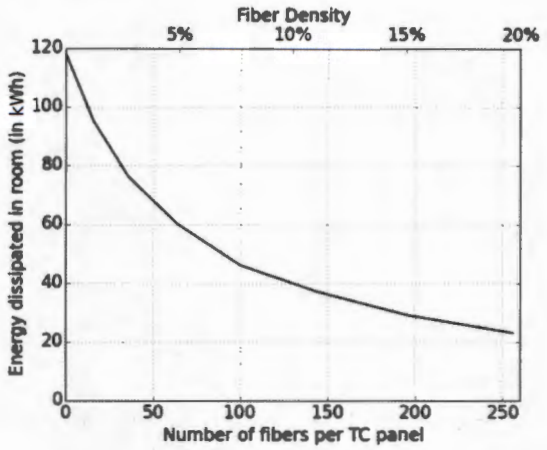

Figure 8.14: Heat dissipated inside the room by fluorescent lamps for different volumetric ratios of optical fibers in the used TC panels.

Finally, the contribution of heat conduction through the walls is also considered which gives the total load on the HVAC system when combined with the loads due to solar radiation and heat dissipation due to artificial lighting. The initial temperature of the walls before the start of simulation ($i.e.$ at 8 am) is set to the outside temperature for the previous hour ($i.e.$ at 7 am). The parameters used in boundary conditions ($e.g.$ wind speed (v_s), T_{amb}, q_{solar}, $etc.$) are first set at the start of the simulation and are then updated after every thirty minutes (by referring to the weather file for that time of the day) [2]. The simulations are repeated for all the days in the year to give the cumulative amount of heating and cooling loads on the HVAC system. Figure 8.15 shows the distribution of net daily heating or cooling loads experienced by the room. Figure 8.16 gives the relative variations in cumulative heating and cooling loads, for a room with a south-facing wall made up of TC panels with different optical fiber densities, when compared with a room with an opaque south-facing wall.

[2]The half-hourly values are calculated from the weather file by taking the mean values of the paramters for the current hour and the next hour.

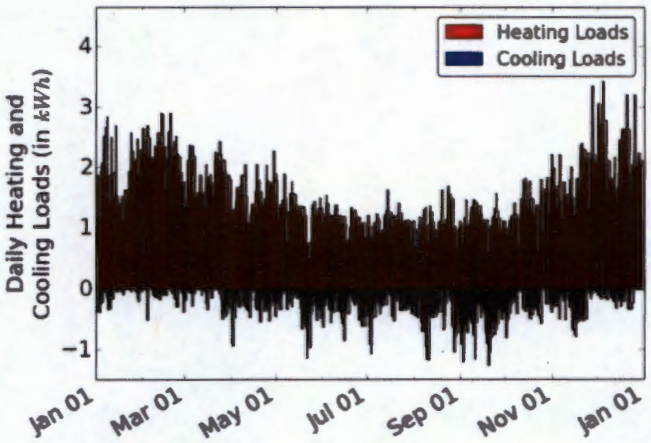

Figure 8.15: The net daily heating and cooling loads experienced by the HVAC system due to conduction, heat dissipation by fluorescent tubes and solar radiation from optical fibers.

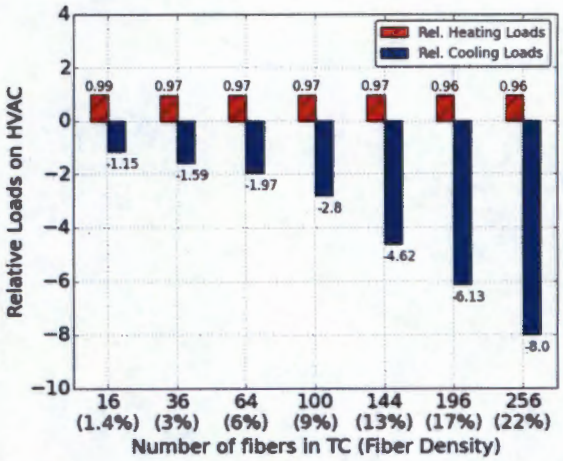

Figure 8.16: The cumulative heating and cooling loads experienced by HVAC system in a room with a south-facing wall composed of TC panels compared to a south-facing opaque wall.

Surprisingly, it is the observed from Figure 8.16 that the heating loads are almost unchanged as the fiber density ratio in TC panels is increased. This can be attributed to three reasons: 1) The initial temperature of the walls at the start of the day is set to an ambient

temperature at 7 am. Therefore, the majority of heating for the day is provided during the first half-hour (8 am - 8:30 am) (Figure 8.17), 2) During the morning times the solar radiation transmitted through the optical fibers is low which is not sufficient to equalize the heat loss through walls, 3) The R-value of an optical fiber is about 2.81 times lower than the remaining wall structure. As the fiber volumetric ratio is increased, the heat in the room is further removed by conduction through the optical fibers. Thus, a slight reduction in the percentage of heat removed due to conduction at start of day for the entire year to the total heat conducted away is observed (Figure 8.17). On the contrary, higher optical fiber density also causes overheating of room, especially during winter afternoons when the Sun's altitude is low and almost normal to the wall, which imposes greater cooling loads and unfortunately, requires operating an air conditioning system even during winter months. This trend is shown in Figure 8.18 for a room containing TC panels embedded with 256 fibers corresponding to 22.3% fiber volumetric ratio. The contributions of heat flow into the room separately due to conduction, solar radiation and heat dissipation from luminaires are given in Figure 8.19.

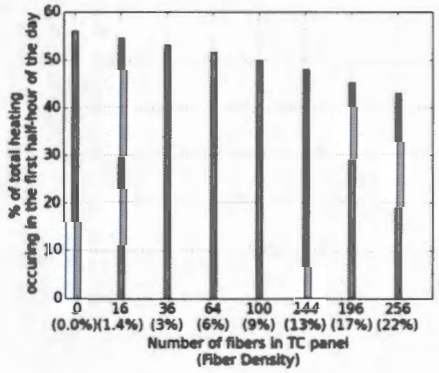

Figure 8.17: The percentage of heat removed at the start of the day for the whole year to the total heat conducted away.

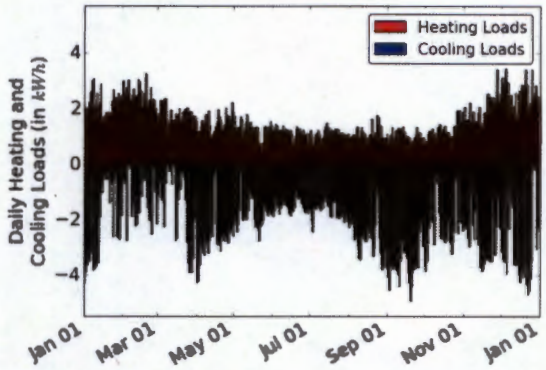

Figure 8.18: The daily heating and cooling loads experienced by the HVAC system in a room with TC panels containing 256 fibers each.

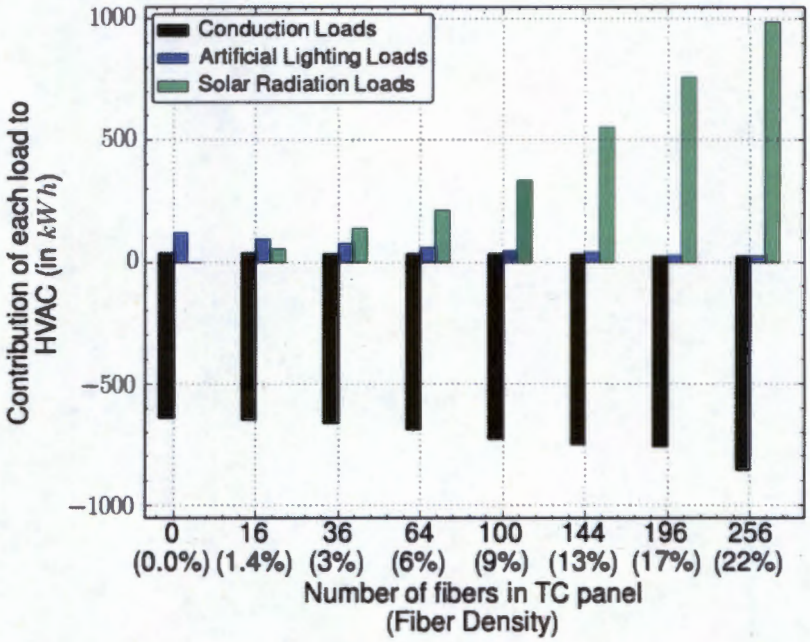

Figure 8.19: The contribution of each of the heating and cooling loads (expressed in kWh) to the total HVAC load.

The energy that is spent by the HVAC to maintain a temperature of $22°C$ inside the room can be monetized to give an estimate of the changes in expenditure on utilities due to the

introduction of wall composed of TC panels. As an example case, consider an HVAC system with a high efficiency gas furnace with 95% efficiency and an air conditioner with a Coefficient of Performance (COP) of 4.0. Also, in the San Francisco Bay Area on average, building owners pay 23.3 $¢/kWh$ for electricity and 5.4 $¢/kWh$ towards natural gas [3]. The expenditure on utilities for a room such as that shown in Figure 8.11 with a south-facing wall composed of TC panels is normalized against the energy expenditure for a room having only opaque walls. The results from comparisons are shown in Figure 8.20 which signifies the initial reduction of expenditure on energy which subsequently increases as the volumetric ratio of fibers increases. Thus, for a given COP of HVAC system and price per unit of electricity and natural gas, we can estimate the density of fibers in the TC panel to be 5.59% (64 fibers per panel) that will optimize the energy expenditure of a building. The use of lower fiber density also supports the construction procedure of TC panels (Appendix F). Optical fibers constitute the most expensive component in the entire mix in terms of material costs. Moreover, construction costs are a function of the number of fibers that have to be laid parallel to each other in the formwork. The use of low fiber density also generates less stress concentration regions in concrete that might eventually lead to the fracture of the TC panel. As a result, a fiber density of 5.59% would be reasonable in containing the costs of the TC panel while functioning as an innovative energy saving building material for the façade.

[3]Source: U.S. Bureau of Labor Statistics,
http : //www.bls.gov/regions/west/news − release/averageenergyprices_sanfrancisco.htm

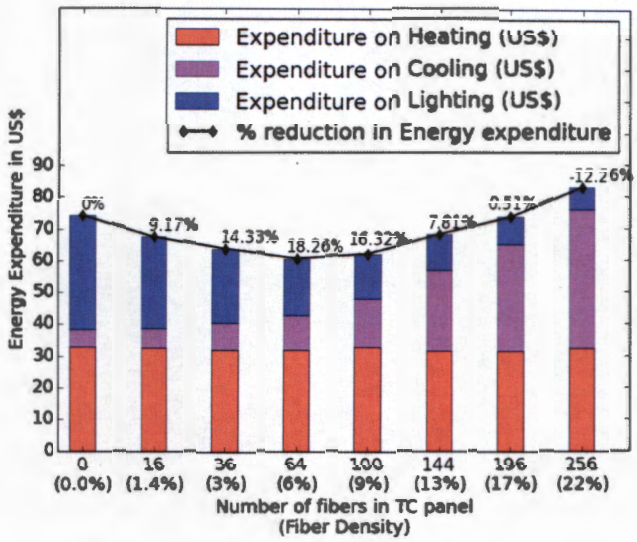

Figure 8.20: Total expenditure on cooling, heating and lighting the room space; Estimated savings in energy due to replacement of a south-facing opaque wall with a wall made of TC panels.

A new building material called the Ultra-Lightweight Cement Composites (ULCC) is being developed currently in the Civil and Environmental Engineering Department at UC Berkeley. The material achieves its low weight from the inclusion of cenospheres that are typically hollow inert spheres produced as a byproduct of coal combustion. At the same time, the high structural strength needed to support the loads in a building is also maintained. For a complete overview of the different types of ULCC mixtures, the reader is referred to research published in Wu et al. [66]. In this example, we select the material properties (Table 8.4) for one type of ULCC mix referred to as 'ULCC-1' in the above cited paper. With the inclusion of cenospheres, the thermal conductivity, λ_{ULCC} and the density, ρ_{ULCC} of the ULCC is lowered while the value of the specific heat, c_{ULCC} is slightly increased. The cenospheres provide a large interface area that increases slippage and act as a barrier to heat transfer which reduces the thermal conductivity of the mixture. In a TC panel, the concrete layer is replaced by a layer of ULCC and a new set of simulations for conduction calculations are implemented. The results in Figure 8.21 show the expenditure on heating and cooling and the relative reduction in expenses after addition of cenospheres to the mix. Interestingly, the expenses for heating do not change since most of the heating is required during morning when the entire wall is below the comfort temperature of $22°C$. The redesigning of walls with ULCC prevents the loss of heat to the ambient environment but is rather ineffective during the morning as heat is lost from the

Table 8.4: Material properties for ULCC and new wall composition.

Parameter	Value/Expression
External Walls	ULCC (0.1 m), XPS insulation (0.075 m), Drywall (0.0156 m)
ULCC composition	Water, Binder (0.35 water-binder ratio), Cenospheres, Superplasticizer, Shrinkage Reducing Admixture
R-value of layered-wall	2.99 m^2K/W (or 16.98 $hr - ft^2 - ^\circ F/Btu$)
λ_{ULCC}	0.40 W/mK [7]
ρ_{ULCC}	1303 kg/m^3 [66]
$c_{p,ULCC}$	788 J/kgK [66]

steep temperature gradient existing between the drywall, XPS and ULCC, and the indoor air. The expenses for cooling, on the other hand, are reduced by about 6-20 % depending on the density of optical fibers in ULCC. As a result, for the given COP values of HVAC and price per unit of electricity and natural gas, a fiber density in the TC panel of 5.59% (64 fibers per panel) in ULCC panels can save approximately 20.5% of energy expenses compared to a room with opaque walls constructed from normal weight concrete.
Remark : From the plots presented in Figures 8.20 and 8.21, it is seen that the savings in energy expenditure fluctuates greatly as the COP of the HVAC equipment changes. Thus, it is important that for a place like Berkeley, only high efficiency air conditioners and gas furnaces should be used to maximize the reduction in expenditure over time.

8.3 Summary

The two case studies presented in this chapter can be summarized as follows:

1. In this chapter, the concepts that are described in earlier chapters are applied to two separate case studies.

2. In the first case study, ray tracing is used to deduce that a tilt angle of 30° with the horizontal will be optimal in transmitting the maximum amount of sunlight through the TC panel for given weather conditions in Berkeley.

3. The illumination model calculates the sunlight distribution after it is transmitted by fibers inside the room using $RADIANCE$.

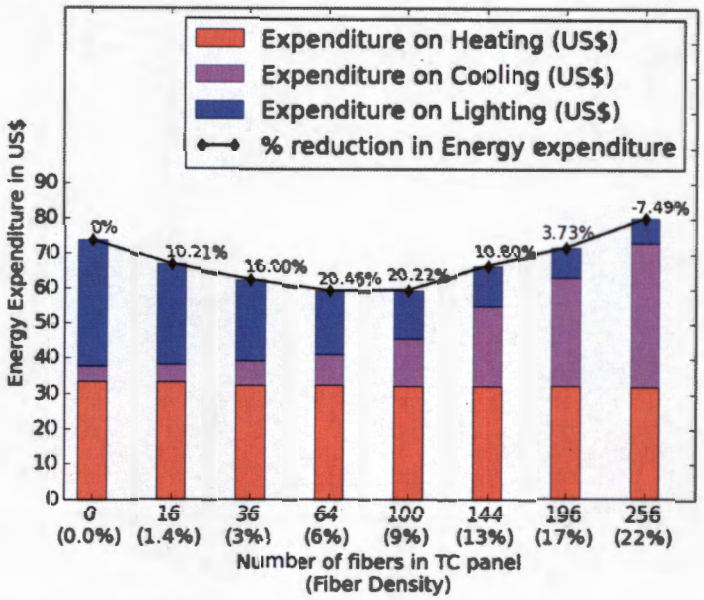

Figure 8.21: Total expenditure on cooling, heating and lighting the room space; Estimated savings in energy after redesigning the TC panels and walls with ULCC and comparing the results with a room containing opaque walls constructed from Normal Weight Concrete (NWC).

4. The 'Energy Savings Estimation' algorithm predicts the amount of energy that can be saved by relying on sunlight for lighting needs during the day.

5. It is estimated that we can save a maximum of $(67/154 \times 100 = 43\%)$ on lighting energy by constructing a south-facing vertical wall containing TC panels with a fiber density of 4.27%.

6. In the second case study, a thermal analysis is conducted on a room to calculate the annual heating and cooling loads on an HVAC system due to solar radiation, conduction through walls and heat dissipation from electrical lighting.

7. The thermal analysis is coupled with light savings from sunlight to determine the equivalent charges for utilities that a building owner would have to pay annually.

8. A building owner can save up to 18% on utility charges by using a south-facing vertical wall with TC panels and a fiber density of 5.59% (when compared to a south-facing opaque wall). The building owner can further increase the savings to

almost 30% by using building material substitutes such as ULCC which has a low thermal conductivity value.

Chapter 9

Summary, conclusions and future work

The research on a novel building construction material called Translucent Concrete (TC) has been presented in this study. The present-day softwares for analyzing building physics (*e.g. EnergyPlus, eQuest*) are limited to materials that are either opaque (*e.g* walls or partitions) or transparent (*e.g.* windows). Hence, it became necessary as part of this research to develop a software that could model and simulate a translucent system which inculcated the hybrid features of both opaque regions and transparent light-channeling components. In a TC panel, the concrete is embedded with several plastic optical fibers that guide light through their structure using laws of optics (Figure 2.4). Since the size of fibers is many orders bigger than the dominant wavelengths of sunlight, the interferences between light waves can be neglected and the transmission properties of the optical fibers can be geometrically assessed using 'Ray Tracing'. The equation for ray tracing (or the Eikonal Equation (2.1)) is discretized in space which allows a ray to keep marching in a medium based on its current position and velocity in the medium. Once the ray encounters a surface of separation between media, a part of its energy is reflected into the same medium while the remaining fraction of energy is refracted into the new medium. The percentage of light energy distributed between refracted/reflected rays is dictated by the Fresnel's Laws (Equation (2.39)) which follow the wave theory of light. In an optical fiber, the Fresnel's laws are applied at its entrance and exit apertures. The sunlight, in form of rays, enters from air into the transparent core of an optical fiber which is manufactured from PolyMethylene MethAcrylate (PMMA). The light is guided through the fiber using the law of 'Total Internal Reflection' (Section 2.5). A small proportion of this light is absorbed inside the fiber which is released as heat and can contribute to the cooling loads of the air conditioning system.

The ray tracing algorithm can provide the fraction of light/heat that is transmitted/absorbed by the TC panel. The amount of light/heat associated with these rays is dictated by the

Solar Radiation Models. One of the best performing radiation model, called the 'Perez Sky Model' (Section 3.4), uses the weather file (also called Typical Meteorological Year (TMY) file) to estimate the contributions of direct and diffused radiation components to the sunlight which depend on the cloud cover being experienced by the location at a particular time of the day. The direct radiation, as the name suggests, originates directly from the Sun and is the dominant component under a clear sky. In contrast, the diffused component is more observable during cloudy days and is produced from the direct radiation that is scattered by the small molecules that make up the atmosphere. The Perez Sky equation was modified (Equation (3.14)) to include the behavior of optical fibers which limits the amount of direct and diffused radiations that can travel through it. Once the amount of direct and diffused light exiting the TC panel is known, illumination studies can be conducted to quantify the distribution of light in a space like a private room or a lab. This was accomplished by developing new material and photometric files for optical fibers (Appendices C and F) within *RADIANCE* which are not available within the software. The illumination calculations in a room were demonstrated for a small lab space occupied by three people. The south-facing wall of the lab was covered with TC panels and exit apertures of optical fibers acted as luminaires to provide light into the room.

The utilization of natural daylighting by the occupants to carry out their daily work in the room is linked to their presence at a certain time of the day and the amount of sunlight that is available on their work space. The occupant's presence was estimated using heterogeneous Markov chain model applied to three months of occupancy data collected from occupants working in Cory Hall, UC Berkeley. The data gave an insight into the average occupancy profile of each occupant and their mobility throughout the day. Using this information, a stochastic presence profile of occupant was generated for each day of the entire year. Active occupants in a room would be willing to turn off artificial lighting if the room receives enough daylight. Probability curves were suggested that captured the human actions towards light-switching events in case the daylight illumination levels on their workspace were sufficient for productive working conditions. Thus, there is an opportunity to save energy which was computed by first determining if the occupant was present or not during that time of the day and in case the person was present, whether he/she would decide to turn off the light citing sufficient illumination on their work space. The same process was repeated for all the days in the year and the cumulative energy saved from the TC panels was recorded. From the first case study (Case study A), it was observed that a TC panel with 4.27% fiber density could save up to 43% energy spent on lighting during the year. The change in energy savings with fiber volumetric ratio was high initially but became more gradual as the volumetric fiber ratio exceeded 7.5%.

A second case study (Case study B) was also undertaken to estimate the heating and cool-

ing loads experienced by the HVAC system of the room due to the solar radiation input from the optical fibers, the conduction through the walls and the heat dissipated from artificial lighting. The solar radiation calculations followed from geometrical ray tracing, the heat dissipated by the use of fluorescent tubes employed lighting schedules derived from occupancy profiles and heat conduction was computed using finite difference methods applied to walls with boundary conditions derived from the TMY weather file. It was observed that solar radiation through optical fibers imposed large cooling loads on the HVAC system for large fiber volumetric ratios in the TC panels. Further, higher fiber ratios also provided sufficient daylight illumination for greater part of the year which helped in curtailing heat dissipated by lighting installations and in general, saved lighting energy (as shown in Case study A). The conduction through the layered wall removed a significant amount of heat during the morning which necessitated the usage of heating during those times. From calculations, it became clear that a fiber volumetric ratio of around 6% in a south-facing TC wall was best suited to reduce the overall energy usage by about 18% compared to a completely sunlight deprived room. The walls of the room were also found to increase the cooling loads of the room during the afternoon and evening times. The use of materials that have lower conductivity values like the ULCC, instead of normal weight concrete, improved the total R-value of the walls and saved another approximately 2% energy utilization over the duration of the entire year.

Though the preliminary computational results seemed promising, yet the future of TC as a building material would largely depend on finding ways in improving its light transmitting capabilities and reducing the heat exchanges between the inside and the outside environment. Moreover, as development progresses there will be a push to follow sustainable design for construction of the TC panels in order to minimize life cycle costs, operational energy and impact on the environment. The following three sections of this chapter presents discussions on some technologies that can potentially improve the performance of the TC panels. The final section of this chapter elaborates on a method that can be incorporated to evaluate long term solutions for the TC panels and search for design alternatives.

9.1 Limitations of current study

The limitations of the conducted study are identified as follows:

1. The structural integrity of the TC panel is not computed. As part of simulations, only the lighting and thermal responses of the TC panels to changing ambient conditions have been analyzed. It is obvious that increasing the volumetric ratio of optical fibers

in concrete will lead to regions of stress concentrations which will consequently affect the strength, constructibility and the overall structural behavior of the panels. The presented research does not cover the structural analysis of the TC panels.

2. The aesthetics of a building façade is important in appealing to its stakeholders. It is the outermost layer that is exposed to public view. However, in this study, the focus has been to study rigorously a novel façade subsystem that might be capable of saving lighting energy and reducing carbon emissions. Therefore, the discussion on using TC panels strategically in a building façade to enhance its aesthetical value is considered to be outside the scope of presented research.

3. Two case studies are considered in Chapter 8 that calculate the heat and light transmitted by a TC wall made up of an assembly of several TC panels. Though the TC wall is regarded as one complete unit, the thermal effects of connections between TC panels that might be present is not described.

4. The room considered for case studies were windowless which is not representative for most of the commercial and residential spaces in the United States. The reason to exclude windows from the models was to observe the absolute contribution of TC panels in imparting natural sunlight and exchanging heat with the indoors.

9.2 Passive daylighting systems

A passive daylighting system captures sunlight using a static, non-moving and non-tracking collector and reflects the sunlight into a defined space. One of the passive daylighting systems that can be coupled with optical fibers in the TC panel is called 'Winston Cones (WC)'. These cones have a special parabolic geometry which includes them into the class of non-imaging concentrators called 'Compound Parabolic Concentrators (CPC)'. Figure 9.1 shows the image of a WC.

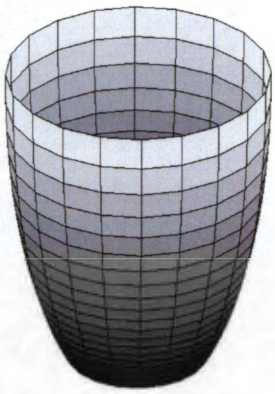

Figure 9.1: A 3D representation of a Winston Cone (WC).

Modeling a WC

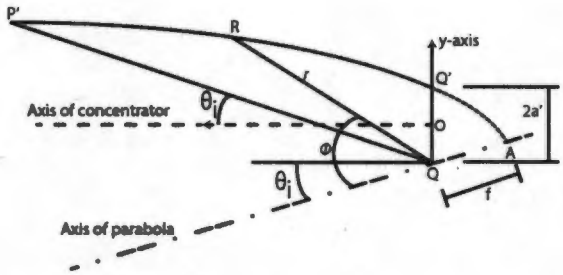

Figure 9.2: A 2D profile of WC. The focal length, f, of the WC is given as QA, the acceptance angle is θ_i, the polar coordinates of WC are (r, ϕ, z) and the diameter of the exit aperture, $Q'Q$ is $2a'$.

The 2-D profile of a WC is constructed from Figure 9.2. The shape of WC is determined from the diameter of its exit aperture, $2a'$, and the acceptance angle, θ_i. By coordinate geometry, the focal length, f, of WC is calculated as follows:

$$f = \frac{a'}{1 + \sin\theta_i} \tag{9.1}$$

The profile of a 2D CPC is expressed in the coordinate system (r, ϕ, z) which is described in Equation (9.2). The derivation of the geometric profile can be found in [65].

$$\begin{aligned}(r\cos\theta_i + z\sin\theta_i)^2 + 2a'(1+\sin\theta_i)^2 r - 2a'\cos\theta_i(2+\sin\theta_i)z - \\ a'^2(1+\sin\theta_i)(3+\sin\theta_i) = 0\end{aligned} \tag{9.2}$$

In polar coordinates, the parametric equations can be written in terms of (r, z) as:

$$r = \frac{2f\,sin(\phi - \theta_i)}{1 - cos\phi} - a', \quad z = \frac{2f\,cos(\phi - \theta_i)}{1 - cos\phi} \tag{9.3}$$

where ϕ traces the surface of the CPC by varying between $[2\theta_i, \theta_i + \pi/2]$

The surface for a 3D CPC is generated by revolving the 2D CPC about its axis of concentration, which can be parametrically obtained by substituting $r^2 = x^2 + y^2$. The resultant fourth order surface and the corresponding spatial variables are given as:

$$((\cos\theta_c\sqrt{x^2+y^2} + z\sin\theta_c)^2 + 2a'(1+\sin\theta_c)\sqrt{x^2+y^2} - 2a'\cos\theta_c(2+\sin\theta_c)z - a'^2(1+\sin\theta_c)(3+\sin\theta_c) = 0 \tag{9.4}$$

$$\begin{aligned} x &= \frac{2f\sin\psi\sin(\phi-\theta_c)}{1-\cos\phi} - a'\sin\psi \\ y &= \frac{2f\cos\psi\sin(\phi-\theta_c)}{1-\cos\phi} - a'\cos\psi \\ z &= \frac{2f\cos(\phi-\theta_c)}{1-\cos\phi} \end{aligned} \tag{9.5}$$

where ψ represents the azimuthal angle between $[0, 2\pi]$ to revolve the 2D profile of a CPC about its axis of concentration. As an example, a 3D winston cone is created in Figure 9.3 with an exiting radius, $a' = 0.01\ m$, and an acceptance angle, $\theta_i = 57°$.

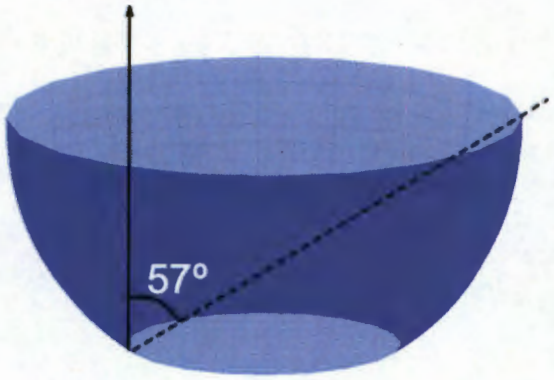

Figure 9.3: A 3D CPC with an acceptance angle, $\theta_i = 57°$ and exit radius, $a' = 0.01\ m$.

Improvement in performance of the TC panel

The performance of a CPC is analysed using the concepts of ray tracing that were discussed in Chapter 2. Figure 9.4 shows the progression of rays inside the CPC.

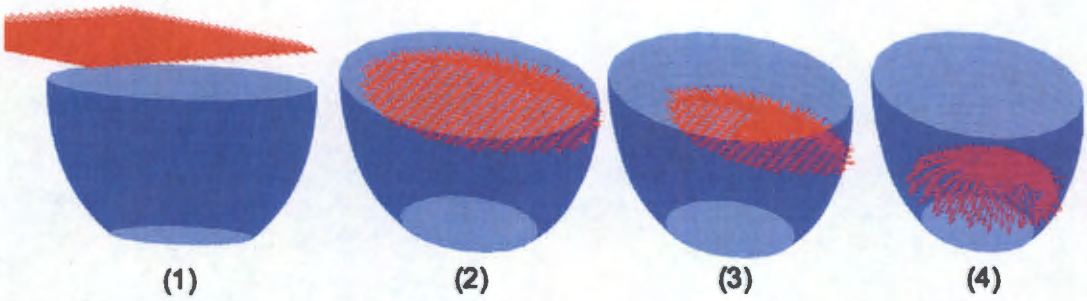

Figure 9.4: Ray tracing through a compound parabolic concentrator.

The CPC has two main characteristics that can be exploited to capture and concentrate more light into an optical fiber. These are:

1. Larger surface area for capture of sunlight during the day.
2. Acceptance of light over a larger range of incident angles.

While the first feature in the list is obvious from the figures above, the second feature is dependent on the acceptance angle of the selected CPC. Therefore, the range of angles for light transmission can be controlled geometrically in a CPC instead of being dictated by the choice of materials, which is the case in an optical fiber. The difference in the performance curves over a range of incident angles for a CPC (given in Figure 9.3) and an optical fiber are shown in Figure 9.5 compared to that in Figure 2.6.

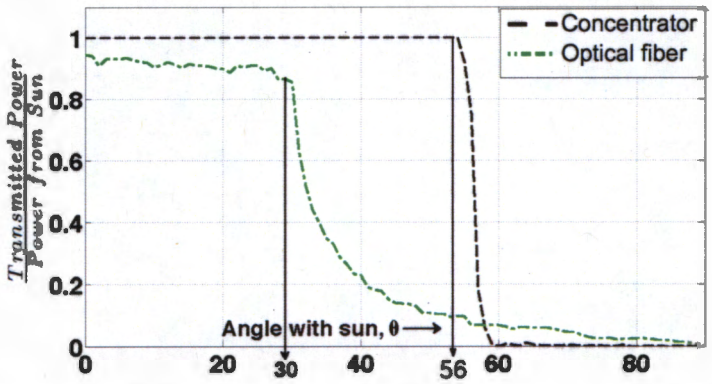

Figure 9.5: Ray tracing light through a parabolic concentrator.

At the same time, the model development for CPC would need further research to solve the following limitations:

1. The design and geometry of the CPC are dependent on the location and weather conditions. Therefore, based on these factors, an optimal design needs to be developed which will be suitable for a specific location.

2. A proper design is required to couple the light exiting from the CPC with the optical fibers to minimize the loss of light.

3. A totally reflective surface of CPC might be difficult to produce. This can affect the performance of light transmission in a (CPC+TC) system.

9.3 Active daylighting systems

Active daylighting is a system for capturing sunlight using actuable devices to increase the efficiency of light collection by tracking the Sun. As a part of future research, it is envisioned that slender and flexible beams made of polymer material will be mechanically or electro-mechanically activated to track the Sun during the day. These devices will be coupled to the optical fibers in the TC panels and will most likely protrude out of the building. A simple 2D simulation of these actuated beams using co-rotational beam formulation of finite elements is shown in Figure 9.6. Interested readers are referred to [9], [67] for a detailed explanation on co-rotational formulation concepts.

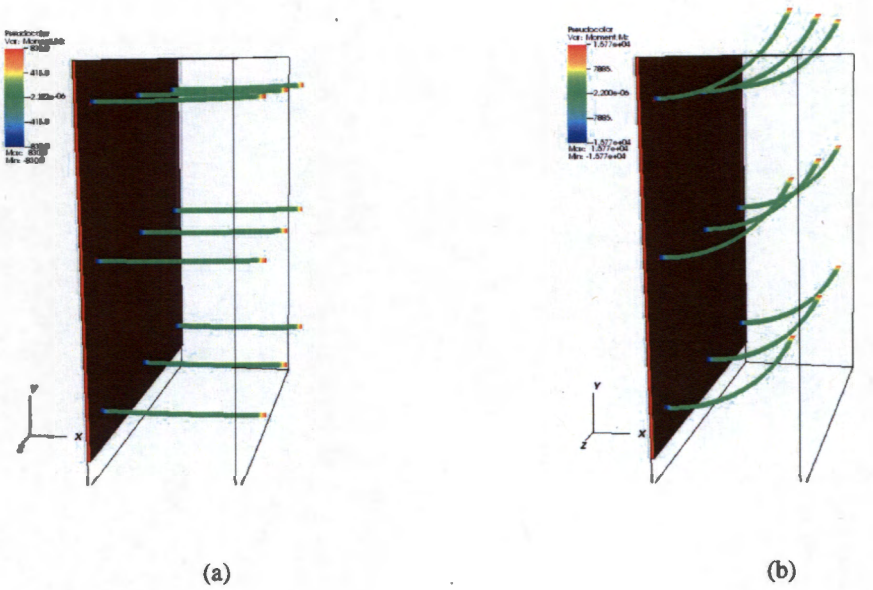

(a) (b)

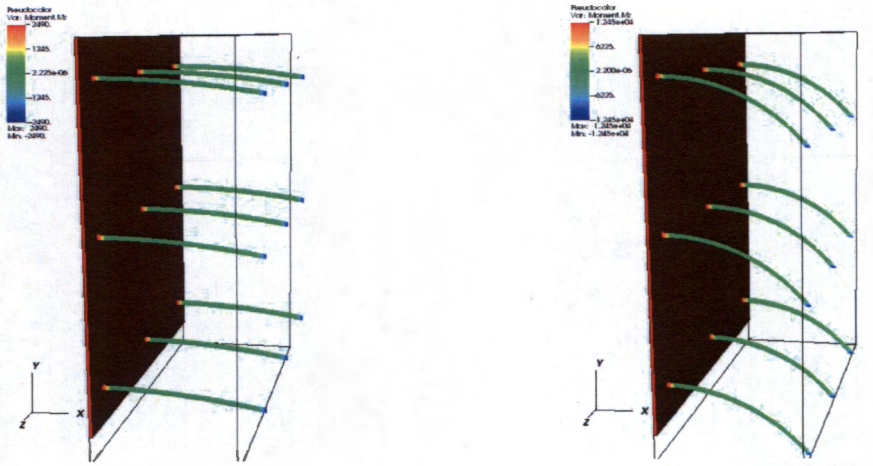

(c) (d)

Figure 9.6: Flexible beams undergoing large deformation will be used to track the sun.

The main challenge in the design of such flexible beams would be related to the choice of materials which will affect their fatigue life. Further, the shape of the beams will have to be modified to reduce their inertial mass while improving the light transmission capability of the TC panel by actuation *e.g* electromagnetically.

9.4 Controlling solar radiation using coatings

The solar radiation transmitted by the optical fibers can cause potential overheating of the room. In Figures 8.16 and 8.19, it was shown that solar radiation was the main cause of cooling loads experienced by the HVAC in rooms with TC panels having high fiber density. In fact, the heat from radiation was so immense that it led to the usage of air conditioners during the winters of Berkeley. Therefore, our next generation of fibers in TC panels should include technologies that can filter the parts of sunlight that are not visible, *i.e.* Ultra-violet (UV) and Infrared (IR). Using an ideal filter consisting of multiple layers of coatings, one would only receive visible light through the TC panel, which will illuminate the room while eliminating the transfer of heat from non-visible spectra (46.6% of incident solar radiation). This leads to the contribution of heat flow as shown in Figure 9.7 (compared to Figure 8.19) into the room due to conduction, solar radiation and heat dissipation from luminaires. As a result of the application of these coatings and using ULCC in walls, the energy expenditure on utilities is also impacted substantially. There is an estimated potential to save as much as 25% of total expenses by eliminating the non-visible spectra from the solar radiation and increasing the thermal resistivity of the walls. This observation is shown in Figure 9.8 .

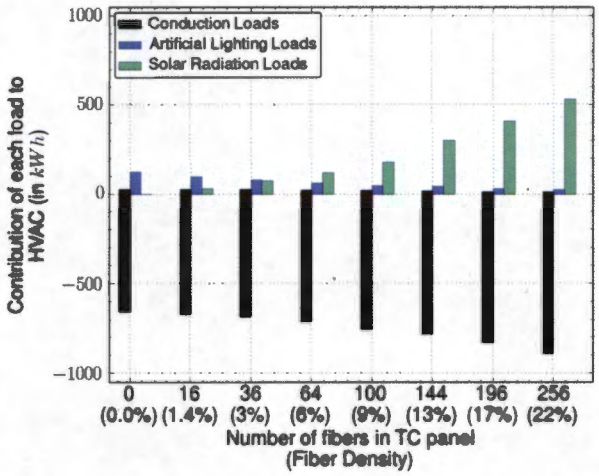

Figure 9.7: The contribution by the heating and cooling loads (expressed in kWh) to the total HVAC load for the case when the entrance apertures of optical fibers are coated with UV and IR filters and the walls comprises of ULCC.

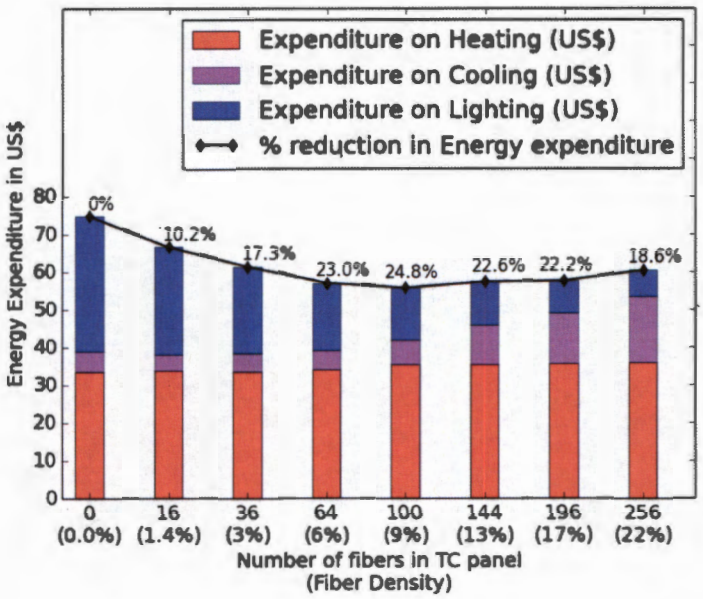

Figure 9.8: Total expenditure on cooling, heating and lighting the room space; Estimated savings in energy after applying UV and IR filters by coating on the entrance apertures of optical fibers and using ULCC in walls.

To implement this technology, it will be important to use thin film coatings that are compatible with optical fibers and can endure the harsh conditions of ambient environment for as long as the life of the TC panels. The use of coated fibers might raise the total cost of manufacturing the TC panels. Hence, a cost-benefit analysis would be needed to justify their use as a suitable alternative.

9.5 Integrated approach for sustainable building façade design

The idea of sustainable development concept was first discussed at the United Nation Conference on environment and development held at Rio de Janeiro in 1992 [30]. The report defined sustainable development as "development that meets the needs of the present generations without compromising the ability of the future generations to meet their needs and aspirations". This meant that in any sustainable design, factors affecting ecology, energy, economy, society and environment should be considered. The same rules apply to

the construction of buildings as well.

Since a building's envelope is the first line of defence between the external influences (like weather changes, pollution, sunlight, water permeability, etc.) and the internal environment, a building cannot be sustainable unless the envelope is sustainable. Therefore, an effort to achieve building envelope sustainability should not be derived from the performance assessment methods meant for buildings alone but also considering the different building envelope design types [23]. To evaluate these designs, Iwaro et al. [27], [26] proposed an Integrated Performance Model (IPM) that combined sustainable development values in a single performance framework for the assessment of the building envelope's sustainable performance and sustainable design.

The IPM framework is based on 6 major sustainable performance criteria: economic efficiency (EC), material efficiency (ME), external benefit (EB), regulation efficiency (RE), energy efficiency (EN), and environmental impact (EI) and several sub-criteria related to each major criteria. The framework quantifies the life cycle performance data for EN through Life Cycle Energy Analysis (LCEA); ME, RE, EI and EB through Life Cycle Impact Assessment (LCIA); and EC performance data through the Life Cycle Cost Analysis (LCCA). The performance values for different alternatives are calculated and transferred to the Integrated Performance Index (IPI). The IPIs for each alternative is combined with an integrated weighting factor (obtained subjectively from experts in the field and objectively from simulations) to generate Sustainable Performance Values (SPVs) for selecting the best alternative. The framework for the IPM is given in Figure 9.9 while the selection of the best alternative follows Table 9.1.

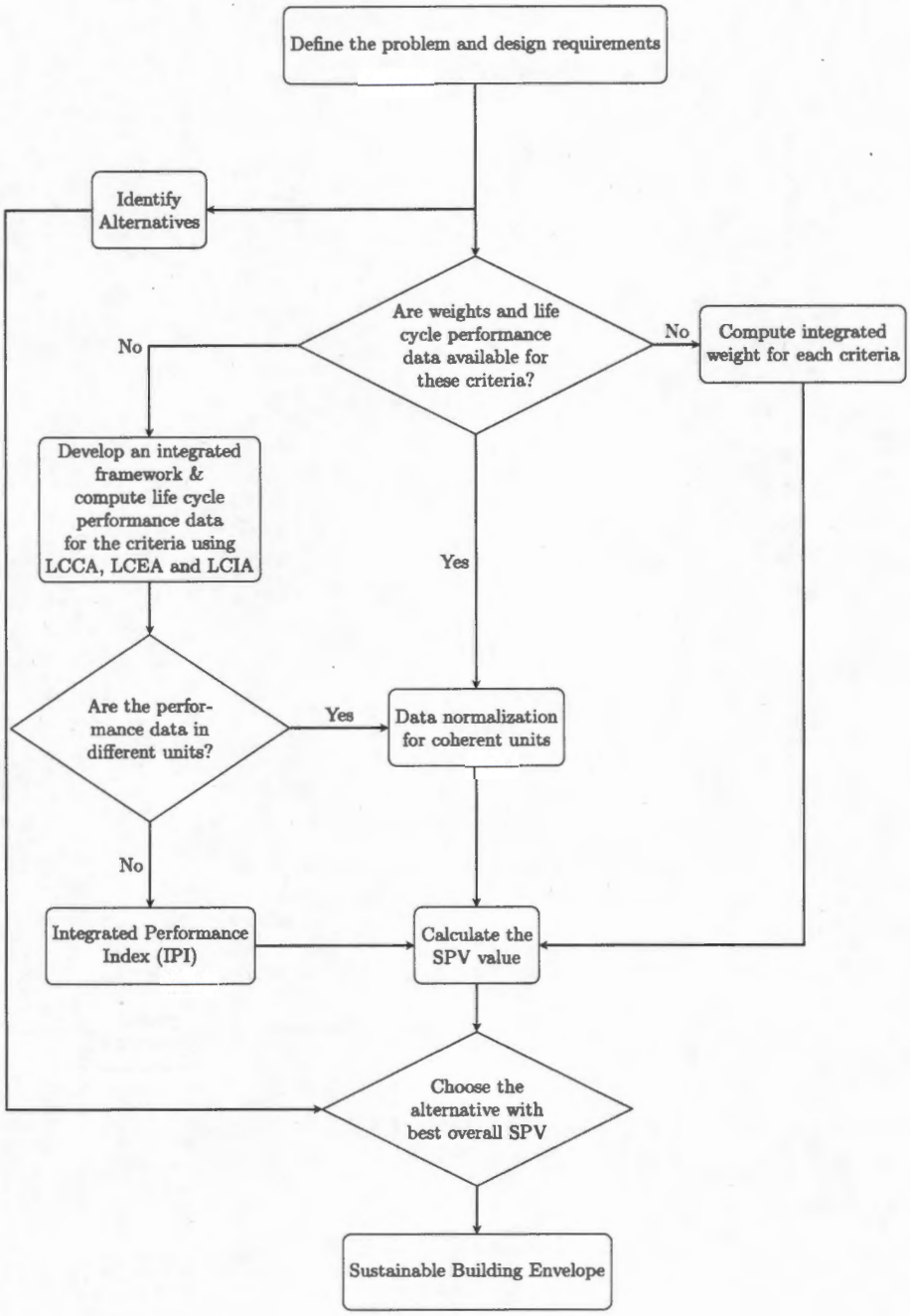

Figure 9.9: Flow chart for the IPM.

Table 9.1: Performance assessment of different alternatives $\{A, B, C\}$. Each SPV is computed by multiplying the performance value, P_i, with its corresponding weight, W_i. The overall SPV (*i.e.* OSP) is the summation of all $SPVs$ for a given design. The alternative with the largest OSP is considered to be the best design.

	Alternative A		Alternative B		Alternative C		
	Performance Value (PV)	SPV	PV	SPV	PV	SPV	W_T
Decision making criteria	P_1	SPV_1	P_1	SPV_1	P_1	SPV_1	W_1
	P_2	SPV_2	P_2	SPV_2	P_2	SPV_2	W_2
	P_3	SPV_3	P_3	SPV_3	P_3	SPV_3	W_3
	P_4	SPV_4	P_4	SPV_4	P_4	SPV_4	W_4
	P_5	SPV_5	P_5	SPV_5	P_5	SPV_5	W_5
	P_6	SPV_6	P_6	SPV_6	P_6	SPV_6	W_6
Overall SPV	$\sum_i SPV_i = OSP_A$		OSP_B		OSP_C		

It is hoped that further iterations to the total design and construction of the TC panels will follow an integrated approach which will lead to a sustainable product. This will be also needed in the future as building assessments are being conducted using tools like Leadership in Energy and Environment Design (LEED), Building Research Establishment Assessment Method (BREEAM) and Green Star, which certify buildings for their sustainability measures and can be helpful in earning points or credit awards for developing a sustainable building envelope.

Bibliography

[1] B. Abushakra et al. *Compilation of Diversity Factors and Schedules for Energy and Cooling Load Calculations*. 2001.

[2] A. Ahuja, K. M. Mosalam, and T. I. Zohdi. "An Illumination Model For Translucent Concrete Using RADIANCE". In: *14th International Conference of the International Building Performance Simulation Association (IBPSA)*. Hyderabad, India, 2015.

[3] A. Ahuja, K. M. Mosalam, and T. I. Zohdi. "Computational Modeling of Translucent Concrete Panels". In: *Journal of Architectural Engineering* 21.B4014008 (2014).

[4] D. Bourgeois, C. Reinhart, and Macdonald I. "Adding advanced behavioural models in whole building energy simulation: A study on the total energy impact of manual and automated lighting control". In: *Energy and Buildings* 36.7 (2006), pp. 814–823.

[5] P. R. Boyce et al. "Occupant use of switching and dimming controls in offices". In: *Lighting Research and Technology* 38.4 (2006), pp. 358–376.

[6] J. W. Bugler. "The determination of hourly insolation on an inclinated plane using a diffuse irradiance model based on hourly measured global horizontal insolation." In: *Solar Energy* 19.477-491 (1977).

[7] D. D. L. Chung. "Cement-matrix composites for thermal engineering". In: *Applied Thermal Engineering* 21.16 (2001), pp. 1607–1619.

[8] D. Crawley, J. Hand, and L. Lawrie. "Improving the weather information available to simulation programs". In: *Proceedings of Building Simulation '99*. Vol. 2. 1999.

[9] M.A. Crisfield. "Nonlinear finite element analysis of solids and structures." In: vol. 1. Chichester, England: John Wiley and Sons Ltd., 1991.

[10] M. Deru. *Energy savings modeling and inspection guidelines for commerical building federal tax deductions*. Tech. rep. National Renewable Energy Laboratory, 2007.

[11] DOE. *Building Energy Data 2010*. Tech. rep. 2011.

[12] C. A. Gueymard. "SMARTS2-A simple model of the atmospheric radiative transfer of sunshine: algorithms and performance assessment." In: *Florida Solar Energy Center Report FSEC-PF-270-95*. 1995.

[13] C. A. Gueymard. "The suns total and spectral irradiance for solar energy applications and solar radiation models." In: *Solar energy* 76.4 (2004), pp. 423–453.

[14] M. P. Gutierrez and T. I. Zohdi. "Effective reflectivity and heat generation in sucrose and PMMA mixtures." In: *Energy and Buildings* 71 (2014), pp. 95–103.

[15] J. E. Hay. "Calculation of monthly mean solar radiation for horizontal and inclined surfaces." In: *Solar Energy* 23.4 (1979), pp. 301–307.

[16] J. He et al. "Study on Smart Transparent Concrete Product and Its Performances." In: *The 6th International Workshop on Advanced Smart Materials and Smart Structures Technology*. Dalian, China, 2011.

[17] J. J. Hirsch. *DOE-2.2 [Computer Program]*. 2003. URL: http://www.doe2.com.

[18] H. C. Hottel. "A simple model for estimating the transmittance of direct solar radiation through clear atmosphere." In: *Solar Energy* 18 (1976), pp. 129–139.

[19] B. Huang and K. Mosalam. *Construction and Testing of the Energy Efficient Translucent Concrete Panels*. Tech. rep. UCB/SEMM-2015/04, University of California, Berkeley, 2015.

[20] D.R.G Hunt. "Predicting artificial lighting use-a method based upon observed patterns of behaviour". In: *Lighting research and technology* 12.1 (1980), pp. 7–14.

[21] D.R.G Hunt. "The Use of Artificial Lighting in Relation to Daylight Levels and Occupancy". In: *Building and Environment* 14.1 (1979), pp. 21–33.

[22] A. A. E. Ibrahim et al. "Estimation of solar irradiance on inclined surfaces facing south in Tanta, Egypt." In: *International Journal of Renewable Energy Research* 1.1 (2011), pp. 18–25.

[23] I. Iqbal and M. S. Al-Homoud. "Parametric analysis of alternative energy conservation measures in an office building in hot and humid climate." In: *Building and environment* 42.5 (2007), pp. 2166–2177.

[24] L. Irene and R. Tiong. "Examining the role of building envelopes towards achieving sustainable buildings." In: *International Conference on Whole Life Urban Sustainability and its assessment*. Ed. by M. Horner, C. Hardcastle, and A. Price. Glasgow, 2007.

[25] T. Ishigure, E. Nihei, and Y. Koike. "Optimum refractive-index profile of the graded-index polymer optical fiber, toward gigabit data links". In: *Applied Optics* 35.12 (1996), pp. 2048–2053.

[26] J. Iwaro and A. Mwasha. "The impact of sustainable building envelope design on building sustainability using Integrated Performance Model." In: *International Journal of Sustainable Built Environment* 2.2 (2013), pp. 153–171.

[27] J. Iwaro et al. "An integrated approach for sustainable design and assessment of residential building envelope: part I". In: *International Journal of Low-Carbon Technologies* (2014).

[28] J. D. Jennings et al. "Comparison of control options in private offices in an advanced lighting controls testbed". In: *Proceedings of the Illuminating Engineering Society*. Paper No. 44, 1999, pp. 275–298.

[29] X. Jiang et al. "Design and implementation of a high-fidelity AC metering network". In: *Information Processing in Sensor Networks, 2009. IPSN 2009. International Conference on*. IEEE, 2009, pp. 253–264.

[30] S. P. Johnson. *The Earth Summit: The United Nations Conference on Environment and Development (UNCED)*. Tech. rep. 1993.

[31] W. Jones. "Linear Optical Properties of organic solids". In: *Organic molecular solids: Properties and applications*. CRC Press, 1997.

[32] T. Kaino. "Absorption losses of low loss plastic optical fibers." In: *Japanese journal of applied physics* 24.12R (1985).

[33] F. Kasten and A. T. Young. "Revised optical air mass tables and approximation formula". In: *Applied Optics* 28.22 (1989), pp. 4735–4738.

[34] D. Kato and T. Nakamura. "Application of optical fibers to the transmission of solar radiation." In: *Journal of Applied Physics* 47.10 (1976), pp. 4528–4531.

[35] B. Leckner. "The spectral distribution of solar radiation at the earths surface-elements of a model." In: *Solar Energy* 20 (1978), pp. 143–150.

[36] D. Lindelöf and N. Morel. "A field investigation of the intermediate light switching by users." In: *Energy and Buildings* 38.7 (2006), pp. 790–801.

[37] B. Y. Liu and R. C. Jordan. "The interrelationship and characteristic distribution of direct, diffuse and total solar radiation." In: *Solar energy* 4.3 (1960), pp. 1–19.

[38] X. Liu et al. "Far-field distance for surface light source with different luminous area". In: *Applied Optics* 52.8 (2013), pp. 1629–1635. DOI: 10.1364/AO.52.001629. URL: http://ao.osa.org/abstract.cfm?URI=ao-52-8-1629.

[39] A. Losonczi. *Building block comprising light transmitting fibres and a method for producing the same.* 2005.

[40] J. A. Love. "Manual switching patterns in private offices." In: *Lighting Research and Technology* 30.1 (1998), pp. 45–50.

[41] W. Lu et al. "Experimental Evaluation of a Glass Curtain Wall of a Tall Building." In: *Earthquake Engineering and Structural Dynamics (Under Review)* (2016).

[42] S. L. Manzello et al. "Measurement of thermal properties of gypsum board at elevated temperatures." In: *Proceedings of the 5th International Conference on Structures in Fire.* Nanyang Technological University, Singapore, May 2008, pp. 656–665.

[43] W. H. McAdams. *Heat Transmission.* Third. Tokyo, Japan: McGraw-Hill Kogakusha, 1954.

[44] K.M. Mosalam et al. "Anidolic Day-Light Concentrator in Structural Building Envelope". In: *First Annual International Conference on Architecture and Civil Engineering (ACE 2013).* Singapore, 2013.

[45] T. Muneer. "Solar radiation model for Europe." In: *Building Services Engineering Research and Technology* 11.4 (1990), pp. 153–163.

[46] K. Narisada and D. Schreuder. *Light pollution handbook.* Vol. 322. Springer Science & Business Media, 2013.

[47] G. R. Newsham, A. Mahdavi, and I. Beausoleil-Morrison. "Lightswitch: a stochastic model for predicting office lighting energy consumption". In: *3rd European Conference on Energy-Efficient Lighting.* 1995, pp. 59–66.

[48] A. M. Noorian, I. Moradi, and G. A. Kamali. "Evaluation of 12 models to estimate hourly diffuse irradiation on inclined surfaces." In: *Renewable energy* 33.6 (2008), pp. 1406–1412.

[49] F. J. Olmo et al. "Prediction of global irradiance on inclined surfaces from horizontal global irradiance." In: *Energy* 24.8 (1999), pp. 689–704.

[50] C. D. Ouden and T. C. (Eds.) Steemers. *Building 2000: Volume 2 Office Buildings, Public Buildings, Hotels and Holiday Complexes.* Springer Science & Business Media, 2012.

[51] J. Page et al. "A generalised stochastic model for the simulation of occupant presence". In: *Energy and buildings* 40.2 (2008), pp. 83–98.

[52] M. Paulescu et al. "Modeling solar radiation at the Earth surface". In: *Weather modeling and forecasting of PV systems operation.* Springer Science & Business Media., 2012, pp. 127–179.

[53] R. Perez et al. "A new simplified version of the Perez diffuse irradiance model for tilted surfaces." In: *Solar energy* 39.3 (1987), pp. 221–231.

[54] S. Pigg, M. Eilers, and J. Reed. "Behavioural aspects of lighting and occupancy sensors in privates offices: a case study of a university office building." In: *Proceedings of ACEEE Summer Study on Energy Efficiency in Buildings 8*. 1996, pp. 161–171.

[55] M. Praprotnik, M. Sterk, and R. Trobec. "Inhomogeneous heat-conduction problems solved by a new explicit finite difference scheme." In: *International Journal of Pure and Applied Mathematics* 13.3 (2004), pp. 275–291.

[56] Y. Qin, D. Lin, and S. Y. Hui. "A simple method for comparative study on the thermal performance of LEDs and fluorescent lamps." In: *Power Electronics, IEEE Transactions*. Vol. 24. 7. 2009, pp. 1811–1818.

[57] D. T. Reindl, W. A. Beckman, and J. A. Duffie. "Evaluation of hourly tilted surface radiation models." In: *Solar Energy* 45.1 (1990), pp. 9–17.

[58] C.F. Reinhart and K. Voss. "Monitoring manual control of electric lighting and blinds." In: *Lighting Research and Technology* 35.3 (2003), pp. 243–260.

[59] Christoph F. Reinhart. "Lightswitch-2002: a model for manual and automated control of electric lighting and blinds". In: *Solar Energy* 77.1 (2004), pp. 15–28.

[60] F. M. Rubinstein et al. "Analyzing Occupancy Profiles from a Lighting Controls Field Study". In: *CIE Conference*. San Diego, 2003.

[61] J. Samimi. "Estimation of height-dependent solar irradiation and application to the solar climate in Iran." In: *Solar Energy* 52.5 (1994), pp. 401–409.

[62] O. Sepp anen, W. J. Fisk, and Q. H. Lei. *Effect of Temperature on Task Performance in Offfice Environment*. Tech. rep. Lawrence Berkeley National Laboratory, Berkeley, CA, 2006.

[63] Krzysztof Wandachowicz. "Calculation of Luminaires Using Radiance." In: *3rd International RADIANCE Workshop*. Fribourg, Switzerland, 2004.

[64] D. Wang, C. C. Federspiel, and F. Rubinstein. "Modeling occupancy in single person offices". In: *Energy and buildings* 37.2 (2005), pp. 121–126.

[65] R. Winston, J. C. Miñano, and P. Benítez. "Nonimaging Optical Systems". In: *Nonimaging Optics*. Elsevier Academic Press, 2005, pp. 43–68.

[66] Y. Wu et al. "Development of ultra-lightweight cement composites with low thermal conductivity and high specific strength for energy efficient buildings." In: *Construction and Building Materials* 87 (2015), pp. 100–112.

[67] L. L. Yaw. *2D Corotational Beam Formulation*. 2009.

[68] T. I. Zohdi. "Modeling and simulation of the optical response rod-functionalized reflective surfaces." In: *Computational Mechanics* 50.2 (2012), pp. 257–268.

[69] J. Zubia and J. Arrue. "Plastic optical fibers: An introduction to their technological processes and applications." In: *Optical Fiber Technology* 7.2 (2001), pp. 101–140.

Appendix A

Geometrical Ray Theory

The propagation of any disturbance, Ψ, is governed by the wave equation

$$\nabla^2\Psi = \frac{1}{c^2(\mathbf{x})}\frac{\partial^2\Psi}{\partial t^2} \tag{A.1}$$

Here, $c(\mathbf{x})$ is a spatially varying wave speed corresponding to the medium defined by $\mathbf{x}$ for the wave and t represents time. A trial wave solution of the following form is used

$$\Psi(\mathbf{x},t) = A(\mathbf{x})\exp\{j(\mathbf{k}_o S(\mathbf{x}) - \omega t)\} \tag{A.2}$$

where $A(\mathbf{x})$ is the amplitude of the disturbance, $j = \sqrt{-1}$, ω is the angular velocity and $k_o = 2\pi/\lambda$ is the wave number in the reference medium. The function $S(\mathbf{x})$ is known as the "Eikonal". One can interpret the waves from a far away source, like the sun, as a family of surfaces for which the values of $k_o S(\mathbf{x})$ differ in incremental subdivisions of 2π. By substituting Equation (A.2) into the wave formulation in Equation (A.1), one obtains:

$$k_o^2 A(n^2 - \nabla S.\nabla S) + jk_0(2\nabla A.\nabla S + A\nabla^2 S) + \nabla^2 A = 0 \tag{A.3}$$

where n is the refractive index of the medium and is defined as the ratio of speed of wave in the medium to that in vacuum. The 'Ray Theory' suggests that as $k_0 \to \infty$ with smaller wavelengths, the wave equation in (A.3) is only satisfied if $\nabla^2 A$ and the coefficients of k_0 are equal to zero. These requirements yield:

$$n^2 = \nabla S.\nabla S = \|\nabla S\|^2 \tag{A.4}$$

This implies that Equation (A.4) gives

$$\nabla S(\mathbf{x}) = n(\mathbf{x})\hat{\mathbf{s}}(\mathbf{x}) \tag{A.5}$$

where $\hat{\mathbf{s}}(\mathbf{x})$ is a unit direction vector.

As mentioned before, $S(\mathbf{x})$ gives the definition of the surface for the waves. The gradient of $S(\mathbf{x})$ represents the rays that are perpendicular to this surface. The second term of Equation (A.3) is equated to zero to give

$$\frac{1}{A}\nabla A.\nabla S = -\frac{1}{2}\nabla^2 S = -\frac{1}{2}\nabla.(n\hat{\mathbf{s}}) \tag{A.6}$$

The directional derivative, $\frac{d(\circ)}{ds} = \hat{\mathbf{s}}.\nabla(\circ)$, is applied to the amplitude of the wave, A

$$\frac{dA}{ds} = \hat{\mathbf{s}}.\nabla A = \left(\frac{\nabla S}{n}\right).\nabla A \tag{A.7}$$

Substituting right hand side of Equation (A.7) in Equation (A.6) and rearranging terms gives

$$\frac{1}{A}\frac{dA}{ds} = -\frac{1}{2n}\nabla.(n\hat{\mathbf{s}}) \tag{A.8}$$

The derivation of Equation (A.8) alludes to show how the amplitude of the trial solution, A, only changes with a ray following a direction, $\hat{\mathbf{s}}$ or ∇S, rather than any other perpendicular direction. This is the fundamental principle of "Ray Tracing" that it deals directly with the ray trajectories and not the wavefront surface, S.

The trajectory of a ray with direction, $\hat{\mathbf{s}}$, can be expressed from Equation (A.5) as

$$\begin{aligned}
\frac{d(n\hat{\mathbf{s}})}{ds} &= \hat{\mathbf{s}}.\nabla(\nabla S) && \text{(taking directional derivative)} \\
&= \frac{\nabla S}{n}.\nabla(\nabla S) && \text{applying Equation (A.5)} \\
&= \frac{1}{2n}\nabla(\nabla S.\nabla S) \\
&= \frac{1}{2n}\nabla n^2 && \text{applying Equation (A.4)} \\
\frac{d(n\hat{\mathbf{s}})}{ds} &= \nabla n
\end{aligned} \tag{A.9}$$

Thus, to march rays in space, all one needs to know is the initial direction ($\hat{\mathbf{s}}_i$) and the index of refraction, $n(x, y, z)$ of the space in which the ray will be travelling.

Appendix B

Refractive index profiles of optical fibers

The refractive index profiles of two types of fibers are defined. The first type is called the 'Step Index (SI)' fiber which assigns one refractive index for the core and one for the cladding. Since there is a jump at the core-cladding interface of the optical fiber, the discontinuity is resolved by smearing the interface to produce a refractive index profile which is continuous. The resulting profile is given as:

$$n(r) = n_{cladding}\left\{1 + \frac{n_{core} - n_{cladding}}{n_{cladding}} \exp\left[-\left(\frac{r^2}{R_{core}^2}\right)^k\right]\right\} \tag{B.1}$$

where n_{core} is the core refractive index, $n_{cladding}$ is the cladding refractive index, R_{core} is the core radius and r is the distance to the point at which the refractive index is specified. As $k \to \infty$, $n(r)$ becomes closer to the profile defined for an ideal SI fiber. Thus we use a value that is large to approximately replicate the profile of an ideal SI fiber.

The second class of optical fibers is called the 'Gradient Index (GI)' fiber which has a refractive index profile that changes parabolically between the core and the cladding. The function for this profile is defined as

$$n(r) = \begin{cases} n_{core}\left(1 - \left(\frac{n_{core}^2 - n_{cladding}^2}{n_{core}^2}\right)\frac{r^2}{R_{core}^2}\right)^{0.5}, & \text{for } r \leq R_{core} \\ n_{cladding} & \text{for } r > R_{core} \end{cases} \tag{B.2}$$

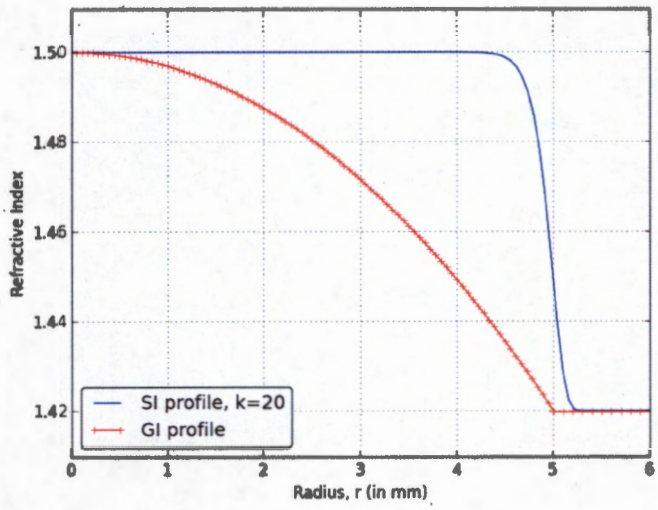

Figure B.1: Refractive index profiles for SI and GI fibers. Core radius is 5 mm and fiber radius is 6 mm.

Appendix C

Luminare description of optical fiber

The optical fiber is treated as a point source that emits light and illuminates part of a defined space located at a distance which is at least fives times the diameter of the optical fiber. To fully define an optical fiber, we need to first describe the geometry and material of the exit end of the fiber that emits light.

Code for defining the geometry and material of optical fiber in RADIANCE

```
# ies2rad -t white
# Dimensions in meters
# 1 watt luminaire, lamp*ballast factor = 1

void brightdata lum_dist
4 flatcorr lum_dist.dat source.cal src_theta
0
1 12732.4

lum_dist light lum_dist_light
0
0
3 1 1 1

lum_dist_light ring lum_dist.d
0
0
8
        0 0 -0.00025
        0 0 -1
        0 0.005
```

Next, the light distribution characteristics of an OF as discussed in Section 4.2 are loaded into *RADIANCE*.

Luminaire description file for optical fibers in RADIANCE

```
1
0 90 91

                  0      1.98870e-07      8.49588e-07      1.76200e-06
        2.63754e-06      3.94999e-06      5.27874e-06      6.69101e-06
        8.28981e-06      9.72311e-06      1.09729e-05      1.22550e-05
        1.40534e-05      1.52634e-05      1.64149e-05      1.76955e-05
        2.07013e-05      2.40025e-05      3.06509e-05      3.97965e-05
        4.18962e-05      4.8632e-05       5.68505e-05      5.95e-05
        6.5624e-05       6.87336e-05      7.2658e-05       7.58347e-05
        8.01228e-05      8.43727e-05      9.12895e-05      9.44352e-05
        9.785e-05        0.000102684      0.0001076        0.000147652
        0.000152832      0.000161155      0.000174749      0.000179441
        0.000188441      0.000192502      0.000239833      0.000255219
        0.000262655      0.000273405      0.00030049       0.000357973
        0.000370096      0.000394814      0.000479901      0.000496516
        0.000574476      0.000628758      0.000736033      0.000780894
        0.000904109      0.001013         0.00120662       0.00148598
        0.00202907       0.00207118       0.00209821       0.00216213
        0.00219616       0.00223259       0.00225208       0.00227162
        0.00229098       0.00231549       0.00233138       0.00234804
        0.00236721       0.00238176       0.0023946        0.00240672
        0.00241987       0.00243028       0.002443         0.00245499
        0.00246856       0.00248703       0.00249584       0.00251135
        0.00252407       0.00253812       0.00254368       0.00255131
        0.00255791       0.00258031       0.00258977
```

After building the geometry and choosing the material properties for the luminaire, calculations are performed to obtain the illuminance distribution in space (x, y, z). The illuminance E_p at point P with coordinates (x_p, y_p, z_p) is calculated using *rtrace* process as:

```
rtrace -h -I+ -ab 1 luminaire.oct <calc_points.txt> Radiance_results
    .txt
```

The *rtrace* command renders the scene without a view and offers operators to extract different types of data from the scene. The $-h$ option excludes headers from the results text file. $-I+$ informs the *rtrace* engine to calculate the point irradiance/illuminance rather than radiance/luminance. The number of ambient bounces for the rays with the room sur-

faces are set by using the $-ab$ option which should be chosen wisely as more reflections need very high memory requirements. The geometry and material properties of the luminaire is described in $luminaire.oct$. The $rtrace$ calculates irradiance for points mentioned in $< calc\_points.txt >$ and saves the resultant values in $Radiance\_results.txt$.

Appendix D

Markov chain Monte Carlo method

A Markov model gives the evolution of a random phenomenon whose future behavior is independent of the past given their current state. More commonly, a random variable $X(t)$ is Markovian if it fulfils the following property

$$p_{(j_{n-1})j_n} = \mathbb{P}(X(t_n) = j_n | X(t_{n-1}) = j_{n-1}, ..., X(t_1) = j_1) \tag{D.1}$$

where $p_{(j_{n-1})j_n}$ describes the probability that the random variable $X(t)$ changes from state j_{n-1} to j_n in a discrete time step from t_{n-1} to t_n. The Markov chain model assumes a memoryless switching between states so Equation (D.2) can be rewritten to give Equation (D.1):

$$p_{(j_{n-1})j_n} = \mathbb{P}(X(t_n) = j_n | X(t_{n-1}) = j_{n-1}) \tag{D.2}$$

for all finite sequence of time $t_1 < ... < t_n \in I$ and of states $j_1, ..., j_n \in S$. This means given sufficient information about the current state, the past does not have any role in determining the probability of reaching final state, j.

In a Markov chain, the following three specifications of a model should be noted:

1. The different states that the random variable, $X(t)$, can attain.
2. The different paths for the transitions between states.
3. The probability of each transition path.

Example of a Markov chain model

The Markov chain is best explained by implementing it for an example. A simple two state model, as shown in Figure D.1, is solved using the Markov chain method.

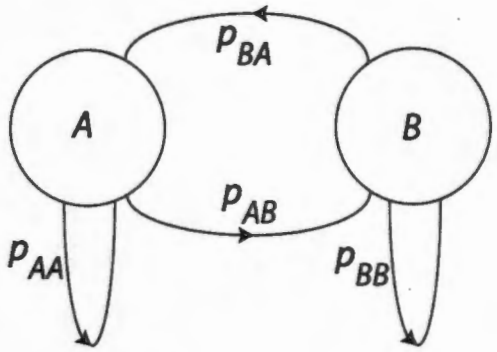

Figure D.1: A Markov chain model with two states, A and B.

The states are recognized as 'A' and 'B'. There are four transition paths in Figure D.1 and their single time step transition probabilities are given as, $p_{AA} = 0.5$, $p_{AB} = 0.5$, $p_{BB} = 0.8$ and $p_{BA} = 0.2$. The transition probabilities, r_{ij} where $i, j \in \{A, B\}$, after different time intervals is given in Table D.1.

Table D.1: Transition probabilities, r_{ij}, at different time instants.

r_{ij}	$n=0$	$n=1$	$n=2$	$n=3$	$n=50$	$n=99$	$n=100$
r_{AA}	1	0.5	$r_{AA}(n=1) \times 0.5 + r_{AB}(1) \times 0.2$ $= 0.35$	0.305	0.286	0.286	0.286
r_{AB}	0	0.5	$r_{AA}(n=1) \times 0.5 + r_{AB}(1) \times 0.8$ $= 0.65$	0.695	0.714	0.714	0.714
r_{BA}	0	0.2	$r_{BA}(n=1) \times 0.5 + r_{BB}(1) \times 0.2$ $= 0.26$	0.278	0.286	0.286	0.286
r_{BB}	1	0.8	$r_{BA}(n=1) \times 0.5 + r_{BB}(1) \times 0.8$ $= 0.74$	0.722	0.714	0.714	0.714

The transition probability at the zeroth time instant ($n = 0$) is simply defined as

$$r_{ij}(n=0) = \begin{cases} 1 & \text{for } i = j \\ 0 & \text{for } i \neq j \end{cases} \tag{D.3}$$

The transition probabilities at first instant are stated as p_{ij} where $i, j \in \{A, B\}$. The transition probabilities for the second time instant ($n = 2$) is directly calculated from the

transition probabilities after the completion of first time step. It can be deduced that to calculate the transition probabilities for $(n = 3)$, we only need the transition probabilities, $r_{ij}(n = 2)$ and p_{ij} to progress from 2^{nd} time instant to the 3^{rd} time instant.

The probabilities, p_{ij} can also be written in terms of its transition matrix, $\mathbb{T}$, which in this case is

$$\mathbb{T} = \begin{bmatrix} 0.5 & 0.5 \\ 0.2 & 0.8 \end{bmatrix} \tag{D.4}$$

In a homogeneous Markov chain, the matrix $\mathbb{T}$ does not change with time. If that is the case, the system is able to reach a steady state after a number of time steps. Thus, in the current example, it can be easily calculated that $\mathbb{T}^{50} = ... = \mathbb{T}^{99} = \mathbb{T}^{100}$. On the contrary, if the transition matrix changes with time, as is observed in the case of an occupancy model, the system may or may not be able to reach an equilibrium state. Such systems are referred to as time-inhomogeneous Markov chain models.

Appendix E

Robust Locally Weighted Smoothing Scatterplots (LOWESS)

The LOWESS scheme is used to draw a nonlinear curve that represents the relation between (x, y) points of the scatterplot. The following procedure is followed:

1. For each x_i (observation point), compute the estimates $\hat{\beta}_j(x_i)$, j = 0, 1, ..., d of the parameters in a polynomial of regression of degree, d (if d is selected to be 1 means the group of points are linearly behaving). Choosing values of $d > 1$, also increases the computation time. The regression of y_k on x_k is fit by weighted least squares with weight $w_k(x_i)$. Thus, $\hat{\beta}_j(x_i)$ are the values of β_j that minimize

$$\sum_{k=1}^{n} w_k(x_i)(y_k - \beta_o - \beta_1 x_k - ... - \beta_d x_k^d)^2 \qquad \text{(E.1)}$$

   The coefficients β_0, β_1,..., β_d, etc. from the above equation are used to find the smoothed x_i and $\hat{y}_i$. Thus, we get

$$\hat{y}_i = \sum_{j=0}^{d} \hat{\beta}_j(x_i) x_i^j \qquad \text{(E.2)}$$

2. Values of $w_k(x_i)$ are found from the weight function, W, that has the following properties:

   - $W(x) > 0$ for $|x| < 1$
   - $W(x) = 0$ for $|x| \geq 1$

- The weight function is a tricubic function given as

$$W(x) = (1 - |x|^3)^2 \; for \; |x| < 1; \text{ and } 0 \; otherwise \tag{E.3}$$

3. Calculate robustness weights, δ_k, for iterations greater than 0.

   - First calculate the error in the solution, e_i

$$e_i = y_i - \hat{y}_i \tag{E.4}$$

   - Then apply a bisquare weight function to calculate δ_k

$$\delta_k = B(e_k/6s) \text{ where } s \text{ is the median of } |e_i| \tag{E.5}$$

   - An example for a bisquare weight function, $B(x)$, is

$$B(x) = (1 - x^2)^2 \; for \; |x| < 1; \text{ and } 0 \; otherwise \tag{E.6}$$

4. With new weights $\delta_k w_k(x_i)$, compute new $\hat{y}_i$ for each i by fitting a d^{th} degree polynomial.

5. Repeat the process for more number of iterations until all high frequency variations are removed.

Appendix F

Detailed construction procedure for TC panels

] The mass production of TC panels was undertaken by the undergraduates and graduate students of Berkeley during summer 2015. Sixty TC panels were produced with white ultra-lightweight cement composites (ULCC) in the concrete laboratory of UC Berkeley to conduct full-scale experiments at the SinBerBEST (Singapore-Berkeley Building Efficiency and Sustainability in the Tropics) testbed focusing on light and thermal measurements. The construction of the TCPs was based on using a large single form and placing the optical fibers (OFs) for various panels at one time. After hardening of the concrete, the block was cut into individual panels using a concrete saw.

Construction Procedure

The construction procedure lists all the steps needed to produce TC panels to the specified dimensions. They are as follows:

1. Construction and assembly of formwork: The acrylic sheets were assembled together using screws and were attached to unistruts from the bottom for ease of handling.

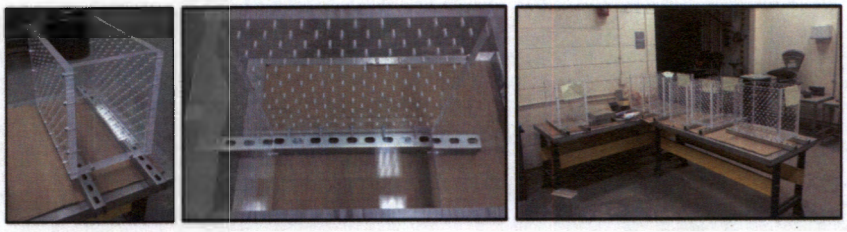

(a) (b) (c)

Figure F.1: The acrylic formwork used for the construction of TC panels.

2. Lubrication of formwork: Forms were greased before concrete was cast. This was done to ensure easy removal of acrylic panels after concrete is hardened.

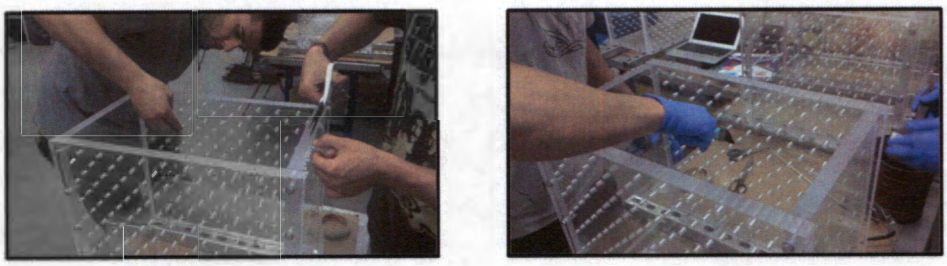

(a) (b)

Figure F.2: Forms were greased with WD-40.

3. Roughening of optical fibers: A very labor intensive process that required roughening of optical fibers' outer surfaces with sand paper to ensure bonding with the concrete materials.

(a) (b)

Figure F.3: The outer surfaces of optical fibers being roughened with sand paper.

4. Insertion of optical fibers in the formwork: The OFs were inserted manually into the formwork one by one. Mini-clamps and cable ties were placed at the two ends of optical fibers to lock them in position in the formwork. The optical fibers were pretensioned to ensure minimum slackening in the middle of fibers upon concrete placement. After inserting the fibers, the surfaces of the fibers were wiped with a clean cloth to ensure proper removal of the traces of greasing agent for further bond enhancement with the concrete.

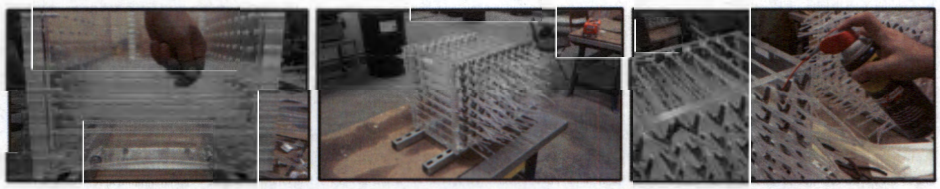

(a) (b) (c)

Figure F.4: Inserting and clamping the optical fibers in place.

5. Concrete mixing and casting: A ULCC mixture for casting was proposed with the following composition:

Table F.1: ULCC mixture

Water	304 kg/m^3
WPC	774.6 kg/m^3
WSF	67.4 kg/m^3
Cenospheres	350.0 kg/m^3
SP [4]	7.2 ℓ/m^3
VMA [4]	6.3 ℓ/m^3
PE fiber [4]	5.3 kg/m^3

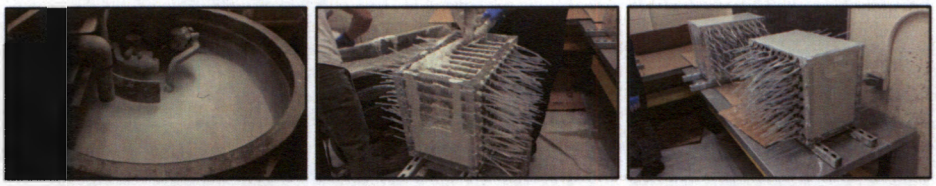

(a) (b) (c)

Figure F.5: Mixing the contents of ULCC and casting concrete in formwork.

6. Form removal and concrete cutting: After a few days of curing in the fog room (100% humidity), the acrylic panels of the formwork are disassembled and the hanging fiber ends are cut such that the face of optical fiber is flush with the face of concrete block. The block is cut into individual panels by a large size concrete saw. The resulting dimensions of each individual panel was 44 cm × 38 cm × 5 cm.

[4]SP or superplastcizers are materials that avoid particle segregation and improves the flow characteristics of concrete; VMA or viscosity modifying admixtures are used in conjunction with SP in optimizing the yield point of the concrete; Polyethylene (PE) fibers are used for the mitigation of plastic shrinkage cracking in concrete

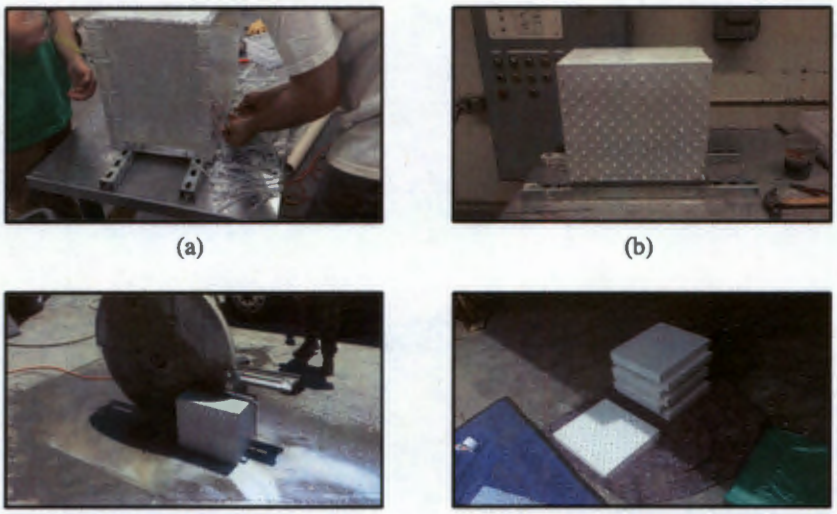

(a) (b)

(c) (d)

Figure F.6: The acrylic panels of the formwork are removed and the concrete block is cut into separate panels.

7. Installation in the Testbed and operation: The TC panels constructed in Berkeley were shipped to Singapore where these panels were installed in the testbed for conducting experiments related to lighting transmission and illuminance distribution in a room space.

(a) (b)

Figure F.7: The TC panels were installed in the Testbed and operated in the presence of a light wall.